Cover Page

The handle http://hdl.handle.net/1887/43417 holds various files of this Leiden University dissertation.

Author: Di Gesu, L.
Title: Winds in the AGN environment : new perspectives from high resolution X-ray spectroscopy
Issue Date: 2016-10-04

Winds in the AGN environment:

new perspectives from high-resolution X-ray spectroscopy

Laura Di Gesu

October 4, 2016

Winds in the AGN environment:
new perspectives from high-resolution X-ray spectroscopy

(met een samenvatting in het Nederlands)

Proefschrift

ter verkrijging van
de graad van Doctor aan de Universiteit Leiden
op gezag van de Rector Magnificus, prof. mr. C. J. J. M. Stolker,
volgens besluit van het College voor Promoties
te verdedigen op 4 Oktober 2016
klokke 13.45 uur

door

Laura Di Gesu

geboren te Vimercate (Italië) in 1984

Promotiecommissie

Promotor:
Prof. dr. J. S. Kaastra

Co-promotor:
Dr. E. Costantini

Overige leden:
Dr. M. Cappi (INAF-IASF, Bologna)
Prof. dr. W. J. Jaffe
Prof. dr. R. Morganti (Rijksuniversiteit Groningen)
Prof. dr. H. J. A. Röttgering
Prof. dr. P. van der Werf

Contents

Introduction

I.1   Active Galactic Nuclei

Active Galactic Nuclei (hereafter AGN) appear as bright point sources located in the center of galaxies. In galaxies hosting an AGN (at least 17% of galaxies in optical spectroscopic surveys, Ho et al. 1997, Carter et al. 2001, Miller et al. 2003) the luminosity of the point-like nucleus ($10^{44} - 10^{46}$ erg s^{-1}) always dominates over the starlight luminosity of the entire galaxy by at least an order of magnitude.

The emission of radiation from AGN covers the entire electromagnetic spectrum, from radio to gamma-ray energies. It is understood that the primary source of energy empowering this enormous release of radiation is the gravitational infall of matter onto a supermassive black hole (hereafter SMBH), with a mass ranging from 10^6 up to a few 10^9 M$_\odot$. This is in fact the most efficient way in nature of extracting energy from matter. For instance, in the case of gravitational accretion onto a fast rotating black hole, the rate of conversion of matter into energy can be up to ∼30% (e.g., Bambi 2012). For comparison, the efficiency of nuclear fusion of hydrogen is only ∼0.7%.

The AGN taxonomy is wide. For historical reasons, local AGN (at redshift z$\lesssim$0.1) are referred to as "Seyfert" galaxies, while more luminous (with a bolometric luminosity $L_{\rm bol} \gtrsim 10^{45}$erg s^{-1}) and distant AGN are more often named as quasars. In the optical AGN are divided into two main classes. The so-called type 1 AGN show broad (BL, with a full width at half maximum *FWHM*$\geq$ 1000 km s^{-1}) and narrow (NL, *FWHM*$\leq$500 km s^{-1}) emission lines in their spectrum, while in type 2 AGN, only NL are present (e.g., Netzer 1990). About ∼15–20% of quasars are ∼100 times brighter at radio than at optical wavelengths (Kellermann et al. 1989). Differently from most radio-quiet AGN, these radio-loud AGN show ∼kpc extended lobe of radio emission (e.g., Centaurus A, Israel 1998).

In the '90s a simple explanation that unified AGN phenomenology was put forward. This so-called "Unified Model" (Fig. I.1 Antonucci 1993, Urry & Padovani 1995) in its basic prescription is still valid today. We give here a brief overview of the basic features of the Unified Model, while in Sect. I.1.1–Sect I.1.5 we summarize in detail the different regions of the AGN.

It is believed that the matter falling onto the SMBH forms a thin accretion disk around it, which emits thermal radiation mostly at optical/UV wavelengths. In the innermost AGN region, close to the SMBH, resides a corona of hot electrons, which Compton upscatters the disk radiation to X-ray wavelengths. The UV-to-X-ray radiation produced in the nuclear region photoionizes the ambient gas. The circumnuclear ionized gas is thought to be distributed in two main regions. The fast moving gas in the so-called Broad Line Region (BLR), which is located in the vicinity of the nucleus is thought to produce the BL. On the other hand, the gas producing the NL is distributed in a roughly conical
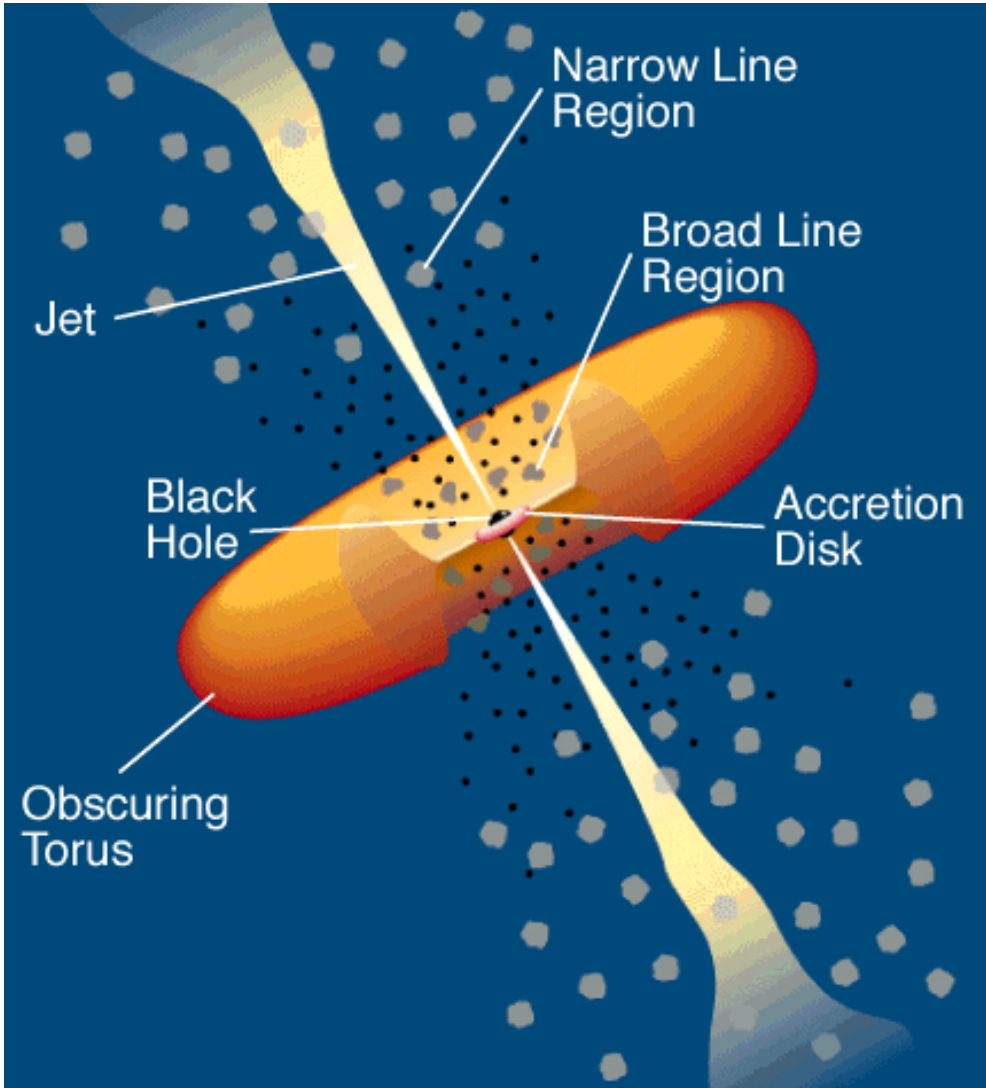
Figure I.1: Sketch of the standard Unified Model for AGN, not to scale. The different AGN regions are labeled. The presence of an optically-thick torus determines an anisotropic obscuration of the nuclear region. From Urry & Padovani (1995).

Narrow Line Region (NLR) located farther from nucleus. The key ingredient of the Unified Model is an optically-thick torus, which prevents a direct view of the nucleus and of the BLR to equatorial observers. In this framework, the type 1/ type 2 bimodality is readily explained as an orientation effect. Namely, type 1 AGN will be those which are viewed

from a polar line of sight that does not intercept the obscuring torus. In radio-loud AGN the radio emission is due to a collimated jet of relativistic electrons that emits synchrotron radiation. The jet is absent in radio-quiet AGN.

This general picture of AGN anatomy is supported by solid observational evidence. For instance, the idea that an accretion disk surrounding a SMBH is present in AGN is strongly supported by the observations of relativistically broadened iron emission line in AGN X-ray spectra (see Reynolds & Nowak 2003, for a review). The line is thought to be produced by reflection (i.e. back-scattering) of the X-ray radiation coming from the hot corona near the disk. The observed line profile (e.g. in the prototypical case of MCG-6-30-15, Tanaka et al. 1995) is explained if both the relativistic Doppler distortion due to the orbital motion of the disk material around the black hole, and the gravitational redshift of the SMBH field (i.e. "clocks near black holes run slowlier") are considered.

A proof that the BLR gas is orbiting in the gravitational field produced by a SMBH is offered, for instance, by the so-called reverberation mapping (Peterson & Horne 2004). This consists in measuring the time delay after which a BL responds to changes of the optical/UV continuum. If interpreted as light-travel time ($\tau_{\mathrm{LT}} \sim r/c$, where c is the speed of light), this delay is a measure of the radius r at which the line is produced. This allows to directly measure the mass M of the SMBH assuming that the line width ΔV is simply due to Keplerian motion ($\Delta V^2 \sim M/r$).

Finally, a quite convincing evidence in favor of the Unified Model has been the discovery of polarized broad emission lines in e.g., the prototypical Seyfert 2 NGC 1068 (Antonucci & Miller 1985). This indicates that, although not visible, a BLR is still present in obscured AGN. The optical polarization of type 2 AGN, being perpendicular to the main source axis, is explained if the radiation coming from the BLR is scattered in our line of sight by free electrons located in a conical region along the pole of an obscuring torus coaxial with the source. Indeed, in this configuration, the torus prevents a direct view of the nuclear region and, at the same time suppresses the scattered light in a significant range of angles.

I.1.1   The accretion disk

The matter falling onto the central SMBH, before disappearing beyond the event horizon, orbits around it and forms an accretion disk. The inner radius of the disk R_{in} is nominally set by the radius of the innermost stable circular orbit (R_{ISCO}) of a test particle in the space-time metric around the black hole. Thus, ultimately, it depends on the black hole mass M and on its spin (Carter 1971). The same holds for the accretion efficiency $\eta = L_{\mathrm{bol}}/\dot{M}c^2$ (where L_{bol} is the bolometric luminosity of the disk and $\dot{M}$ is the mass accretion rate).

Theoretical calculations in a general relativity framework predict that the accretion disk around a classical, non rotating, Schwarzschild black hole starts at $6R_{\mathrm{g}}$ (where $R_{\mathrm{g}} = GM/c^2$ is the gravitational radius) and has an efficiency $\eta = 0.057$. When the black hole spin is included in the computation the Kerr metric has to be used. For a rotating Kerr black hole, R_{ISCO} decreases steeply as the spin increases, while the efficiency increases. For an asymptotic, maximally rotating black hole $R_{\mathrm{in}} = 1R_{\mathrm{g}}$ and $\eta = 0.42$ (e.g., Bambi 2012).

For a typical AGN hosting a black hole of 10^8 M$_\odot$, R_{g} is of the order 10^{-5} pc, which means

that the inner radius of the disk lies at a distance of a fraction of light hours from the black hole. At large radii the disk self gravity becomes important and the disk is unstable to self-fragmentation (Toomre 1964). This self-fragmentation radius, which is of the order $\sim 10^4 R_g = 0.1$ pc for a black hole mass 10^8 M$_\odot$, nominally defines the outer boundary of the disk.

At first approximation, the spectrum emitted by the accretion disk is modeled well by the classical Shakura-Sunyaev model of a geometrically-thin, optically-thick disk (Shakura 1973). This ideal disk emits a blackbody-like spectrum which is obtained by integrating the blackbody spectrum of a thin disk annulus over the radial temperature profile of the disk. The latter scales with the black hole mass as $M^{-1/4}$, which means that disks around lighter black holes are hotter and emit at shorter wavelengths (see e.g., Peterson 1997). For instance, the accretion disk around $\sim 10^8$ M$_\odot$ black hole radiates predominantly in the far UV part of the spectrum, while for $\sim 10^6$ M$_\odot$ black hole the peak of emission is in the extreme UV. Conversely, for stellar-mass black hole of few M$_\odot$, the peak of the disk emission is in the X-ray band.

I.1.2 The hot corona

The blackbody emission of the disk declines towards X-ray energies. The X-rays at energies above ~ 2.0 keV are thought to originate in a hot tenuous plasma which probably resides in the inner part of the accretion flow (Haardt & Maraschi 1991). The X-ray emission is produced via inverse Compton scattering of the disk-photons by the hot electrons of this corona. The resulting X-ray spectrum has a power-law shape with an exponential cutoff at high energies. The electron temperature of the corona (kT=20–100 keV) can be directly obtained by simultaneously measuring the slope and the high energy cutoff of the hard X-ray power law (see Malizia et al. 2014). On the other hand, observationally probing the location and the geometry of the X-ray emitting region is challenging (but see Reis & Miller 2013, and references therein). Recent results of X-ray spectral-timing analysis of AGN set the distance between the corona and the accretion disk to be in the 1–10 R_g range. Moreover, the rapid variability of the hard X-ray emission of AGN suggests that the corona is compact in size. Indeed, in a few gravitationally lensed quasars, the size of X-ray emitting region has been measured to be of the order of ~ 10 gravitational radii.

I.1.3 The line emitting gas

Emission lines from a variety of ionized species and with a bimodal line width (where the BL have a *FWHM* up to $\sim 10^4$ km s^{-1} and the NL of the order of 10^1 km s^{-1}) are observed across the electromagnetic spectrum of AGN. Broad Balmer hydrogen lines are prominent in the optical spectrum of type 1 AGN (Sulentic et al. 2000), while the UV band covers the transitions from the hydrogen Lyman series (Scott et al. 2004) and from more highly ionized carbon, nitrogen, and oxygen species (e.g., C IV, Bachev et al. 2004). Later, broad lines from e.g., O VII, Ne IX, have were also detected in the X-ray (Costantini et al. 2007, Detmers et al. 2011).

Conversely, NL are present in the spectra of both type 1 and type 2 AGN. In the optical

band, a narrow [O III] $\lambda\lambda$5007, 4959 Å doublet is typically seen. In the UV and in the X-ray spectrum of type 1 AGN NL are often difficult to be disentangled from either the prominent BL or the bright continuum. However, in some cases, a temporary low X-ray continuum allows the detection of a rich spectrum of X-ray NL, of which the O VII forbidden line is usually the most prominent line. (e.g., Whewell et al. 2015).

Photoionization is the most likely source of line excitation for the AGN circumnuclear gas (see Netzer 2008, for a review). A direct evidence in favor of this is, for instance the correlated line and continuum variations observed during reverberation mapping campaigns of Seyfert galaxies. Photoionization equilibrium (i.e. the balance between the ionization and the recombination rate) is reached at temperatures of the order $\sim 10^4$ K for a wide variety of astrophysical plasmas. The temperature of the line-emitting gas in AGN can be directly estimated using the measured ratios of the strengths of emission lines with different upper levels (Osterbrock 1989), such as [O III] [I(λ4959) + I(λ5007)] / I(λ4363). These measurements usually indicate a temperature typical of photoionization for the NLR gas.

Despite being both dominated by photoionization, under other respects the BLR and the NLR are two different gaseous environments. The absence of strong broad forbidden lines indicates that the gas in the BLR must have a density of the order of at least $\sim 10^8 \, \text{cm}^{-3}$. This is the critical density above which the [O III] forbidden line is collisionally suppressed. The geometry, the kinematics and the ionization conditions of the BLR gas can be probed using reverberation mapping techniques and photoionization modeling. The BLR size that is deduced from measurements of reverberation lags of e.g. the H_β line ranges between 10 and 100 light days (Peterson et al. 2004). Interestingly, the inferred BLR size correlates with the AGN optical luminosity as $\sim L_{5100}^{0.7}$ (where L_{5100} is the luminosity at 5100 Å, see Kaspi et al. 2000). This matches qualitatively with what is expected in a photoionization scenario, where the luminosity of the ionizing source regulates the size of the zone of ionized gas. High ionization lines are found to respond to continuum variations faster than low ionization lines, which indicates that the BLR gas is stratified in ionization. The spatial distribution of the line emission in the BLR has been modeled using the LOC (locally optimally emitting cloud, Baldwin et al. 1995) approach. This model is based on the idea that line-emitting clouds of gas of various density are distributed around the nucleus. Emission of a particular line comes predominantly from a location where clouds with optimal conditions for the emission of that line reside. The LOC model has been used to successfully model the optical and UV BLR (Korista et al. 1997, Korista & Goad 2000) and more recently, in a few cases, (e.g. Costantini et al. 2007) it has been extended to the X-ray BL.

In contrast to the BLR, the NLR does exhibit the [O III] forbidden transition which indicates a lower density of the emitting gas ($n = 10^3 - 10^6 \, \text{cm}^{-3}$, see a review from Netzer 1990). Another difference is that the NL are not observed to vary, even in sources undergoing drastic continuum changes. This suggests that the NL are emitted at larger distance from the center and that the NLR itself is spatially extended. Indeed, in nearby Seyfert 2 the NLR is spatially resolved and can be directly imaged (e.g., Circinus, Wilson et al. 2000, NGC 1068, Pogge 1988) . These studies indicate a conical geometry for the NLR gas, extended up to distances of the order of ~100 pc. The NLR is a complex gaseous environment, and

a LOC photoionization modeling is required to account for the observed properties of the optical/UV NLR (Ferguson et al. 1997). Concerning the X-ray NL, Bianchi et al. (2006) found that a density profile scaling like $\sim r^2$ is required to reproduce the observed [O III] to soft X-ray ratio observed in spatially resolved X-ray and optical images of the NLR in nearby Seyfert 2. For a tentative optical-to-X-ray photoionization modeling of the NLR in a nearby quasar see chapter 1.

I.1.4   The obscuring torus

A toroidally-shaped, dusty structure screening the central engine on the equatorial line of sight was firstly invoked in Antonucci (1993) to account for the observed type 1-type 2 AGN bimodality. The toroidal geometry of the obscuring medium was initially inferred from the observed optical polarization of type 2 AGN. The measured polarization angles can be explained by the presence of an absorber preventing the nuclear light to be scattered in a significant range of angles. A torus shape is the simplest configuration which achieves this effect. The observed biconical geometry of the ionized gas in NLR, that is not obscured by the torus, is also naturally explained in this geometrical configuration.

In the context of the Unified Model, the location of the inner edge of the torus, nominally separating it from the BLR, can be set by the dust sublimation radius beyond which dust grains can survive the AGN radiation field. This is ultimately regulated by the AGN luminosity (e.g., Krolik & Kriss 2001). Thus, it is at ~sub-pc scales in Seyfert objects and at ~pc scale at quasar luminosities.

Probing the location and the detailed geometry of the obscuring material in AGN is a crucial test for the current theoretical paradigm.

The dust in the torus absorbs the AGN X-ray/UV radiation and re-emits thermally at infrared wavelengths. The K band wavelength ($\sim 2.2 \mu$m) is close to the peak emissivity of the hottest dust. Thus, in this band, the reverberation lag technique probes the torus inner boundary (Suganuma et al. 2006, Kishimoto et al. 2007, Koshida et al. 2014, Pozo Nuñez et al. 2014). The time-lags measured in these experiments, which were successfully carried out for a handful of medium-to-low redshift AGN, are a factor 3-4 larger than those found in the optical for e.g. the Hβ broad emission line. This indicates that the BLR is limited in size (Landt et al. 2014) by the inner wall of the torus, which is in good agreement with the Unified Model.

At longer, mid-infrared (MIR) wavelengths (8–13 μm), colder dust can be probed. Recently, thanks to the significant improvements in the long-baseline IR interferometry offered by the ESO MID-infrared interferometric instrument (MIDI, see e.g., Jaffe et al. 2004, Burtscher et al. 2013) and the Astronomical Multi-BEam combiner (AMBER, see e.g., Weigelt et al. 2012), it has become possible to map the distribution the of MIR-emitting dust with an unprecedented spatial resolution of the order of few milliarcseconds. For a few well observed nearby sources, the detailed geometry of the dust emission could be revealed. For instance, Tristram et al. (2014) modeled the emissivity map of Circinus in three MIR bands. Roughly 20% of the MIR flux is emitted by a thin, centrally located, 1 pc large, disk like structure while the bulk (~80%) of the MIR emission comes from a second, thicker component, elongated along the polar direction. A somewhat similar structure

has been observed also in two other type-2 AGN (NCG 1068 Raban et al. 2009, and NGC 424. Hönig et al. 2012) and in the type-1 source NGC 3783 (Hönig et al. 2013). Moreover, 18 out 123 sources in the Asmus et al. (2016) sample show clear indication of an elongated MIR morphology, and it is argued that this detection rate is artificially lowered by e.g., the lack of sufficient high-quality datasets in the sample.

These findings challenge the simple torus paradigm of the Unified Model. While the hot, NIR-emitting dust may indeed be confined in a central small equatorial torus, much of the cooler dust may reside in an extended region having an elongated geometry and, possibly, a different dynamic (e.g., a wind, as argued in Hönig et al. 2012, 2013).

Indications for a more complex geometrical distribution of the obscuring material in AGN are provided also by studies the X-ray band (see Bianchi et al. 2012, and references therein). Recent results from X-ray variability studies indicate that some cold obscuring material, likely in the form of clumps, is present within the dust sublimation radius also in optically unobscured type 1 AGN (see Sect.I.3.2). These findings are naturally explained in the context of new theoretical models of non-uniform clumpy tori (Elitzur & Shlosman 2006, Nenkova et al. 2008, Hönig & Kishimoto 2010). These models are promising because as well as accounting for the time-variable X-ray obscuration, they also reproduce better the IR SED of both type 1 and the type 2 AGN over the full range of IR wavelengths covered (Nenkova et al. 2002).

In a clumpy torus framework the BLR, and the dusty torus are part of the same clumpy medium which decreases in ionization as the distance from the center increases. In this context, the AGN classification must be reinterpreted. The degree of obscuration is determined not only by the observer's viewing angle, but also by the cloud number density on the equatorial plane. When the cloud number density is low, the source may appear as an unobscured type 1 AGN even to equatorial observers.

All in all, while the classical model of a uniform axysimmetric torus has been proven to be inadequate by these, and others pieces of evidence, a new paradigm is far from being firmly set (see Netzer 2015, and references therein). The nature of the AGN obscurer remain uncertain and a comprehensive picture of how it forms, evolves and remains stable over a long period of time is still missing.

I.1.5   The relativistic jet

The synchrotron radio emission from a jet distinguishes radio-loud from radio-quiet AGN. Radio-quiet AGN are not always radio-silent, as in some cases they show evidence for weaker radio lobes (Panessa et al. 2014). For an overview of the observational properties of AGN jets see Hardee (2008). For the purpose of this thesis, it is important to clarify the difference between AGN jets and winds (see e.g., Königl 2006). A jet is a highly-collimated flow of relativistic particles, which emits non-thermal radiation. On the other hand, winds are less collimated flow of ionized gas, identified by their thermal emission signatures. The outflow velocity of a wind, even for the fastest cases, is always sub-relativistic ($v_{out} \leq 0.1c$).

I.2   Rationale of this thesis

The Unified Model has been an ambitious attempt of explaining a vast observational taxonomy using a small number of physical parameters. Namely, the source inclination with respect of the observer line of sight determine the detectability of the nucleus and of the optical/UV/X-ray BLR, while the presence (or the absence) of a jet determine the AGN radio-loudness (or quietness). Undoubtedly, this model has enabled a significant progress in our understanding of the AGN phenomenon. Nevertheless, some questions remain open (see e.g., Beckmann & Shrader 2012).

In this thesis we use X-ray spectroscopy to characterize the central engine and the circum-nuclear environment in some nearby AGN. Using high-resolution X-ray spectroscopy, it is possible to probe the physical conditions in the absorbing/emitting photoionized gas surrounding the black hole. This ionized material is often found to be part of a fast outflow. As we shall see, AGN winds are theoretically expected to have a profound impact on the surrounding galactic environment. For this reason, the possible impact of winds beyond the AGN boundary is currently a matter of investigation in observational astrophysics.

I.2.1   The role of winds in shaping the AGN environment

A potentially crucial additional ingredient in the AGN science is a wind energized by the black hole activity and interacting with the interstellar medium of the host galaxy.

From a theoretical point of view there are reasons to expect an important wind component in AGN. For instance, accretion disk winds of various kinds have been invoked in models for the formation of the jet (e.g., Blandford & Payne 1982) and of the torus clumpy medium (e.g., Elitzur & Shlosman 2006). It is also straightforward to prove that the AGN activity must somehow regulate the star-formation in the host galaxy. Indeed, a tight correlation between the mass of the central black hole and the stellar mass of the galactic bulge (the so-called M-σ relation, Merritt & Ferrarese 2001) holds. This relation naturally follows as a consequence of the so-called AGN feedback scenario. Detailed numerical simulations of the galaxy/black hole coevolution (Di Matteo et al. 2005, Scannapieco & Oh 2004, Sijacki et al. 2007, Hopkins et al. 2008, Hopkins & Elvis 2010) show that the energy output from the accreting SMBH results in powerful gas outflows. These winds effectively deplete the galaxy of its cold gas, thereby halting the star formation and preventing further black hole growth.

An accretion disk around a black hole can launch a wind, provided that either the gradient of gas pressure (thermal driving), or the radiation force (radiative driving) or the Lorentz force (magnetic driving) overcomes the gravitational force (see Proga 2007, for a review). Radiatively and magnetically driven disk winds are theoretically expected to reach the highest terminal velocities, of the order 10^4 km s^{-1} (Proga et al. 2000, Everett 2005). Fast disk winds are able to drive a large-scale outflow in the ISM of the host galaxy provided that energy is conserved in the wind-ISM interaction, i.e., that the shocked hot ISM does not radiatively cool on a timescale shorter than its flow time (King & Pounds 2015, and references therein). The large-scale outflow is able to clear up a galaxy of its gas as required in the AGN feedback scenario.

Outflows of different kinds are observed across the electromagnetic spectrum of AGN, from X-ray to radio wavelengths. Observations in different bands probe outflows in different phases, from the highly-ionized gas to the cold, molecular, gas. However, so far, observations of AGN outflows have not yet provided a firm confirmation of the AGN feedback scenario, nor have allowed to definitively discriminate between different wind driving mechanisms.

In the X-rays two classes of highly-ionized gas outflow are probed. The so-called ultrafast outflows (UFO) are highlighted by blueshifted absorption lines from the most highly-ionized iron species (Fe XXV–Fe XXVI). These highly-ionized winds reach mildly relativistic velocities (of the order ~0.1 c) and are believed to be accelerated out of the accretion disk, possibly via magnetic driving (Tombesi et al. 2012). Conversely, the so-called warm absorbers (WA, see Sect. I.4 for a detailed description) can be detected in both the X-ray and the UV band via narrow absorption lines (NAL) of several ionized species of e.g., Fe, Si, Mg, O, N, and, C. These are more gentle winds reaching velocities of the order of few thousands km s^{-1}.

An interesting class of AGN showing outflows in the optical/UV band are the so-called broad-absorption line quasars (BAL QSO, see Hamann & Sabra 2004 for a review). These sources display broad (with a typical width of 10^4 km s^{-1}) absorption troughs due to resonant transitions of ionized metals e.g., C IV, N V, O VI, Si IV, which are strongly blueshifted (from few 1000 to few 10 000 km s^{-1}) with respect to the source systemic velocity. Interestingly, in some cases the X-ray spectrum of BAL QSO requires a partially covering or ionized X-ray absorption, which can be variable on timescales as short as few hours. These UV/X-ray properties are consistent with the picture of a nuclear wind (e.g., Giustini et al. 2015).

At optical wavelengths, large scale (~ kpc, Harrison et al. 2014) galactic winds are revealed. Indicators in the optical band can probe the mildly-ionized, neutral, and dusty component of galactic outflows (Rupke & Veilleux 2013). These winds can in principle be driven by the stellar winds and supernovae generated in a powerful starburst or by the AGN activity or by a combination of the two. However, the high-velocity winds observed in QSO hosts (up to few thousands km s^{-1}) are difficult to be produced from a starburst alone (Rupke & Veilleux 2013).

In the infrared and in the submilimeter, transitions from a plethora of molecular species (e.g., OH, Sturm et al. 2011 and CO, Cicone et al. 2014) highlight massive outflows of cold, molecular gas. This phase of the outflow carries the largest amount of mass away from the galaxy and thus provide the most effective feedback. For instance, in the best-studied case of Mrk 231, the giant molecular outflow seen in CO (Feruglio et al. 2010), OH (Fischer et al. 2010), HCN, HCO+, HNC (Aalto et al. 2012), and, water vapor (González-Alfonso et al. 2010) has been shown to be able to expel the cold gas reservoir of the galaxy in about 10^7 yr (Feruglio et al. 2010).

Recently, in two notable cases (IRAS-F11119+3257 Tombesi et al. 2015 and Mrk 231 Feruglio et al. 2015), a nuclear UFO of highly-ionized gas and a galactic molecular outflow have been simultaneously observed. The energetics of these flows are consistent with a picture where energy is conserved in the wind/ISM interaction.

Finally, in the radio band outflows of neutral gas, with velocity ranging from few hundreds
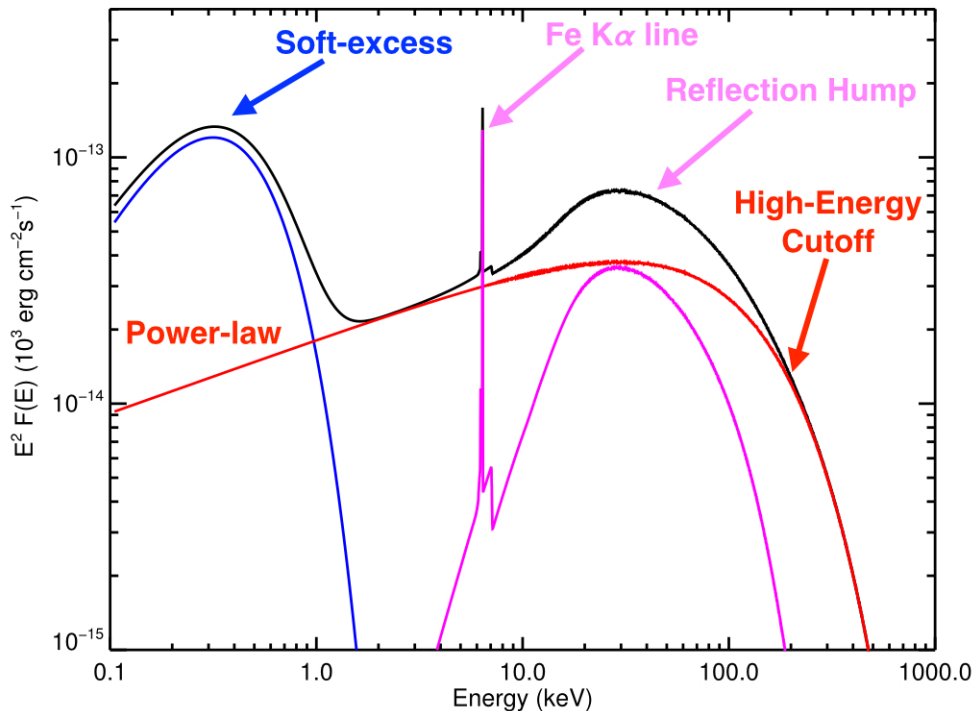
Figure I.2: Spectral components of the AGN continuum in the X-ray band. The most relevant spectral features are labeled.

up to a few thousands km s^{-1} have been discovered in a handful of radio-loud objects using the H I-line and/or the carbon monoxide (CO) transitions as tracers (see Morganti 2015, and references therein). In the best studied case (4C 12.50 Morganti et al. 2013), the Very Large Baseline Interferometer (VLBI) has imaged the H I outflow to be located off-nucleus, in a region of bright radio emission due the ongoing jet-ISM interaction. This proves that, in the case of radio-loud AGN, the activity of the jet is able to drive an outflow in the ISM of a galaxy (Wagner & Bicknell 2011, Wagner et al. 2012).

I.3   The broadband X-ray spectrum of AGN

Currently, the leading missions dedicated to X-ray astronomy are the ESA satellite X-ray Multi Mirror (XMM-*Newton*) and the *Chandra* satellite of NASA, that were both launched in 1999. Both these spacecrafts are equipped with X-ray detectors based on CCD technology (e.g., the EPIC camera Strüder et al. 2001, Turner et al. 2001 on board XMM-*Newton* and the ACIS detector on board *Chandra*), which are sensitive to X-rays in the 0.3–10.0 keV band. It is common in the terminology of X-ray astronomy to divide this bandpass

into a soft and a hard band, below and above 2.0 keV, respectively. With these non disper-sive instruments, especially with the XMM EPIC-pn which has a highest effective area among the current X-ray detectors, a low-resolution (e.g., for the EPIC-pn the spectral resolving power is R=20–50) but broadband spectroscopy of astrophysical sources can be performed. This is ideal, for instance, for accessing the physics producing the AGN continuum emission. Recently, the launch of the Nuclear Spectroscopic Telescope Array (NuStar, Harrison et al. 2013), which is the first X-ray telescope capable of focusing the hard X-ray light up to ∼80 keV, has expanded the high quality coverage of X-ray band to above ∼10 keV. As we shall see important features of the AGN continuum are expected in this energy range.

I.3.1   The X-ray spectral continuum

In Fig. I.2, we show the typical X-ray spectrum of a type 1 AGN, cleaned from any absorp-tion. This is a rather idealized case since the spectrum is often modified by absorption from both neutral and ionized gas along the line of sight. However, for clarity, we illustrate at first the spectral components of the intrinsic AGN continuum and hence in Sect. I.3.2 and in Sect. I.4 we describe the effects of cold and warm absorption on the spectrum, respectively. The knowledge of the continuum shape, especially in the soft X-ray band where most of the absorption features fall, is crucial for a correct absorption estimated. As shown in Fig. I.2, three main spectral components are typically needed to account for the X-ray continuum across the 10^{-1}–10^3 keV band. There is a general consensus about the origin of the X-ray emission above ∼2.0 keV. In this spectral range the emission is dominated by the Comptonized radiation of the hot corona (Sect. I.1.2). The predicted power-law shaped spectrum provides a good fit for both Seyfert and quasar objects. Typi-cal spectral slopes range between $\Gamma = 1.6 - 1.9$ (e.g., Bianchi et al. 2009, Piconcelli et al. 2005), with possible subtle differences between the quasar and Seyfert population. Re-cently, the advent of NuStar has opened the possibility of measuring the high-energy cutoff of the AGN X-ray continuum with an accuracy never achieved before (of the order of 10% in the best constrained cases, e.g., Brenneman et al. 2014, Marinucci et al. 2014a). The knowledge of both the spectral slope and of the cutoff energy allows to directly access the corona physical parameters (the temperature kT and the plasma optical depth τ).
A prominent iron line emerging over the X-ray continuum is ubiquitously detected in AGN. On average, the line peaks at the energy expected for the Kα transition of neutral iron (∼ 6.4 keV) and has an ubiquitous narrow profile (Jiménez-Bailón et al. 2005, Corral et al. 2008, Bianchi et al. 2009), which is barely resolved by current grating spectrome-ters (Yaqoob & Padmanabhan 2004). In some cases, a broad component (e.g., Nandra et al. 2007) can be disentangled from the narrow core. Reflection of the disk radiation in some neutral distant material (e.g., the obscuring torus, Matt et al. 1991) is a likely origin for the narrow core of the line. Conversely, the broad component may result from reflection by the disk material (Fabian 2006) or, sometimes, may be partially ascribed to the line-emitting gas in the BLR (e.g., Mrk 279, Costantini et al. 2010). For genuine disk-lines, relativistic effects may significantly affect the line profile (see Miller 2007, and references therein). Reflection processes produce also a continuum emission due to

electron scattering. The contribution of this reflected continuum to the total AGN X-ray spectrum becomes significant at hard energies. Indeed, if reflection occurs in a Compton thick material ($N_H \geq 10^{24}$ cm^{-2}), a broad hump is expected at 30–40 keV (Murphy & Yaqoob 2009).

In the majority of type 1 AGN, the combination of a primary and a reflected continuum is not sufficient to account for the emission at energies below ∼2.0 keV. At these energies a broad excess, which can be phenomenologically modeled as a blackbody at temperatures of the order of ∼150 keV (e.g., Piconcelli et al. 2005), is often seen. This so-called soft-excess (Singh et al. 1985) cannot be ascribed to the accretion disk, because the Wien tail of the disk blackbody emission is not expected to be strong at soft X-ray energies (Sect. I.1.1).

There is no general consensus about the origin of the soft-excess. Comptonization of the disk photons in a warm, optically plasma is a viable mechanism to extend the disk emission to soft X-ray energies. The Comptonizing plasma may reside in the inner regions of the accretion disk, (Done et al. 2012) or in an extended corona located above it (Petrucci et al. 2013).

Another possible explanation invokes reflection of the primary radiation in an ionized disk (Ross & Fabian 2005). The soft X-ray spectrum of the reflected radiation would contain a wealth of fluorescence emission lines. According to this so-called light-bending model, in the case of disk reflection, the strong gravity in the vicinity of the black hole smoothen these lines in a pseudocontinuum, thereby creating the observed excess. A rapidly spinning black hole is often required in this model to justify the extreme relativistic blurring (e.g., Crummy et al. 2006).

Finally, other authors (Turner et al. 2009) have proposed that the soft X-ray spectrum of AGN is dominated by absorption in a patchy medium, which partially covers the source. As a consequence of the partial-covering, there is a leakage of flux at lower energies that modifies the continuum slope. This absorption may arise for instance in a clumpy disk wind, located within the BLR.

X-ray spectral fitting alone is not sufficient to distinguish among these models. Even in high quality dataset, (e.g., MCG 6-30-15, Ballantyne et al. 2003, Miller et al. 2008) models with drastically different physical assumptions are equally able to account for the observed spectral shape. Complementary experiments, exploiting for instance the informations contained in the time domain, may, in some cases provide a discriminating evidence. For instance, during a multiwavelength monitoring campaign of the bright Seyfert 1 Mrk 509, the UV flux followed the variability of the soft-excess (Mehdipour et al. 2011). This is easily interpreted as a Comptonization framework, where the optical/UV disk photons directly feed the Comptonizing the corona. A reflection scenario would more naturally predict a correlation between the soft-excess and the hard X-ray flux above ∼10 keV, because of the Compton reflection hump expected at ∼ 30 keV. This correlation is absent in the Mrk 509 case.

On the other hand, recent observations of short time lag between variation in the soft X-ray band with respect to the hard X-ray band (De Marco et al. 2013) have been successfully explained in a reflection based scenario (Fabian et al. 2009, Cackett et al. 2013).

I.3.2   X-ray variability

AGN are variable X-ray sources. For instance, early on it was noticed (Matt et al. 2003) that the spectra of some type 2 AGN taken at different epochs show drastic changes in both flux and spectral shape. Prompted by this finding, in the last ten years many studies have been dedicated to AGN spectral variability and a rich phenomenology has emerged. Spectral variations have been observed on timescales ranging from few hours up to few years, in both type-2 and type-1 AGN. This is often ascribed to a variable absorption of the X-ray radiation along the line of sight. For instance, on these timescales many type 2 AGN (e.g., NGC 7582, Piconcelli et al. 2007, UGC 4203, Risaliti et al. 2010, and, NGC 454 Marchese et al. 2012) have been observed to change look, switching from a Compton-thick state ($N_H \geq 10^{24}$ cm^{-2}) to Compton thin state ($N_H \leq 10^{24}$ cm^{-2}). Variations in the absorbing column density and/or covering fractions have been observed also in some, on average unobscured, type 1 sources. (e.g., NGC 4151, Puccetti et al. 2007, 1H 0557-385, Longinotti et al. 2009, and, SWIFT J2127.4+5654, Sanfrutos et al. 2013.) This ubiquitous rapid variability suggests that some cold X-ray absorbing material must be present in the vicinity of the central engine, even in optically unobscured AGN (Bianchi et al. 2012). This material is probably patchy and may belong to the BLR itself or to a clumpy torus extending inward beyond the dust sublimation radius (Miniutti et al. 2014).

The clumpy nature of the absorption is unambiguously witnessed by recent observations of rapid occultation and de-occultation of the X-ray source. For instance, in the best studied Seyfert 1.8 NGC 1365, a 10-hours long eclipse has been observed (Risaliti et al. 2009). Assuming a simple picture of a cloud orbiting at Keplerian velocity, the observed crossing time of the line of sight implies that the cloud is moving at $v \gtrsim 10^4$ km s^{-1} at a distance of $\sim 10^4 \, R_g$ from the nucleus. In this scenario, the inferred physical properties of the cloud (physical size of the order of 10^{13} cm and density of 10^{10}–10^{11} cm^{-3}) are typical for the BLR material. The case of Mrk 766 (Risaliti et al. 2011) indicates that eclipsing events occur also in type 1 sources. For instance, a systematic search for eclipse events in the vast archive of AGN light curves of the Rossi X-ray timing explorer (RXTE) has encountered eight objects with multiple events (Markowitz et al. 2014).

The variable absorption can coexist with relativistic disk reflection (e.g., NGC 1365, Risaliti et al. 2013, and MCG 6-30-15 Marinucci et al. 2014b) or with a Comptonized soft-excess (e.g., NGC 5548, Mehdipour et al. 2015). In a disk reflection scenario, a variety of possible spectral appearances are predicted as the geometry of the disk-corona system changes (Miniutti & Fabian 2004). Namely, when the primary X-ray emitting spot migrates closer to the black hole, because of the stronger gravity, the radiation will be focused down to the disk, without reaching the observer. In the most extreme conditions, a low-flux, flat spectrum is predicted. For the case of e.g., Mrk 335 (Wilkins & Gallo 2015), the variable light bending may be alone sufficient to explain the spectral history of the source. In this context, in chapter 2 we test the light-bending model against a scenario based on Comptonization and variable absorption for the long-timescale variable X-ray spectrum of the bright Seyfert 1 1H 0419-477.

The analysis reported in chapter 3 of this thesis is related to the dramatic spectral changes that we witnessed in 2013, during an optical/UV/X-ray/gamma-ray observational cam-

paign dedicated to the prototypical Seyfert 1 NGC 5548. The coincidence between this historical spectral transition and our monitoring campaign provided a unique opportunity to investigate the cause of this unusual event. During the campaign, the source was ~25 times weaker at soft X-rays than the long-term average, while behaving almost normally at energies above ~2.0 keV. At the same time, in the UV it shows broad absorption troughs in the blue wings of e.g., the Lyα, C IV, and N V, broad emission lines, that were never present before. In Kaastra et al. (2014) we propose that all these changes are due to the onset of a weakly ionized, fast wind, located within or just outside the BLR, which blocks 90% of the soft X-ray flux in our line of sight. In chapter 3 we show that the rapid variability of this newly discovered obscurer is consistent with the picture of a patchy wind. Whether the obscuring wind in NGC 5548 is a unique case or a common mode of AGN variability is an intriguing question that deserves further investigations.

I.4   AGN ionized outflows

In the last fifteen years, thanks to advent of high resolution X-ray grating spectrometers, such as the Reflection Grating Spectrometer (RGS, den Herder et al. 2001) on board XMM-*Newton* and the low/high energy transmission grating spectrometers (LETGS, Brinkman et al. 2000, and HETGS, Canizares et al. 2005) on board *Chandra*, the field of X-ray spectroscopy has been revolutionized. With these instruments, an unprecedented spectral resolving power of R=200–1000 has become available, allowing for the first time a detailed diagnosis of the physical conditions (kinematics and ionization state) of the absorbing/emitting gas in a variety of astrophysical sources.
An advantage of X-ray spectroscopy compared to other wavelengths is that a larger bandpass is covered. Thus, numerous transitions of abundant elements such as iron, neon, oxygen, nitrogen, and carbon can be detected in a single X-ray observation. For instance, the Fe I and the O I absorption edges from a neutral gas fall in the X-ray band. X-ray transitions from ionized gas comprises a wealth of lines and edges from both lowly-ionized iron (Fe II–Fe XXIV) and oxygen (O IV–O VI), up to helium-like and hydrogen-like oxygen (O VII–O VIII), carbon (C V–C VI), nitrogen (N VI–N VII) and neon (Ne IX–Ne X). In 15 years of XMM-*Newton* and *Chandra* operations, many of these transitions have been detected both in absorption and in emission in several high resolution X-ray spectra of AGN up a redshift z of ~0.1.

I.4.1   Warm absorber diagnostics in the X-ray and in the UV bands

A warm absorber is identified in the X-ray and in the UV spectrum of type 1 AGN via the detection of narrow absorption lines (NAL) from several ionized species of e.g., Ne, O, Fe, C, N, Mg, and Si. These lines are usually blueshifted with respect to the systemic velocity, which indicates a global outflow of absorbing gas. Transitions from low ionization species (e.g., Mg II, C II–C IV, and, Si II–Si III) are seen in the UV. Conversely, high ionization species (e.g., Ne IX–Ne X, and, O VII–O VIII) produce only X-ray features. Ions like e.g., O VI, which produces features in both bands, are suitable to investigate the connection between the

UV and the X-ray absorber.

From a single X-ray or UV spectral observation, the kinematics and the ionization conditions of the gas can in principle be estimated. However, the current UV spectrometers are sensitive to details of the velocity structure that are not resolved in the X-ray. On the other hand, determining an accurate solution for the gas ionization parameter ξ using only few UV transitions is difficult. This is not the case in the X-ray, where dozen of transitions are typically detected. For instance, the M shell transitions from many ionized iron species form a deep unresolved transition array (UTA) which is a typical feature of X-ray warm absorbers. The shape of this trough is also sensitive to small variation of the ionization parameter (Netzer 2004). For these reasons, the combination of X-ray and UV spectroscopy provides the best possible diagnostics of the physical conditions in the outflow.

In a spectral observation, the kinematics of the gas is determined straightforwardly from the Doppler shift of the absorption lines. Moreover, individual ionic column densities can be readily derived from the observed depth of the absorption lines. In the UV, a velocity dependent covering factor (Arav et al. 2002) has to be considered in the column density determination. The global properties of the absorbing gas, namely the global hydrogen column density $N_{\rm H}$ and gas ionization parameter ξ can also be accessed by fitting the numerous X-ray features with a synthetic model of a photoionized absorber (e.g., XABS, Kaastra et al. 1996). In these models the ionic column densities of different elements are linked to each other through the ionization balance prescribed by the Spectral Energy Distribution (SED) of the source. The ionization balance is computed through a photoionization code, such as Cloudy (Ferland et al. 2013) or XSTAR (Kallman 1999).

Besides characterizing the physical conditions in the outflow, the aim of the study of warm absorbers is to ascertain whether these winds are energetically important for the AGN feedback scenario. This can also be evaluated from spectroscopic observables.

According to theoretical models, the outflow can provide an effective feedback if its kinetic luminosity is comparable (i.e., between 0.5% and 5%, Hopkins & Elvis 2010, and references therein) with the AGN bolometric luminosity $L_{\rm bol}$. The kinetic luminosity is simply given by $L_{\rm kin} = \dot{M} v^2 / 2$, where v is the outflow velocity and $\dot{M}$ is the mass outflow rate. The latter scales as $\sim v\, N_{\rm H}\, r$ (e.g., Crenshaw et al. 2003b) and thus depends critically on the distance r of the outflowing gas from the nucleus.

Moreover, it depends on the geometry of the outflow, which is difficult to determine. It is often assumed (Blustin et al. 2005) that the outflow is a partially filled spherical shell of gas, with an opening angle Ω and a volume filling factor f. An average value of $\Omega = 1.6$ is derived assuming that 25% of AGN are type 1 (Maiolino & Rieke 1995) and that the covering factor of these outflows is roughly 50% (Crenshaw et al. 2003b). An analytical expression for the volume filling factor f can be derived from the prescription that the momentum of the outflow must be of the order of the momentum of the absorbed radiation plus the momentum of the scattered radiation. Namely, $\dot{M} v \sim \dot{P}_{\rm abs} + \dot{P}_{\rm sc} = \frac{L_{\rm abs}}{c} + \frac{L_{\rm ion}}{c}(1 - e^{-\tau_{\rm T}})$ where $L_{\rm abs}$ is the luminosity absorbed by the outflow in the 1–1000 Ry range, $L_{\rm ion}$ is the source ionizing luminosity in the same range, and $\tau_{\rm T}$ is the optical depth for Thompson scattering.

Provided that the density n of the absorber is known, the distance r can be in principle

determined from the definition of ionization parameter $\xi = L_{\mathrm{ion}}/n r^2$ (Tarter et al. 1969). In the UV the gas density can be in some cases directly diagnosed using some density-sensitive lines (e.g., Si II, Si III, C II, C III, and, Fe III) from collisionally-excited metastable transitions (Bautista et al. 2009).

Alternatively, the recombination timescale of a particular ion can also be used as a density indicator, as it scales like $\sim n^{-1}$. This timescale can be accessed by searching for absorption line variability in response to continuum variation and measuring the delay (or the lack of delay) in the response of a particular line. Depending on the timescales that one wants to test, this is feasible with either a single long observations (e.g., Krongold et al. 2007) or extensive monitoring campaigns (e.g., Kaastra et al. 2012). When none of these density indicators is available some milder constraints can still be put on the gas location. These are derived from some general considerations (Blustin et al. 2005). The prescription that the velocity of the outflow must be greater than the escape velocity from the black hole ($v \geq \sqrt{\frac{2GM}{c^2}}$) sets a lower limit for the distance. Conversely, an upper limit of $r \geq \frac{L_{\mathrm{ion}} f}{N_{\mathrm{H}} \xi}$ (where f is the volume filling factor) is derived if the thickness of the outflowing shell is not greater than its distance from the center. These constraints on the distance, although quite approximated, are in most cases sufficient for an order of magnitude evaluation of the contribution of the wind for the AGN feedback.

I.4.2   Observed properties of warm absorbers

Ionized outflows are common in AGN. About 50% (Crenshaw et al. 2003b) of radio-quiet Seyferts 1 host a warm absorber. Typical absorbing column densities range between 10^{20}–10^{23} cm^{-2}while the observed outflow velocities are of the order of few hundreds up to few thousands km s^{-1}(McKernan et al. 2007). Recently, warm absorbers analogous to those found in radio-quiet AGN have been discovered also in the X-ray spectrum of radio-loud objects (Torresi et al. 2012, and references therein). However, for radio-loud objects, the statistics of X-ray WA studied at grating resolution comprises of only four sources, including the case of 4C +74.26 that we present in Chapter 3.

In the last fifteen years UV/X-ray observational campaigns have been performed for some nearby Seyfert 1 (Costantini 2010, and references therein) unveiling the detailed structure of the outflow. Warm absorbers are multicomponents winds, covering a wide range in ionization parameter and in velocity even in the same object. The combination of X-ray and UV spectroscopy provides the complete census of the ionization and velocity components of the outflow. Hence, the interplay between the X-ray and the UV absorbing gas can be explored by comparing the gas kinematics and the ionic densities independently derived in each band.

Usually at least some of the UV and X-ray components share, within the uncertainty due to the lower X-ray spectral resolution the same kinematics (e.g., NGC 3783, Kaspi et al. 2002a, NGC 4051, Kraemer et al. 2012, and, Mrk 509, Ebrero et al. 2011). Moreover, in some cases, (e.g., Mrk 279, Arav et al. 2007) a correspondence in the ionic column densities of common ions is found, provided a covering factor acting in the UV band. These findings suggest that the UV and X-ray absorber are the manifestation of the same, composite

outflow.

Nevertheless, determining how the different gas phases are geometrically and physically related is not trivial. From the kinematical correspondence it is often inferred that the UV and the X-ray absorbing gas may be co-located (Ebrero et al. 2011). Some authors (e.g., Kraemer et al. 2012) have suggested a scenario where the UV absorbing gas is in the form of colder clumps embedded in a flow of tenuous and more highly ionized gas. This may be the case for the outflow in NGC 3783, where the high-ionization UV components have been found to have pressures similar to those of the three X-ray ionization components, (Gabel et al. 2005) which are thermally stable (Netzer et al. 2003). In other cases, the distance estimations indicate that the highly ionized components are located much closer to the black hole than lowly-ionized components (e.g., NGC 4593 Ebrero et al. 2013). This is suggestive of a stratification of the ionized matter in the wind.

The quest of measuring the density of the absorber to infer its distance has led to many studies of the WA variability on short timescales. Changes in the WA opacity or ionization were observed for instance in NGC 3783 (~31 days, Krongold et al. 2005) and NGC 4051 (few ks–few months, Krongold et al. 2007, Steenbrugge et al. 2009). On the other hand, assessing the WA variability on long (e.g., ~years) timescales requires that high quality multi-epoch spectroscopy is available, which is seldom the case. A multi-epoch study of the WA was attempted, for instance, in the case of Mrk 279 (Ebrero et al. 2010) without finding significant variability. A more noticeable long-term variability of the WA was observed, for instance, in Mrk 335 (Longinotti et al. 2013) where the emergence of an ionized outflow that was not historically present was observed in 2009. In this respect the WA variability that we observed during the 2013-2014 observational campaign of NGC 5548 is an outstanding case. We found that the WA has recombined in response to the dramatic lowering of the ionizing flux caused by the inner obscurer that we discovered during the campaign (Kaastra et al. 2014). Signatures of the lower-ionization WA are indeed seen in the UV and in the X-ray spectra taken during the campaign (see Arav et al. 2015 and chapter 3). In most cases, obtaining accurate estimation of the location of the absorber is not possible. Direct density indicators are rarely detected, and when available, they constrain the location only for the specific outflow component to which they belong. So far, density-sensitive lines have been detected in the UV in a handful of sources (Kraemer et al. 2006, Gabel et al. 2005, Arav et al. 2015). Attempts of measuring the gas density via the line variability have sometimes led to undetection (which implies however a robust lower limit for the distance e.g., Kaastra et al. 2014, Arav et al. 2012) or to contradictory results (Krongold et al. 2007, Steenbrugge et al. 2009, e.g., NGC 4051). Recently, Crenshaw & Kraemer (2012) have made the census of the distance estimations available so far for the well known X-ray/UV absorbers. They found that in nearby Seyferts the absorbers are located between ~0.01 and ~100 pc from the center, i.e., outside the BLR and inside the NLR. This range of location is consistent with a scenario where the wind originate via photoionized evaporation of matter off of the surface of the obscuring torus (Krolik & Kriss 2001).

A connection between the WA and the line emitting gas in the NLR has also been suggested in some cases (Behar et al. 2003, Detmers et al. 2009). However, accurate distance estimation of the WA and detailed multiwavelength photoionization modeling of the NLR

are needed to set a connection on a firm basis.

The kinetic luminosity carried by the warm absorber is usually modest ($\lesssim 0.1\% L_{bol}$, Costantini 2010, and references therein). Thus, these ionized outflows are not expected to produce a significant feedback in the AGN environment. However, in a recent theoretical modeling of the wind/ISM interaction (Hopkins & Elvis 2010), the energy needed for an effective feedback has been found to be an order of magnitude lower ($\sim 0.5\% L_{bol}$) than what was previously thought ($\sim 5\% L_{bol}$). Interestingly, Crenshaw et al. (2015) have shown that the energetics of the outflow in NGC 4151, exceeds this lower benchmark if the outflow discovered in the NLR of this AGN is summed up with the classical warm absorber.

I.5 This thesis

In the cases of study treated in this thesis (1H 0419-577, NGC 5548, and, 4C +74.26) we draw a geometrical picture of the AGN gaseous environment, thanks to the analysis of the X-ray data. In each of these cases we detected an AGN outflow, with quite different characteristics.

The main results of this thesis are the following.

- In chapter 1 we analyze the longest exposed high-resolution X-ray spectrum ever taken of the Seyfert 1.5 galaxy 1H 0419-577. This was acquired as a part of a UV/X-ray campaign dedicated to this source. A simultaneous optical spectrum was also used in the analysis. We detect a thin, lowly ionized warm absorber, which is consistent to be one and the same with a galactic scale outflow detected in the UV. This is the first X-ray absorber ever detected so far away from the nucleus. Thanks to the optical/UV/X-ray spectral coverage, we could also attempt a multivawelength photoionization modeling of the narrow emission lines. The line-emitting gas is located much closer to the nucleus, at ~pc distance. Our photoionization analysis suggests the NLR is a complex gaseous environment, stratified both in ionization and in density.

- In chapter 2 we focus on the broadband optical-to-X-ray spectrum of the same source. We successfully model it using a Comptonization model, where the disk-photons are up-scattered to X-ray wavelengths by two intervening layers of plasma having different temperatures and optical depths. The X-ray photons above ~2.0 keV are produced in the classical hot, optically thin corona. Conversely, softer X-ray photons are produced in an another corona, which is warm and optically thick. In this framework the historical spectral variability of this source is readily explained as due to a neutral absorber with a variable opacity which intervenes in the line of sight. We speculate that the variable X-ray absorption originates in the innermost dust-free region of a clumpy torus.

- In chapter 3, we analyze several high resolution X-ray spectra that were taken in 2013-2014 in the context of a multi-satellite observational campaign of the prototypical

Seyfert 1 galaxy NGC 5548. During the campaign, we discovered the source in an unusual condition of heavy and persistent soft X-ray obscuration. We find that this newly discovered obscurer is rapidly variable, on timescale as short as two days, both in column density and in covering fraction. This is consistent with the picture of a patchy wind. In September 2013, the source underwent a two-week long re-brightening. Our analysis of the September 2013 spectrum indicates that this is a flare of the intrinsic continuum. This temporary flux enhancement provided a unique occasion to disentangle the WA features from the obscured continuum. We detect absorption from Fe-UTA, O IV-O IV, which are consistent to belong to a lower-ionized counterpart of the historical NGC 5548 warm absorber. This confirms that the WA has recombined in response to the lowering of the ionizing flux caused by the inner obscurer.

- In chapter 4, we model the X-ray absorption of the giant radio-loud quasar 4C +74.26. We clearly disentangle from the heavy Galactic absorption a highly-ionized outflow ($v \sim 3600\,\mathrm{km\,s^{-1}}$) located at the redshift of the source. This is one of the few cases so far of a well-characterized WA in a radio-loud galaxy. We discuss a scenario where the ionized gas flows along the polar axes of the source and cause an apparent redshift of the polarized Hα line. The kinetic luminosity carried by the outflowing gas is insufficient to produce a significant AGN feedback in this quasar.

1 ⸺ Simultaneous XMM-*Newton* and HST-COS observation of 1H 0419-577: The absorbing and emitting ionized gas.

.... **Abstract** ....

In this paper we analyze the X-ray, UV, and optical data of the Seyfert 1.5 galaxy 1H0419-577 with the aim of detecting and studying an ionized-gas outflow. The source was observed simultaneously in the X-rays with XMM-*Newton and in the UV with HST-COS. Optical data were also acquired with the* XMM-*Newton Optical Monitor. We detected a thin, lowly ionized warm absorber (*$\log \xi \approx 0.03$, $\log N_{\mathrm{H}} \approx 19.9$ *cm*$^{-2}$*) in the X-ray spectrum, which is consistent to be produced by the same outflow already detected in the UV. Provided the gas density estimated in the UV, the outflow is consistent to be located in the host galaxy at* $\sim$ *kpc scale. Narrow emission lines were detected in the X-rays, in the UV and also in the optical spectrum. A single photoionized-gas model cannot account for all the narrow lines emission, indicating that the narrow line region is probably a stratified environment, differing in density and ionization. X-ray lines are unambiguously produced in a more highly ionized gas phase than the one emitting the UV lines. The analysis also suggests that the X-ray emitter may just be a deeper portion of the same gas layer producing the UV lines. Optical lines are probably produced in another disconnected gas system. The different ionization condition and the* $\sim$ *pc scale location, suggested by the line width for the narrow lines emitters, are evidences against a connection between the warm absorber and the narrow line region in this source.*

....

1.1   Introduction

Active galactic nuclei (AGN) are believed to be powered by the accretion of matter onto a supermassive black hole (Antonucci 1993). Emission and absorption lines in AGN spectra are the signatures of a plasma photoionized by the central source. High-resolution spectral observations can probe the physical conditions in this gas, providing information about the interaction between AGN radiation and the surrounding environment.

A variety of emission lines with different width (from 10^2 to 10^4 km s^{-1}) can be identified in AGN type 1 spectra. The diverse line broadening reflect a different location of the emitting region: narrower lines are believed to originate in a region far ($\sim$100 pc) from the black hole, which is lower in density and in temperature than the broad line region (BLR), where broader lines are emitted (Osterbrock 1989). Line emission ranges from the optical (e.g. [O III], hydrogen Balmer series) to the X-ray waveband (e.g O VII, O VIII, Ne IX). Narrow lines may be more difficult to detect. For instance, narrow lines (NL) in the UV from e.g. C IV and O VI are blended in a dominant broad component and difficult to disentangle (e.g. Kriss et al. 2011). In the soft X-ray, the flux of any emission line is usually outshone by the underlying continuum and lines detection is favored by a temporary low-flux state of the source (e.g. NGC 4051, Nucita et al. 2010). Whether X-ray lines arise in the same gas emitting the longer-wavelength lines is an open issue that has been recently addressed through multiwavelength photoionization modeling. In the case of Mrk 279, X-ray broad lines are consistent to be produced in a highly-ionized skin of the UV and optical BLR (Costantini et al. 2007). Bianchi et al. (2006) found that a single medium, photoionized by the central continuum, may produce the [O III] to soft X-ray ratio observed in spatially resolved images of the narrow line region (NLR).

Besides the line-emitting plasma, another photoionized gas component that can modify the spectra of type 1 AGN is a warm absorber (WA) which intervenes in the line of sight. WA are commonly detected in about half of type 1 AGN (Crenshaw & Kraemer 1997, Piconcelli et al. 2005) via UV and/or X-ray absorption lines. These lines are usually blueshifted, (see Crenshaw et al. 2003b) indicating a global outflow of the absorber. In the past ten years, multiwavelength UV-X-ray campaigns (see Costantini (2010) and references therein) have depicted the physical conditions in the outflowing gas in great detail. WA are multi component winds spanning a wide range in ionization and in velocity (e.g., Kriss et al. 2011, Ebrero et al. 2011). X-ray spectra show the the most highly ionized lines (e.g., from O VII, O VIII and Ne IX), while a lower ionization phase (e.g.,C II, Mg II) is visible only in the UV. In some cases (e.g., NGC 3783, NGC 5548, NGC 4151, Mrk 279), a common phase producing e.g. O VI lines in both the UV and the X-ray spectrum has been identified (Kaspi et al. 2002b, Steenbrugge et al. 2005, Kraemer et al. 2005, Arav et al. 2007). Similarities in the line width (NGC 3783, Behar et al. 2003) and in the gas column density (NGC 5548, Detmers et al. 2009) suggest a connection between the WA and the gas in the NLR. However, the origin of WA is not clearly established yet, mainly because of the great uncertainty in estimating its location.

Provided the gas density, the distance of the outflow from the central source can be in principle derived from the gas ionization parameter $\xi = L_{\mathrm{ion}}/nR^2$ (where L_{ion} is the source ionizing luminosity, n is the gas density, and R is the distance from the ionizing

source). However, the gas density in most cases is unknown, and the distance may just be estimated indirectly (Blustin et al. 2005). Absorption lines from collisionally excited metastable levels may provide a direct density diagnostic (e.g. Bautista et al. 2009), but they are rarely detected. In the UV, metastable lines from e.g. Fe II, Si II, and C II have been detected in a handful of cases (e.g. Moe et al. 2009, Dunn et al. 2010, Borguet et al. 2012). In the X-rays the identification of metastable lines from O V is hampered by uncertainties in the predicted line wavelength (Kaastra et al. 2004). So far, available estimations, using different methods, have located the outflows within the BLR (e.g., NGC 7469, Scott et al. 2005) or have located them as far as the putative torus (e.g. Ebrero et al. 2010). In some quasars, a galactic scale distance has been reported. (Hamann et al. 2001, Hutsemékers et al. 2004, Borguet et al. 2012, Moe et al. 2009).

The distance estimation allows quantifies the amount of mass and energy released by the outflow into the medium. Hence, it is possible to establish, if WA contributes to the AGN feedback, which is often invoked to explain the energetics and the chemistry of the medium to a very large scale (Sijacki et al. 2007, Hopkins et al. 2008, Somerville et al. 2008, McNamara & Nulsen 2012). Warm absorbers usually produce a negligible feedback (e.g. Ebrero et al. 2011). Only the fastest AGN wind (e.g. Moe et al. 2009, Dunn et al. 2010, Tombesi et al. 2012) may be dynamically important in the evolution of the interstellar medium (Faucher-Giguère & Quataert 2012).

In this paper, we analyze a long-exposure XMM-*Newton* dataset of the bright Seyfert galaxy 1H 0419-577, which was taken simultaneously with a Cosmic Origins Spectrograph (HST-COS) spectrum. The source is a radio-quiet quasar located at redshift z=0.104 and is spectrally classified as a type 1.5 Seyfert galaxy (Véron-Cetty & Véron 2006). Using the Hβ line width, Pounds et al. (2004a) derived a 1.3×10^8 M$_\odot$ mass for the supermassive black hole (SMBH) hosted in the nucleus. The HST-COS spectrum has been published by Edmonds et al. (2011, herafter E11). The UV spectrum displays broad emission lines from C IV, O VI, and Lyα and absorption lines (E11). Three outflowing components were identified in absorption with the line centroids located at $v_1 = -38$ km s^{-1}, $v_2 = -156$ km s^{-1}, and $v_3 = -220$ km s^{-1} in the rest frame of the source. Only a few ionized species (H I, C IV, N V, O VI) were detected in component 1, while component 2+3 displays a handful of transitions from both low (e.g., C II) and high-ionization species (e.g. C IV, N V, O VI).

The present analysis is focused mainly on the high-resolution spectrum collected with the Reflection Grating Spectrometer (RGS, den Herder et al. 2001); in a companion paper, we will present the broad band X-ray spectrum of this source. Analysis of a previous RGS dataset is reported in Pounds et al. (2004b). Hints of narrow absorption features from an Fe unresolved transition array (UTA) were noticed in the spectrum. However, the short exposure time (~ 15 ks) has so far prevented an unambiguous detection and characterization of a warm absorber in this source.

The paper is organized as follows: in Sect. 2.3, we present the XMM-*Newton* observations and the data reduction; in Sect. 1.3, we describe the spectral energy distribution of the source; in Sect. 1.4, we discuss the spectral analysis; in Sect. 1.5, we model the narrow emission lines of the source; in Sect. 1.6, we compare the X-ray and the UV absorber; in Sect. 2.6, we discuss our results and in Sect. 1.8, we finally present the conclusions. The cosmological parameters used are: H_0=70 km s^{-1} Mpc^{-1}, Ω_m=0.3 and Ω_Λ=0.7. Errors are

Table 1.1: XMM-Newton observation log for 1H 0419-577

Observation ID	0604720401	0604720301
Date	28/05/2010	30/05/2010
Orbit	1917	1918
Net exposure (ks) [a]	61	97
RGS Count Rate (s^{-1})	0.337 ± 0.002	0.385 ± 0.002
EPIC-pn Count Rate (s^{-1})	1.41 ± 0.02	1.56 ± 0.02

Notes. [a] Resulting exposure time after correction for flaring.

quoted at 68% confidence levels ($\Delta \chi^2 = 1.0$) unless otherwise stated.

1.2 Observations and data preparation

In May 2010, two consecutive exposures of 1H 0419-577 were taken with the XMM-*Newton* X-ray telescope with both the EPIC cameras (Strüder et al. 2001, Turner et al. 2001) and the RGS. Moreover, optical monitor (OM, Mason et al. 2001) imaging mode data were acquired with four broad-band filters (B, UVW1, UVM2, UWV2) and two grism filters (Grism1-UV and Grism2-visual). The source was observed for ~ 167 ks in total, and a slight shift in the dispersion direction was applied in the second observation. In this way, the bad pixels of the RGS detectors were not at the same location in the two observations, allowing us to correct them by a combination of the two spectra (see Sect. 1.2.1). Details of the two observations are provided in Table 1.1.

1.2.1 The RGS data

For both RGS datasets, we processed the data following the standard procedure [1] using the XMM-*Newton* Science Analysis System (SAS, version 10.0.0) and the latest calibration files. We created calibrated event files for both RGS1 and RGS2, and to check the variation of the background, we also created the background light curves from CCD 9. The background of the first observation was quiescent, while the second light curve showed contamination by soft protons flares. We cleaned the contaminated observation by applying a time filter to the event-files: for this purpose, we created the good time intervals (GTI) by cutting all the time bins in the light curve where the count rate was over the standard threshold of 0.2 counts s^{-1}. Resulting exposure time after deflaring is 97 ks. Starting from the cleaned event files, we created a fluxed spectrum for each RGS detector for both observations. We did this through the SAS task rgsfluxer, considering only the first spectral order and correcting for the background.

The spectral fitting for 1H 0419-577 was performed using the package SPEX, version 2.03.02 (Kaastra et al. 1996). We first fit the RGS spectrum of each observation to check

---
[1] http://xmm.esac.esa.int/sas/8.0.0/documentation/threads/

whether the continuum was unchanged in the two datasets: we found that the continuum could be phenomenologically fitted by a broken power law in both datasets. The variations of the fitted parameters were within the statistical errors. Moreover, the measured flux in the RGS bandpass was basically the same (within $\sim 8\%$) in the two observations. This source is well known in the literature for being highly variable in the soft X-ray band (< 2.0 keV) (e.g. Pounds et al. 2004a): our observation caught it in an intermediate flux state ($F^{\mathrm{pn}}_{0.5-2.0\,\mathrm{keV}} \approx 10^{-11}$ erg s^{-1} cm^2).

Given the stability of the continuum shape in the two observations, we could safely perform a combination of the spectra to improve the signal to noise ratio. We followed the same route outlined in Kaastra et al. (2011); here we just summarize the main steps. We combined the four fluxed spectra created with rgsfluxer into a single stacked spectrum using the SPEX auxiliary program *RGS_fluxcombine*. The routine *RGS_fluxcombine* sums up two spectra using the exposure time to weigh all the bins without bad pixels. In the presence of a bad pixel, this procedure is incorrect since it would create an artificial absorption line (for an analytical example see, Kaastra et al. 2011). To correct the output spectrum from bad pixels, the task works as follows: in the presence of a bad pixel, it looks at the neighbouring pixels and, assuming that the spectral shape does not change locally, it estimates the contribution to the total flux expected from good data. Using this fraction, the task estimates the factor by which the flux at the bad pixel location has to be scaled. For the final composite spectrum, the proper SPEX readable response matrix was hence created through the tool *RGS_fmat*.

1.2.2 The OM data

We retrieved the processing pipeline subsystem (PPS) products of the OM Image Mode operations to extract the source count rates in four broadband filters: B (λ_{eff}=4340 Å), UVW1 (λ_{eff}=2910 Å), UWM2 (λ_{eff}=2310 Å), and UVW2 (λ_{eff}=2120 Å). Hence, we converted the count rates to flux densities using the conversion factors provided in the SAS watchout web page [2].

We also processed the images from the OM optical grism using the standard reduction pipeline (omgchain) provided in the SAS. The task corrects the raw OM grism files from the Modulo-8 fixed pattern noise and removes the residual scattered light features. It rotates the images, aligning the grism dispersion axis to the pixel readout columns of the images, and it runs a source detection algorithm. Finally, the tool extracts the spectra of the detected sources from the usable spectral orders. A step-by-step description of the grism extraction chain is given in the SAS User's Guide. For the present analysis, we used the 5 ks long optical spectrum (grism1, first dispersion order) from the dataset 0604720301 to measure the luminosities of the optical narrow emission lines of 1H 0419-577 (Sect. 1.4.4).

---

[2]http://xmm.esac.esa.int/sas/11.0.0/watchout/Evergreen_tips_and_tricks/uvflux.shtml

1.2.3   The EPIC data

To constrain the spectral energy distribution (SED) of the source in the X-ray band, we used the broadband EPIC-pn spectrum. We applied the standard SAS data analysis thread to the observation data files (ODF) products of both observations. We created the calibrated EPIC-pn event files, and we cleaned them from soft proton flares through a time filtering of the light curves. The counts threshold over which we discarded the time bins of the light curves was determined by a 2σ clipping of the light curve in the whole EPIC band. Starting from the clean event files we extracted the source and background spectra and we created the spectral response matrices. We fitted the EPIC-pn spectrum with a phenomenological model, considering the effect of the galactic absorption. The unabsorbed phenomenological continuum model of the EPIC-pn spectrum served as input for the X-ray SED.
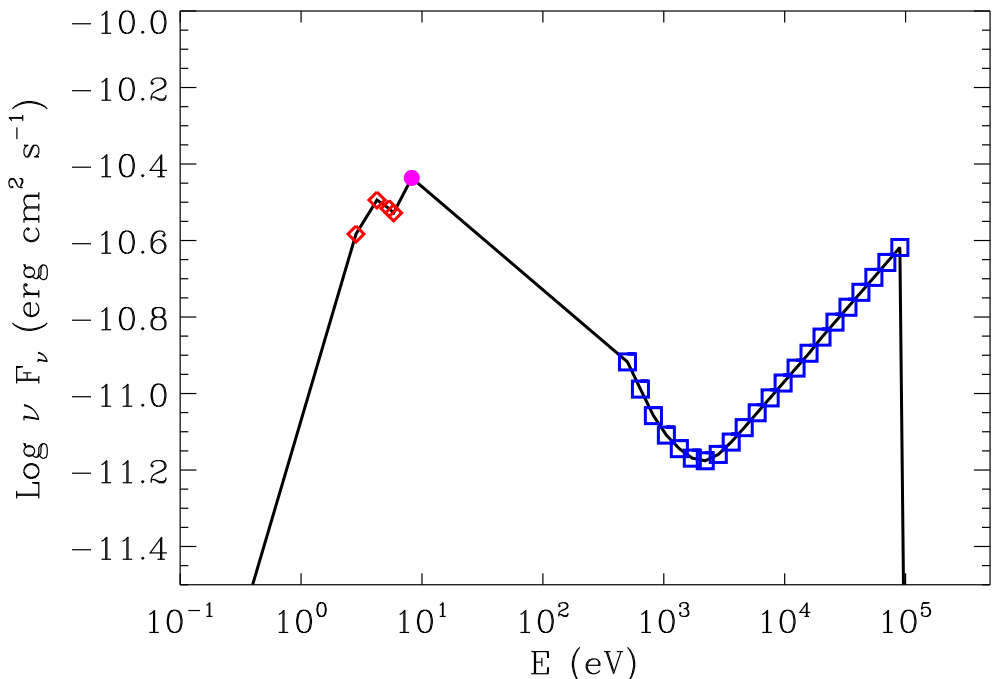
1.3   The spectral energy distribution

Figure 1.1: The spectral energy distribution for 1H 0419-577 . Open diamonds are the fluxes from the OM optical and UV broad band filters discussed in the text. The filled circle is the continuum flux taken from the simultaneous HST-COS observation. Open squares are from the unabsorbed model for the X-ray continuum, observed with the EPIC-pn.

We exploited the simultaneous XMM-*Newton* and HST-COS observation to constrain the SED of source. The shape of the SED at lower energy is constrained by the XMM-*Newton* OM and by HST, while the EPIC-pn camera covers the higher energy range. For this purpose, we estimated the UV continuum of the source at 1500 Å in the complete HST-COS spectrum. We selected a wavelength region that was not contaminated by any emission lines (1495 Å–1505 Å), and we averaged the 83 spectral points comprised in it. We cut off the SED at low ($E \leq 1.36\,\mathrm{eV}$) and high energy ($E \geq 100\,\mathrm{keV}$). Indeed, the AGN spectral energy distribution falls off with the square of the energy above 100 keV, while the optical-UV bump has an exponential cutoff in the infrared (Ferland et al. 2003). We show the SED in Fig. 3.3. From a numerical integration of the SED, we calculated the source bolometric luminosity ($\log L_{\mathrm{bol}} = 45.95\,\mathrm{erg\,s^{-1}}$): for the SMBH hosted in 1H 0419-577, the Eddington ratio is therefore $L_{\mathrm{bol}}/L_{\mathrm{Edd}} = 0.5$. The source ionizing luminosity in the 1-1000 Ry energy range is $\log L_{\mathrm{ion}} = 45.43\,\mathrm{erg\,s^{-1}}$.

1.4 Spectral analysis

1.4.1 RGS continuum fitting

We show the composite RGS spectrum of 1H 0419-577 in Fig. 1.2. We fitted the spectrum in the 8-38 Å band, and we applied a factor 5 binning. Because the (more appropriate) C-statistic cannot be computed in the case of our combined fluxed spectrum, we used the χ^2 statisticfor the fit. We checked that at least 20 counts were collected in each spectral bin, as required for using the χ^2 statistic. We consider the cosmological redshift and the effects of Galactic neutral absorption. For the latter, we used the HOT model (collisional ionized plasma) in SPEX for it, considering a column density of $N_{\mathrm{H}} = 1.26 \times 10^{20}\,\mathrm{cm^{-2}}$ (Kalberla et al. 2005) along the line of sight and a temperature of 0.5 eV to mimic a neutral gas.
We modeled the continuum emission with a broken power law. The best-fit parameters that we obtained are $\Gamma_1 = 2.73 \pm 0.02$ and $\Gamma_2 = 2.30 \pm 0.03$ as indexes with a break energy of $E_0 = 0.80 \pm 0.03\,\mathrm{keV}$.

1.4.2 RGS emission lines

Superposed on the underlying continuum, the spectrum exhibits emission lines, of which most are broadened. To model the broad emission features of the spectrum, we added a Gaussian to the fit for each candidate emission line, leaving the centroid, the line-width and the flux as free parameters. We also tested the significance of the improvement of the χ_ν^2 given by the extra component through an F-test. The F-test is trustworthy in testing the presence of an emission line if the line normalization is allowed to vary also in the negative range (Protassov et al. 2002).
We show the results in Table 1.2. Three broad components gave a highly significant improvement of the fit. Beside the Ne IX blended triplet and the O VIII Lyα line, that are redshifted respectively at ~ 15.1 Å and ~ 21.2 Å (Fig. 1.2), the most prominent broad emission feature we detected in the spectrum is a blend of the lines of the O VII triplets. In
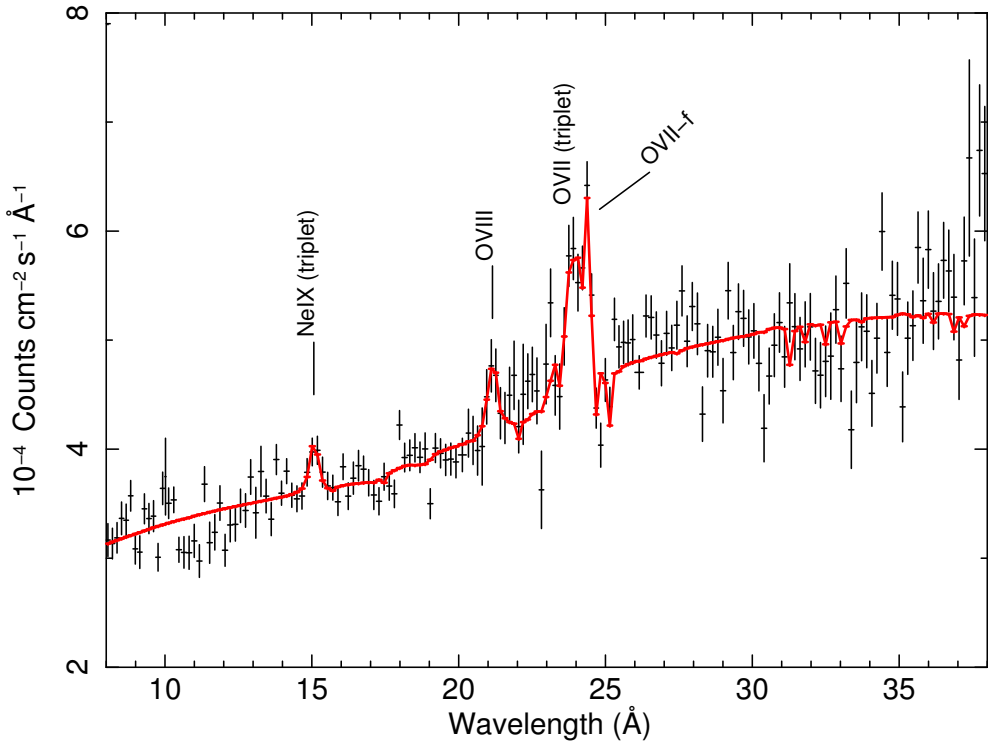
Figure 1.2: Composite RGS spectrum of 1H 0419-577. We rebinned the spectrum for clarity. The solid line corresponds to the best-fit model. The main emission features are labeled.

Fig. 1.3, we provide a zoom on the 20-26 Å spectral region, where O VII and O VIII lines are seen. To fit the spectrum in this complex region, we first modeled the prominent narrow line visible at ~ 24.4 Å with a delta function, finding a rest wavelength of 22.11 ± 0.08 Å for it. Therefore, we could identify this line as due to the forbidden transition of O VII : the line is formally detected with the F-test giving a significance above 99.99%. The line was unresolved, but we could however estimate un upper limit for its line width. Assuming a 3:1 value for the forbidden-to-intercombination line ratio (Porquet & Dubau 2000), we provided the intercombination and resonance lines that corresponds to the detected O VII-f line. After adding these two narrow lines, the spectrum was still poorly fitted in the 23.5-24.5 Å range, showing broad prominent residuals. Hence, we added a broad-line to the fit leaving the centroid free to vary in the range among the known transitions of the O VII triplets. The modeling of the oxygen emission features allows a proper detection of any intervening absorption system (e.g Costantini et al. 2007). Indeed, transitions from O IV-O VII are in principle present in the same wavelength region covered by the blend of the O VII lines.

Beside the O VII-f line, we determined upper limits for the luminosity of several other

narrow lines. Since the narrow line width is not resolved in the RGS spectrum, we modeled
them with a delta function. We estimated the upper limits by determining the maximum
normalization below which a delta line centered at the wavelength of the known transition
is undetectable over the continuum. The parameters of the X-ray narrow lines are listed
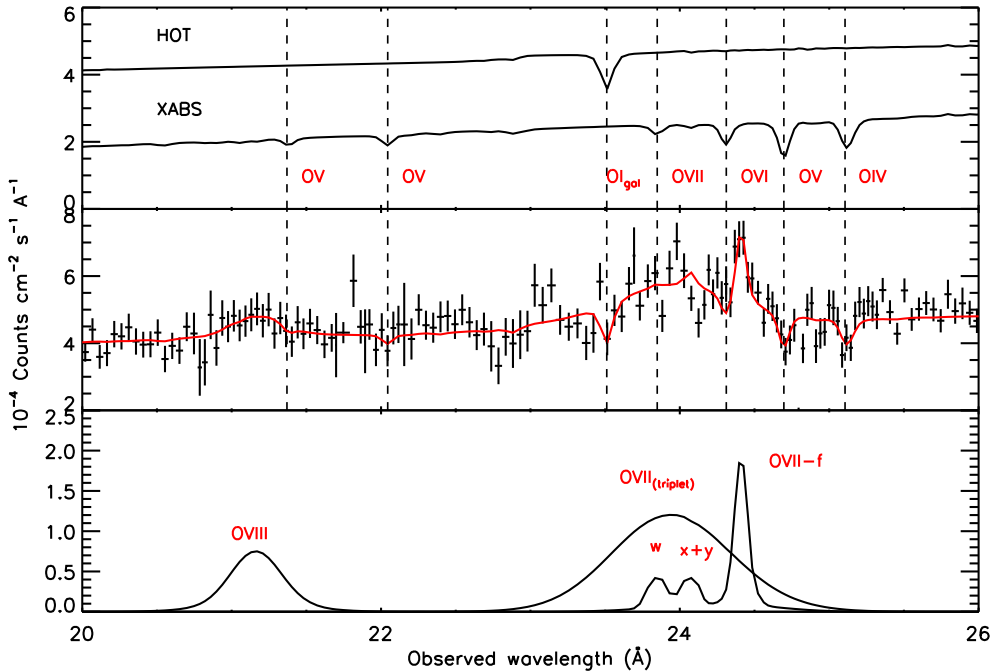in the upper panel of Table 1.4.

Figure 1.3: *Middle Panel*: Best fit to the RGS spectrum of 1H 0419-577 in the 20-26 Å wavelength
range. *Upper Panel*: Absorbing components. The neutral absorbers at z=0 and the local warm
absorber (shifted downward for plotting purpose) are displayed as solid lines. *Lower Panel*: Profiles
of the broad and narrow emission features.

Table 1.2: Parameters of 1H 0419-577 X-ray broad lines.

Ion [a]	Rest wavelength[b] Å	$\log(L_{\mathrm{obs}})$[c] erg s^{-1}	*FWHM*[d] km s^{-1}	F-test [e]
O VII	21.69 ± 0.07	42.44 ± 0.07	11000 ± 1000	$> 99.99\%$
O VIII	19.17 ± 0.06	41.95 ± 0.16	5000 ± 2000	99.2%
Ne IX	13.66 ± 0.05	41.81 ± 0.15	5000 ± 3000	99.6%

Notes. [a] Line transition. Note that O VII and Ne IX are blends. [b] Wavelength of line centroid in
the local frame. [c] Intrinsic line luminosity. [d] Line Doppler broadening as given by the full width
at half maximum of the fitted Gaussian. [e] Line significance as given by the F-test probability.

1.4.3   RGS absorption lines

We modeled the X-ray absorbing gas of 1H 0419-577 using the photoionized-absorption model XABS in SPEX. This model calculates the transmission of a slab of material, where all ionic column densities are linked through the ionization balance. Thus, it computes the whole set of absorption lines produced by a photoionized absorbing gas for a gas column density N_H and an ionization parameter ξ. The gas outflow velocity v_{out} is another free parameter. We set instead the RMS velocity broadening of the gas to the default value (100 km s^{-1}). The input ionization balance for XABS is sensitive to the spectral shape of ionizing SED: we calculated it running the tool *xabsinput* with the SED described in Sect. 1.3 as input. The *xabsinput* routine makes use internally of the Cloudy code (ver.10.00, Ferland et al. 1998) to determine the ionization balance. In the calculation, we assume solar abundances as given in Cloudy (see Cloudy manual [3] for details). We found that the absorption features of 1H 0419-577 can be fitted by a thin and lowly-ionized absorber. The best-fit parameters are $N_H = 8 \pm 3 \times 10^{19}$ cm^{-2} and $\log \xi = 0.03 \pm 0.15$. We had no strong constraints on a possible outflow velocity. We estimated an upper limit at 99% confidence ($\Delta \chi^2 = 6.67$ for one parameter) of $v_{out} \leq 210$ km s^{-1}. By adding the absorption component, we achieved an improvement of the statistic of $\Delta \chi^2 = 25$ for 3 extra degrees of freedom. According to the F-test, this χ^2 improvement is significant at a 99.7% level of confidence. The most prominent absorption lines (Fig. 1.3) are transitions from lowly ionized oxygen species, such as O IV and O V, redshifted to 25.1 Å and 24.7 Å (Fig. 1.3). respectively.In Table 1.3, we provide the column densities, predicted by XABS, of the main ions of the absorber. As a comparison, we also fitted each ionic column density individually with the SLAB model. SLAB is a simpler absorption model where all the ionic column densities are modeled independently, since they are not linked each other by any photoionization model. In the line-by-line fit with SLAB, we kept the same outflow velocity and velocity broadening of the previous XABS fit. XABS predictions and SLAB fit are consistent within the quoted errors. Therefore, we will use hereafter the value provided by XABS as reference.

1.4.4   The UV and optical narrow emission lines

We also studied the narrow emission-lines present in both the optical and the UV spectrum. In the middle panel of Table 1.4, we list the UV narrow emission lines derived from the fit performed on the simultaneous HST-COS spectrum. Each line was fitted by a combination of resolved broad and narrow components (see Sect. 3.1 and Fig. 2 in E11 for details). From the parameters of the fit, a formal 5% error was estimated on the narrow component, for both the line luminosity and line width. This error does not include any uncertainty associated to the blend of the narrow and the broad components.
Finally, the lower panel of Table 1.4 lists the optical narrow emission lines, which were obtained by fitting the OM grism spectrum (Fig. 1.4). We fitted the continuum with a broken power-law, and we modeled the sinusoidal feature that was due to a residual Modulo-8 fixed pattern noise with Gaussians. We clearly detected the broadened features

---

[3]`http://nublado.org/`

Table 1.3: Column densities of the main absorbing ions for 1H 0419-577 .

Ion	XABS [a] log(N_{ion}) cm^{-2}	SLAB [b] log(N_{ion}) cm^{-2}
O IV	16.2 ± 0.1	16.1 ± 0.2
O V	16.2 ± 0.1	16.4 ± 0.4
O VI	15.9 ± 0.1	≤ 15.6
O VII	15.2 ± 0.1	15.9 ± 0.5
C V	16.1 ± 0.1	≤ 16.8
N IV	15.3 ± 0.1	≤ 15
N V	15.3 ± 0.1	$15.4^{+0.4}_{-1.7}$
N VI	15.3 ± 0.1	≤ 15.5

Notes. [a] Ionic column densities provided by the XABS model. Quoted errors are from the propagation of the error on the fitted hydrogen column density. [b] Ionic column densities from the line-by-line fitting performed with the SLAB model.

Table 1.4: Parameters of the X-ray, UV, and optical narrow lines of 1H 0419-577 .

Ion	Wavelength [a] Å	log(L_{obs}) [b] erg s^{-1}	FWHM[c] km s^{-1}
C VI	33.73	≤ 41.67	...
N VI	29.53	≤ 40.73	...
N VII	24.78	≤ 40.65	...
O VII-f	22.11 ± 0.08	41.84 ± 0.08	≤ 2500
O VIII	18.97	≤ 41.69	...
Ne IX	13.70	≤ 40.52	...
C IV	1551	42.89	805 ± 40
C IV	1548	43.03	805 ± 40
Ly α	1215	43.18	488 ± 24
O VI	1038	42.69	840 ± 42
O VI	1032	42.73	840 ± 42
[O III]	5007	43.13 ± 0.01	1200 ± 100
[O III]	4959	42.71 ± 0.03	500 ± 300
Hβ	4861	42.14 ± 0.12	488 (fixed)

Notes. Parameters and errors for the X-ray, UV, and optical narrow emission lines of 1H 0419-577 . [a] Wavelength of the transition in the rest frame. [b] Intrinsic line luminosity. [c] Doppler broadening of the line, as given by the full width at half maximum of the fitted Gaussian. Note that the X-ray lines are not resolved in the RGS spectrum.

of the hydrogen Balmer series (Hβ λ4861 Å, Hγ λ4341 Å, Hδ λ4102 Å and Hϵ λ3970 Å) and the narrow emission lines of the [O III] doublets $\lambda\lambda$5007,4959 Å. In the analysis, we used
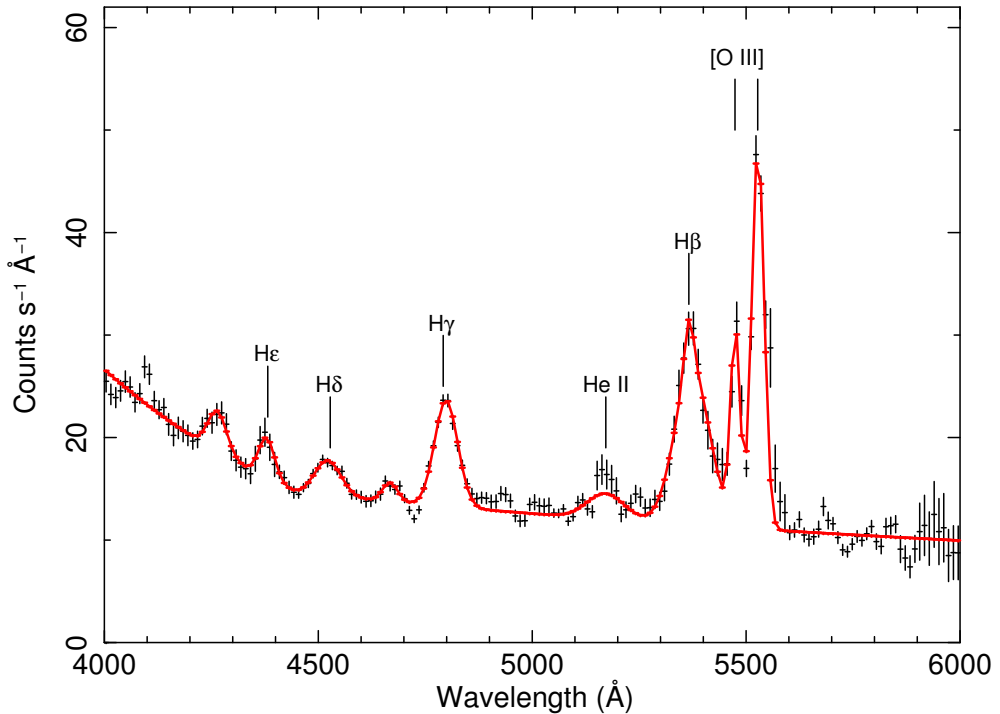
Figure 1.4: OM optical grism spectrum of 1H 0419-577 in the 4000-6000 Å range. The best-fit model is displayed by a solid line. The main emission features from the hydrogen Balmer series an the [O III] doublet are labeled.

the luminosities of the [O III] lines and of the narrow component of Hβ. We modeled the [O III] lines with Gaussian profiles, leaving the centroid, the line width, and the flux as free parameters. The full width at half maximum (*FWHM*) of the [O III] lines was resolved, and it is reported in Table 1.4. In fitting the Hβ line, we used two Gaussians, respectively, for a narrow and a broad component. We set the wavelength of the narrow component to the nominal wavelength of the Hβ transition and its width to that of the Lyα narrow component measured in the UV, leaving only the normalization as free parameters. All the parameters of the broad component were otherwise left free. The fitted *FWHM* for the broad Hβ component (4700 ± 400 km s^{-1}) is within the range of the three broad components of Lyα measured in the UV spectrum (≈ 1000, 3400, and $14\,000$ km s^{-1}).

1.5   Photoionization modeling

To estimate the global properties of the gas that emits the narrow lines in 1H 0419-577, we used the photoionization code, Cloudy v. 10.0 (Ferland et al. 1998). In the calculation, we assumed total coverage of the source and a gas density of 10^8 cm^{-3}. We note that the

Table 1.5: Covering factor, column density and ionization parameter for the gas emitting the UV and X-ray narrow lines in 1H 0419-577 .

	C_v	$\log N_{\mathrm{H}}$ cm^{-2}	$\log \xi$
UV [a]	0.104 ± 0.006	21.67 ± 0.25	0.48 ± 0.15
X [b]	0.104 (fixed)	21.40 ± 0.25	1.44 ± 0.15

Notes. [a] Best-fit parameters for the gas emitting the UV lines. [b] Parameter of the gas model consistent with the observed upper limits and best-fit of the only detected X-ray line. We imposed the same gas covering factor of the UV-emitter. See text for details.

assumption on the gas density is not critical for the resulting gas parameters. Indeed, line ratios of He-like ions are not sensitive to the gas density over a wide range of density values (Porquet & Dubau 2000). We used the SED described in Sect. 1.3 and the ionizing luminosity derived from it as input. We created a grid of line luminosities for a wide range of possible gas parameters: the column density ranged between $\log N_{\mathrm{H}} = [19-23]\,\mathrm{cm}^{-2}$ and the ionization parameter between $\log \xi = [-0.3-2.7]\,\mathrm{erg\,cm\,s}^{-1}$ with a spacing of 0.25 dex and 0.15 dex, respectively. In the fitting routine, we first computed the gas covering factor C_v for each grid entry by imposing to the model to match the luminosity of the Lyα line. Hence, we modeled the data by minimizing the merit function:

$$\chi^2 = \sum \frac{(C_v L_c - L_{\mathrm{obs}})^2}{\sigma_{\mathrm{obs}}^2},$$

where L_c is the model-predicted luminosity of each line, C_v is the gas covering factor, and L_{obs} is the observed line luminosity with statistical error σ_{obs}. We fitted all the UV, X-ray, and optical luminosities listed in Table 1.4. The C IV, O VI, and [O III] doublets were considered as a blend, and 3σ upper limits for the X-ray lines of Table 1.4 were also included.

A model with a $\sim 10\%$ covering factor, $\log N_{\mathrm{H}} \sim 21.67$ cm^{-2} and $\log \xi \sim 0.48$ fits the three UV data points (Lyα, C IV, O VI) and agrees with all the upper limits for the X-ray luminosities. In fitting the UV lines we obtain a minimum $\chi^2/\mathrm{d.o.f} = 0.35/1$. With just one degree of freedom the probability of getting a low or lower observed χ^2 for a correct model is 0.45.The derived parameter for the UV emitter are outlined in Table 1.5. We report the width of the grid step as error on the parameters. The error for the covering factor is estimated by propagating the error ($\sim 5\%$) on the luminosity of the Lyα line.

This best-fit model neither matches the luminosity of the O VII-f nor the luminosities of the optical lines, suggesting that X-ray and optical lines arise in a gas with different physical conditions. It was not possible to estimate the parameters of the X-ray emitter through a proper fit, because we had only one line detection. However, the measured upper limits provide useful constraints for the model. Assuming the same covering factor of the UV emitter, we selected all the models in the grid that agree with the measured upper limits and match the luminosity of the O VII-f line within $3\sigma_{\mathrm{obs}}$. In this calculation, we added the contribution of the best-fit UV model to the X-ray luminosities. We find that the selected

models have log $N_{\rm H}$ ([21.13−21.93] cm^{-2}) and their ionization parameter is comprised within log ξ = [1.12−2.06]. Therefore, the fit that best models the O VII-f line has a column density consistent within a grid step with the UV emitter one (log $N_{\rm H}$ ≈21.40 cm^{-2}) but its ionization parameter is (log ξ ≈1.44). This may indicate a geometrical connection between the UV and the X-ray emitter. In the case when also the gas covering factor is left free, we obtained a broader parameter range, (C_ν = [0.03−0.60], log $N_{\rm H}$ = [20.90−23.00] cm^{-2}), which still indicates a higher ionization parameter (log ξ = [1.12−1.60]) with respect to the UV-emitter. We also remark that none of the models in our grid match the optical-lines luminosities. Finally, we note that models with parameters consistent with the warm absorber detected in the RGS spectrum neither fit the UV (χ^2 = [246−631]) nor the X-ray (the O VII-f is not fitted within ≈ 6σ) emission lines. We show the best-fit models for the UV and the X-ray emission lines in Fig. 1.5. The derived parameter for the X-ray emitter are outlined in the second row of Table 1.5.

1.6 Comparison between the UV and the X-ray absorber

We investigate the possible relationship between the UV absorber found for 1H 0419-577 in E11 and the X-ray absorber found here (Sect. 1.4.3) by comparing the gas parameters independently measured in the two different wavebands.

Three different outflow components (v_1 = −38 km s^{-1}, v_2 = −156 km s^{-1}, and v_3 = −220 km s^{-1}) were identified in the UV. Because of the the lower RGS resolution, we were not able to resolve any of the UV components; however our upper limit for the outflow velocity of the X-ray absorber is consistent with all of them. Thus, it is likely that we observed a blended superposition of the UV components in the X-rays.

In Table 1.6, we compared the UV and X-ray column densities for C II, C IV, N V, and O VI. Absorption lines from O VI were detected in both bands, while lines from C II, C IV, and N V were detected only in the UV; their column densities however could be predicted by our XABS model. We report the sum of the column densities of the UV kinetic components 1, 2, and 3, in Table 1.6. These were obtained using a UV partial covering model, with a power law distribution of the optical depth (see E11 for details). The column densities independently found in the X-ray and the UV agree within the quoted error range for all ions.

The ionization parameter of the UV absorber is given in terms of $U_H = \frac{Q_H}{4\pi R^2 c\, N_{\rm H}}$ (where Q_H is the rate of ionizing photons emitted by the source, R is the absorber distance from the source, c is the speed of light, and $N_{\rm H}$ is the total hydrogen column density), while we used ξ as defined in Sect. 1.1. For the SED of 1H 0419-577, log ξ = 1.7 + log U_H. In the UV, the determination of U_H is not well constrained: for a broken power law SED and for a gas with solar abundances, log U_H =[-1.7 to -1.5] (Fig. 8 in E11). Applying the conversion factor just given, this value corresponds to log ξ =[0 to 0.2], which is consistent with the more constrained value found here for the X-ray absorber: log ξ =[-0.12 to 0.18].
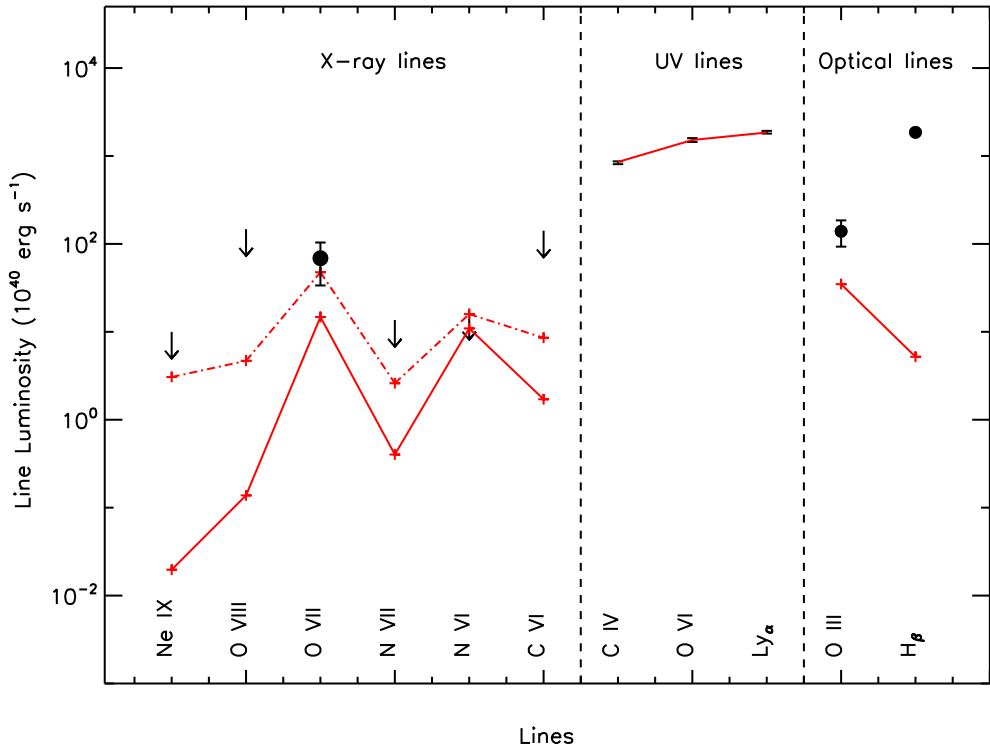
Figure 1.5: Best fit of the intrinsic luminosities of the UV narrow emission lines (*middle panel*). The model is displayed by a solid line only to guide the eye. The line luminosities predicted by the model in the X-ray (*left panel*) and in the optical (*right panel*) band are displayed by red crosses connected by a solid line. The model agrees with the upper limits for the X-ray lines but does not fit the optical lines. The qualitative best fit model for the X-ray lines is also shown by red crosses connected by a dot dashed line. Error bars, when larger than the size of the plotting symbols, are also shown. Note that a 3σ error bar is shown for O VII-f line.

1.7   Discussion

1.7.1   Absorber distance and energetics

The spectral analysis of the RGS spectrum of 1H0419-577, together with the analysis of the simultaneous COS spectrum (E11), revealed that the X-ray and the UV emission spectra of 1H 0419-577 are both absorbed by a thin, weakly ionized absorber. As pointed out in Sect. 1.6 the ionization parameter and the ionic column densities independently measured in the UV and the X-ray agree with each other. Thus, it is likely that the UV and X-ray warm absorber are the same gas. In the UV, the kinetic structure of the warm absorber is resolved, with three outflowing components detected. The bulk of absorbing column density is carried by components 2+3 (see Table 1 and 2 and Fig. 3 in E11). Therefore, we

Table 1.6: Comparison between the UV and X-ray column densities of the absorbing ions in 1H 0419-577 .

Ion	UV [a] $\log(N_{ion})$ cm^{-2}	X [b] $\log(N_{ion})$ cm^{-2}
C II	12.99 − 13.08	13.11
C IV	15.16 − 15.29	15.42
N V	15.16 − 15.31	15.36
O VI	15.83 − 15.96	15.89

Notes. [a] Ionic column densities measured in the UV. We considered the sum of the three kinetic components detected. [b] Ionic column densities predicted the X-ray model (XABS), as discussed in Sect.1.4.3.

likely detected a blend of the UV kinetic components dominated by the UV components 2+3 in the lower resolution X-ray spectrum. Having established the connection between the UV and the X-ray absorber, we can exploit the complementary information derived in the two wavebands to estimate the warm absorber location and energetics.

In the following discussion, we consider that an ionized medium, parameterized by $\log \xi \approx 0.03$ and $N_{H} \approx 8 \times 10^{19}$ cm^{-2} (this paper), is outflowing from the source at the velocity of UV component 3 ($v_3 = -220$ km s^{-1}). Additionally, we use a gas number density $n_{H} \leq 25$ cm^{-3}, as estimated in E11 for the UV component 2+3. This upper limit for the gas number density was derived from the ratio of the (nondetected) first excited metastable and the ground level of C II. As already pointed out in Sect. 1.6, the C II column density measured in the UV is well accounted for by our absorber model. We note however that the C II 1334.5 Å profile is possibly asymmetric in the COS spectrum, and the centroid is slightly shifted with respect to the UV component 3: at least part of the C II emission may in principle arise in a kinetic component that is separated from the UV component 3. However, this possible additional component is not evident in any other lines.

Given the X-ray/UV connection just established, the following discussion is based on the assumption that the upper limit for the gas density estimated in the UV may be applied to the UV/X-ray absorber. We assume a thin shell geometry for the outflow. In this approximation, the outflow is spherically shaped with a global covering factor of the line of sight C_g. Each outflowing shell, Δr thick, is partially filled with gas, with a volume filling factor f. The volume filling factor f can be estimated analytically (Blustin et al. 2005) from the condition that the kinetic momentum of the outflow must be on the order of the momentum of the absorbed radiation plus the momentum of the scattered radiation. Applying this condition, we found that the absorber in 1H 0419-577 has a volume filling factor $f \approx 3 \times 10^{-3}$, suggesting that it may consist of filaments or fragments that are very diluted in the available volume and intercepting our line of sight.

Exploiting the tighter constraint on the ionization parameter provided by the present

analysis we confirm the distance estimation given in E11:

$$R \geq (\frac{L_{\text{ion}}}{n_{\text{H}}\xi})^{1/2} \gtrsim 3\,\text{kpc}. \tag{1.1}$$

This estimation places the warm absorber at the host galaxy scale, well outside the central broad-line region ($R_{\text{BLR}} \approx 0.07\,\text{pc}$, Turner et al. 2009). UV absorbers located at a galactic-scale distance are not uncommon in low-redshift quasars (see Table 6 in E11 and references therein). The X-ray/UV connection that we infer for this source would therefore make its low-ξ absorber the first galactic scale X-ray absorber ever detected. A possible confining medium for an X-ray absorbers located at about a ~kpc from the nucleus could be a radio jet-like emission. This source is radio quiet, but a 843 MHz flux detection (Mauch et al. 2003) may be due to a weak radio lobe. More accurate radio measurements are required to test this possibility. This a galactic-scale wind may be both AGN or starburst driven. However, the UV analysis for this source, suggests that the photoionization of the outflow may be dominated by the AGN emission (see discussion in E11 and references therein). We also estimated an upper limit for the WA distance from the condition that the thickness Δr of the outflowing-gas column should not overcome its distance R from the center (Blustin et al. 2005). Analytically, this condition is

$$\frac{\Delta r}{R} \approx \frac{N_{\text{H}}}{f\, n_H R} = \frac{\xi R\, N_{\text{H}}}{L_{\text{ion}}f} \leq 1. \tag{1.2}$$

From Eq. 1.2, we derived: $R \lesssim 15\,\text{kpc}$. We note that this distance is well within the typical extension of a galactic halo (e.g., as mapped by H I emission for a large sample, de Blok et al. 2008). Therefore, we use this estimation in the following to derive hard upper limits for the mass outflow rate and kinetic luminosity.

The outflow mass rate is given by

$$\dot{M}_{\text{out}} = 4\pi\mu m_P R\, v\, N_{\text{H}}\, C_g = [4-16]\, M_{\odot}\, \text{yr}^{-1}, \tag{1.3}$$

where μ=1.4 is the mean atomic mass per proton and m_P is the proton mass. We assumed a covering factor C_g=0.5, given by the fact that outflows are seen in about 50% of the observed Seyfert galaxies (Dunn et al. 2007).

This value may be compared with the classical mass accretion rate of a black hole in the Eddington regime ($\dot{M}_{\text{Edd}} = L_{\text{bol}}/\eta c^2$) to obtain an estimation of the impact of the mass loss due to the outflow on the AGN. Assuming a typical accretion efficiency $\eta = 0.1$ and taking $L_{\text{bol}} = 9 \times 10^{45}\,\text{erg s}^{-1}$, as estimated from the SED (see Sect. 1.3), we obtained

$$\dot{M}_{\text{Edd}} \approx 2 M_{\odot}\, \text{yr}^{-1}. \tag{1.4}$$

As found in most cases (see Costantini 2010), the mass outflow rate can be of on the same order of the mass accretion rate, suggesting a balance between accretion and ejection in this system. The kinetic luminosity of the outflow is

$$L_{\text{kin}} = \frac{\dot{M}_{\text{out}} v^2}{2} \approx 10^{40.7-41.4}\,\text{erg s}^{-1}, \tag{1.5}$$

and it represents a low fraction ($\lesssim 10^{-2}\%$) of the AGN bolometric luminosity L_{bol}. Thus, the outflow is not energetically significant in the AGN feedback scenario, where kinetic luminosities of a few percent of the bolometric luminosities are required (Scannapieco & Oh 2004). We finally estimated the maximum kinetic energy that the outflow can release into the interstellar medium in the case that it is steady all over the AGN life time ($\sim 4 \times 10^8$ yr, Ebrero et al. 2009):

$$E_{tot} \approx 10^{56.8-57.5} \text{ erg.} \tag{1.6}$$

As argued in Krongold et al. (2010), this value may in principle be sufficient to evaporate the interstellar environment out of the host galaxy. However, it is not trivial to couple this energy effectively to the galaxy (e.g. King 2010).

1.7.2 The origin of the emission lines

The simultaneous HST-COS and XMM-*Newton* observation of 1H 0419-577 provided a set of narrow lines, ranging from the optical to the X-ray domain, suitable for photoionization modeling. We show that a single gas model cannot account simultaneously for all the narrow line emission. The UV lines are emitted by moderately ionized gas, intercepting about the 10% of the total AGN radiation field. This value for the covering factor is consistent with what previously was reported (C_v=1.9%–20.5%, Baskin & Laor 2005). The X-ray lines are instead emitted in a more highly ionized gas phase: ($\log \xi \approx 1.44$). We also found that a gas with the same column density and covering factor as the UV emitter is a good description of the X-ray emission. This may suggest that the two emitters are two adjacent layers of the same gas.

Most of the optical emission is not accounted for by our model: it can explain only up to 4% of the Hβ luminosity and 0.3% of [O III] luminosity. Lower densities are required to emit the [O III] lines: the [O III] λ5007Å line is indeed collisionally de-excited for $n_H \gtrsim 10^5 \text{ cm}^{-3}$ (Osterbrock 1989). Our simple photoionization model cannot however account for the variety of gas physical conditions occurring in the narrow-line region. Our analysis suggests that the NLR is a stratified environment hosting a range of different gas components. Previous studies have shown that multicomponent photoionization models are required for describing the narrow emission lines spectrum of AGN. The narrow line emission from the infrared to the UV is well reproduced assuming that the emitting region consists of clouds with a wide range of gas densities and ionization parameters (Ferguson et al. 1997). In the case of NGC 4151, more than one gas component, with different covering factor, is required to explain line emission even limiting the analysis to the soft X-ray regime (Armentrout et al. 2007). In the present case, the data quality did not allow us to test a more complex, multicomponent scenario.

The estimated gas parameters of the warm absorber are largely inconsistent with the emitters. Thus, neither the UV nor the X-ray emitter can be regarded as the emission counterpart of the warm absorber. Therefore, a connection between the warm absorber and the gas in the NLR is discarded in the present case.

1.7.3   The geometry of the gas

The present analysis of the UV and X-ray spectrum of 1H 0419-577 revealed three distinct gas phases: the UV/X-ray warm absorber, the X-ray emitter ($\log \xi_X \approx 1.44$), and the UV emitter ($\log \xi_{UV} \approx 0.48$). We used the line width of Table 1.4 to estimate qualitatively the location of the emitters. Assuming that the NLR gas is moving in random keplerian orbits with an isotropic velocity distribution, the velocity v_{FWHM} by which the narrow lines are broadened is given by (Netzer 1990):

$$v_{FWHM} = \sqrt{\frac{4GM}{3R}}, \tag{1.7}$$

where M is the mass of the SMBH and R is the radial distance from it. The *FWHM* of the UV lines ([488–805] km s^{-1}, Table 1.4) therefore give the approximate location of the UV emitter:

$$R_{UV}^{em} \approx [1-3]\,\text{pc}. \tag{1.8}$$

This distance would imply a gas number density of $n_H = (L_{ion} \xi_{UV})/(R_{UV}^{em})^2 \approx 10^{7-8}\,\text{cm}^{-3}$ at the location of the UV emitter, which is consistent with the range of gas density and distance where these lines are optimally emitted (Ferguson et al. 1997). The X-ray emitter is consistent to be a gas with covering factor and column density similar to the UV emitter. This suggests that it may be a layer of gas adjacent to UV emitter. The higher X-ray ionization parameter may by both produced by a smaller distance to the SMBH and a lower gas density. The gas density in the NLR ionization cone has a smoothly decreasing radial profile (Bianchi et al. 2006). Therefore, a similar gas density for both the emitters can be assumed if the UV and X-ray emitter are not radially detached, as we suggested. From the definition of ionization parameter, it follows that

$$R_X^{em} \approx \sqrt{\frac{\xi_{UV}}{\xi_X}}\, R_{UV}^{em} \approx [0.3-1.0]\,\text{pc}.$$

This estimation is consistent with the lower limit for the distance ($R_X^{em} \gtrsim 0.1\,\text{pc}$) that is implied by the upper limit for the broadening of the O VII-f line. This first order estimation places the emitters on a very different distance scale compared to the absorber, again arguing against a connection between emission and absorption in this source. We did not detect the NLR in absorption: this may indicate that the NLR ionization cone is not along our line of sight, as this would produce visible O VII absorption lines. We are possibly detecting scattered light from the NLR. The presence of a circumnuclear scattering region has been proposed, such as for the case of NGC 4151 (Kraemer et al. 2001).

1.8   Summary and conclusions

We analyzed and modeled the X-ray, UV, and optical data of the Seyfert 1.5 galaxy 1H 0419-577. Simultaneous X-ray (RGS) and UV (HST-COS) spectra of the source were taken to study the

absorbing-emitting photoionized gas in this source. Optical data from the OM were also used for the present analysis. We found three distinct gas phases with different ionization. The X-ray and the UV spectrum are both absorbed by the same, lowly ionized warm absorber ($\log \xi = 0.03 \pm 0.15$). The outflow is likely to be located in the host galaxy at a distance $R \gtrsim 4\,\mathrm{kpc}$ from the central source. The kinetic luminosity of the outflow is a low fraction ($\lesssim 10^{-2}\%$) of the AGN bolometric luminosity, making the outflow unimportant for the AGN feedback. However, this galactic-scale X-ray absorber, like the one we serendipitously discovered in this source, might still play a role in the host galaxy evolution.

We performed photoionization modeling of the narrow lines emitter using the available UV, X-ray, and optical narrow emission lines. The analysis indicates that the narrow line emitters are not the emission counterpart of the WA. A connection between the WA and the NLR can therefore be discarded in this case.

The X-ray emission lines are emitted in a more highly ionized gas phase compared to the one producing the UV lines. We suggest a geometrical connection between the UV and the X-ray emitter, where the emission takes place in a single gas layer, that is located at about a $\sim$ pc scale distance from the center. In this scenario, the X-ray lines are emitted in a portion of the layer located closer to the SMBH.

Finally, our analysis suggests that the NLR is a stratified environment, hosting a range of gas phases with different ionization and density.

ACKNOWLEDGEMENTS

2 —— Simultaneous XMM-*Newton* and HST-COS observation of 1H 0419-577: Broadband spectral modeling of a variable Seyfert galaxy

Published in:

L. Di Gesu, E. Costantini, E. Piconcelli,
J. Ebrero, M.Mehdipour, J.S. Kaastra,
Astronomy & Astrophysics, volume 563, A95, 2014.

·· **Abstract** ··

In this paper, we present the longest exposed (97 ks) XMM-Newton EPIC-pn spectrum ever obtained for the Seyfert 1.5 galaxy 1H 0419-577. With the aim of explaining the broadband emission of this source, we took advantage of the simultaneous coverage in the optical/UV that was provided in the present case by the XMM-Newton Optical Monitor and by a HST-COS observation. Archival FUSE flux measurements in the FUV were also used for the present analysis. We successfully modeled the X-ray spectrum and the optical/UV fluxes data points using a Comptonization model. We found that a blackbody temperature of $T \sim 56$ eV accounts for the optical/UV emission originating in the accretion disk. This temperature serves as input for the Comptonized components that model the X-ray continuum. Both a warm ($T_{wc} \sim 0.7$ keV, $\tau_{wc} \sim 7$) and a hot corona ($T_{hc} \sim 160$ keV, $\tau_{hc} \sim 0.5$) intervene to upscatter the disk photons to X-ray wavelengths. With the addition of a partially covering ($C_v \sim 50\%$) cold absorber with a variable opacity ($N_H \sim [10^{19} - 10^{22}]$ cm^{-2}), this model can explain also the historical spectral variability of this source with the present dataset presenting the lowest one ($N_H \sim 10^{19}$ cm^{-2}). We discuss a scenario where the variable absorber becomes less opaque in the highest flux states because it gets ionized in response to the variations of the X-ray continuum. The lower limit for the absorber density derived in this scenario is typical for the broad line region clouds. We infer that 1H 0419-577 may be viewed from an intermediate inclination angle $i \geq 54°$, and, on this basis, we speculate that the X-ray obscuration may be associated with the innermost dust-free region of the obscuring torus. Finally, we critically compare this scenario with all the different models (e.g., disk reflection) that have been used in the past to explain the variability of this source.

··

2.1   Introduction

The infalling of matter onto a supermassive black hole (SMBH) supplies the energy that active galactic nuclei (AGN) emit in the form of observable radiation over a broad energy range. In the radio quiet case, the AGN emission mostly ranges from optical to X-ray wavelengths. The optical/UV emission is thought to be direct thermal emission from the accreting matter. A standard geometrically thin, optically thick accretion disk (Shakura 1973, Novikov & Thorne 1973) produces a multicolor blackbody spectrum, whose effective temperature scales with the black hole mass as $\propto M^{-1/4}$. Therefore, for a typical AGN hosting a supermassive black hole (SMBH) of $M \sim 10^8 M_\odot$, the disk spectrum is expected to peak in the far UV range (e.g., for an Eddington ratio of $L/L_{\mathrm{Edd}} \sim 0.2$, $T \sim 20\,\mathrm{eV}$).

The Wien tail of the accretion disk emission is not expected to be strong in the soft X-rays. However, Seyfert X-ray spectra display a prominent "soft excess" (Arnaud et al. 1985, Piro et al. 1997) that lies well above the steep power law, which well describes the spectrum at energies larger than ~ 2.0 keV (Perola et al. 2002, Cappi et al. 2006, Panessa et al. 2008). The origin of the soft X-ray emission in AGN has been debated a lot in the last decades. Comptonization of the disk photons in a warm plasma is a possible mechanism to extend the disk emission to higher energies (Magdziarz et al. 1998, Done et al. 2012). Alternatively, relativistically blurred reflection of the primary X-ray power law in an ionized disk (Ballantyne et al. 2001, Ross & Fabian 2005) is another possible explanation. Partial covering ionized absorption (see Turner et al. 2009, for a review) is also able to explain the soft X-ray emission without requiring extremely relativistic conditions in the vicinity of the black hole. Discriminating among these models through X-ray spectral fitting alone is difficult, even in high signal to noise spectra. In many cases, models with drastically different underlying physical assumptions can provide an acceptable fit (e.g., Middleton et al. 2007, Crummy et al. 2006). For instance, in the case of the well-known nearby Seyfert 1 MCG-6-30-15, both a reflection model (Ballantyne et al. 2003) and an absorption based model (Miller et al. 2008) have been successfully used to fit the spectrum. For these reasons, the nature of the soft excess is still an open issue (see also Piconcelli et al. 2005). Recently, the multiwavelength monitoring campaign (spanning over ~ 100 days) of the bright Seyfert galaxy Mrk 509 (Kaastra et al. 2011) provided possible discriminating evidence. During the campaign, the soft excess component varied with the UV continuum emission (Mehdipour et al. 2011, hereafter M11). This finding disfavors disk reflection, at least as the main driver of the source variability on the few days timescale which was typical of the campaign. Indeed, in the case of disk reflection the soft excess component should vary in correlation with the hard ($\gtrsim 10$ keV) X-ray flux because of the broad reflection bump at ~ 30 keV that characterizes any reflection component. The M11 result is not a unique case: in a different case, the soft excess variability has been found to be independent from the hard X-ray variability also on a longer ($\sim$ years) timescale (e.g., Mrk 590, Rivers et al. 2012).

The correlation between the soft X-ray and UV variability may be a natural consequence of Comptonization, because the soft X-ray emission is directly fed by the disk photons in this framework. Indeed, this interpretation explains the simultaneous broadband optical/UV/X-ray/gamma-ray spectrum of Mrk 509 obtained in the monitoring campaign
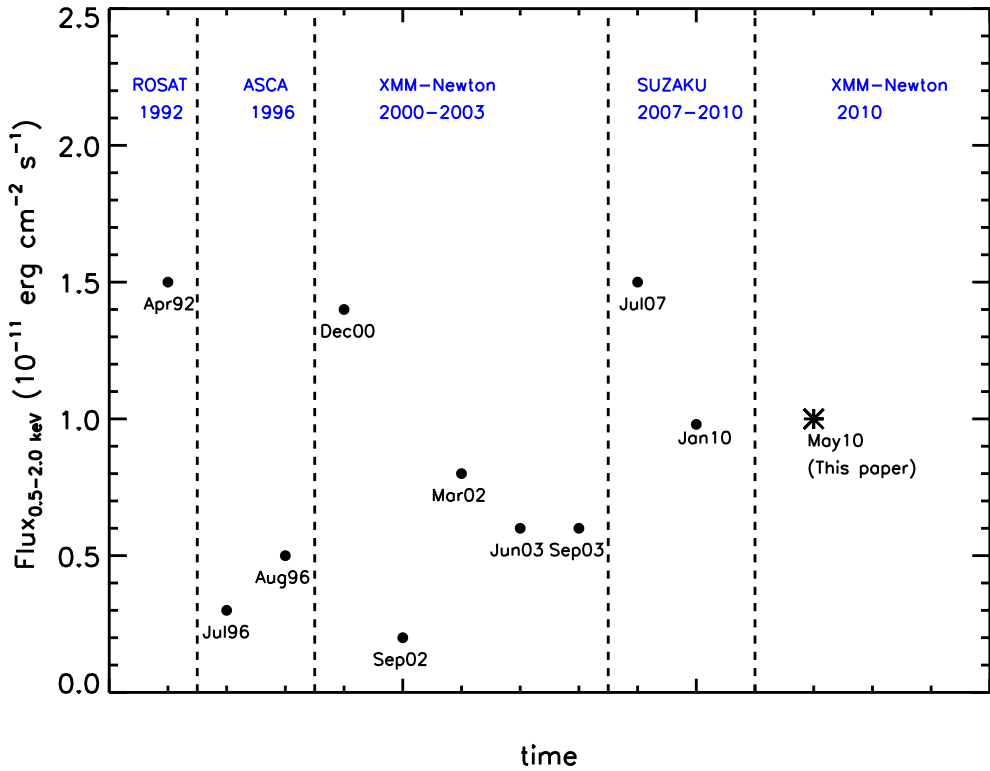
Figure 2.1: Historical X-ray (0.5–2.0 keV) fluxes of 1H 0419-577. Each symbol indicates a flux measurement, as obtained in the labeled date.

(Petrucci et al. 2013, hereafter P13).

In the P13 broadband model, two Comptonized components model, respectively, the "soft-excess" and the X-ray emission above ~ 2.0 keV. Indeed, it is commonly accepted that the phenomenological power law that characterizes AGN spectra above ~ 2.0 keV is produced by Comptonization of the disk photons in a hot (T~ 100 keV), optically thin corona (Haardt & Maraschi 1991). The nature and the origin of the hot corona are still largely unknown. However, recent results from X-ray timing techniques (e.g., X-ray reverberation lag, Wilkins & Fabian 2013) or imaging of gravitationally lensed quasar (e.g., Morgan et al. 2008) indicates that it may be a compact emitting spot which is located a few gravitational radii above the accretion disk (e.g., Reis & Miller 2013).

Table 2.1: XMM-*Newton* datasets log.

Obs	Observation ID	Date	Orbit	Net exposure [a]	$F_{0.5-2.0\,keV}$ [b]	$F_{2.0-10.0\,keV}$ [b]
				ks	$10^{-12}\,\mathrm{erg\,s^{-1}\,cm^2}$	$10^{-12}\,\mathrm{erg\,s^{-1}\,cm^2}$
1[c]	0112600401	04/12/2000	181	6	14	16
2[c]	0148000201	25/09/2002	512	11	1.8	8.2
3[c]	0148000401	30/03/2003	605	11	7.6	11.3
4[c]	0148000501	25/06/2003	649	6	6.4	10.3
5[c]	0148000601	16/09/2003	690	11	5.6	10.0
6[d]	0604720301/401	28-30/05/2010	1917/1918	97	10	14

Notes. [a] Net exposure time after flaring filtering. [b] Observed fluxes in the quoted bands [c] Archival datasets. [d] Datasets analyzed in this paper.

2.2 1H 0419-577: A variable Seyfert galaxy

The Seyfert 1.5 (Véron-Cetty & Véron 2006) galaxy 1H 0419-577 is a radio quiet quasar located at redshift z=0.104. The estimated mass for the SMBH harbored in its nucleus is $\sim 3.8 \times 10^8 M_\odot$ (O'Neill et al. 2005). The source has been targeted by all the major X-ray observatories, and, in Fig. 2.1 we plot the historical fluxes in the 0.5–2.0 keV band. As noticed for the first time in Guainazzi et al. (1998), 1H 0419-577 undergoes frequent transitions between low and high flux states. While the bulk of the flux variation occurs in the soft X-ray, the spectral slope flattens out drastically in the hard (2–10 keV) X-ray band (down to $\Gamma = 1.0$ in the lowest state, Page et al. 2012, Pounds et al. 2004a). Due to this peculiar behavior in the X-rays, 1H 0419-577 is challenging for any interpretation, and for this reason, it has been subject of discussion over the past years.

According to Page et al. (2002), the cooling of the plasma temperature in the hot corona may produce the observed flux/spectral transition. Afterwards, Pounds et al. (2004a,b) carried on a systematic study of the spectral variability in this source, using five ~15 ks long observations, which had been taken during one year with a time spacing of ~3 months. These authors concluded that the spectral variability is dominated by an emerging/disappearing steep power-law component, which is, in turn, modified by a slightly ionized variable absorber. The fitted absorber becomes more ionized and less opaque as the continuum flux increases, supporting the idea that a fraction of the soft X-ray emission may be due to re-emission of the absorbed continuum in an extended region of photoionized gas. An alternative explanation of the same XMM-*Newton* datasets was, however, readily proposed in the framework of blurred reflection model (Fabian et al. 2005, hereafter F05). This model prescribes that AGN spectral variability is due to the degree of light-bending, as the primary power-law emitting spot moves in a region of stronger gravity. Low flat states, such as the ones observed in 1H 0419-577, are extreme reflection-dominated cases occurring when the primary emission is almost completely

focused down to the disk and do not reach the observer. The broader spectral coverage provided by two subsequent *Suzaku* observations of 1H 0419-577 did not break this models degeneracy. The variable excess observed above ∼15 keV can be either explained by reflection (Walton et al. 2010, Pal & Dewangan 2013) or by reprocessing of the primary emission in a partially covering Compton-thick, screen of gas (Turner et al. 2009). The high ionization parameter suggests that this absorber may be part of a clumpy disk wind located within the broad line region (BLR).

In this paper, we present the longest exposure EPIC-pn dataset of 1H0419-577 that has been obtained so far. The XMM-*Newton* observation was taken simultaneously to a HST-COS observation in the UV (Edmonds et al. 2011) and caught the source in an intermediate flux state (Fig. 2.1). In the Reflection Grating Spectrometer (RGS) spectrum of this dataset (already presented in Di Gesu et al. 2013, hereafter Paper I) we detected a lowly ionized absorbing gas (also observed in *Suzaku*, Winter et al. 2012). We found that the X-ray and the UV absorbing gas (Edmonds et al. 2011) are consistent to be one and the same. The low-gas density estimated in the UV and the low ionization parameter that we measured in the X-ray imply a galactic scale location for the absorbing gas ($d \sim 4$ kpc). In this respect, the warm absorber in 1H 0419-577 represents a unique case, being the first X-ray absorber ever detected so far away from the nucleus. The absorbing gas does not have an emission counterpart since more highly ionized lines which are produced by elements such as O VII, O VIII, and Ne IX, are the most prominent emission features in the X-ray spectrum. The photoionization modeling of the X-ray and UV narrow emission-lines confirmed that they are produced by a more highly ionized gas phase which is located closer (∼1 pc) to the nucleus.

In the present analysis, we exploit the simultaneous UV and optical (thanks to the XMM-*Newton* Optical Monitor) coverage to model the X-ray spectrum in a broadband context using Comptonization. The paper is organized as follows: in Sect. 2.3 , we explain the data reduction procedure; in Sect. 2.4, we present the spectral analysis of our dataset; in Sect. 2.5, we apply our best fit model to the past XMM-*Newton* datasets with the aim of explaining the historical spectral variability; finally we discuss our results in Sect. 2.6 and in Sect. 2.7 we outline our conclusions. The cosmological parameters used are: H_0=70 km s^{-1} Mpc^{-1}, Ω_m=0.3 and Ω_Λ=0.7. The C-statistics (Cash 1979) is used throughout the paper, and errors are quoted at 90% confidence levels ($\Delta C = 2.7$). In all the spectral models presented in the following, we consider the Galactic hydrogen column density from Kalberla et al. (2005, N_H =1.26 × 10^{20} cm^{-2}).

2.3   Observations and data preparation

The source was observed in May 2010 with XMM-*Newton* for ∼167 ks. The observing time was split into two observations (Obs. ID 0604720301 and 0604720401, respectively) which were performed in two consecutive satellite orbits. For the present analysis, we used the EPIC-pn (Strüder et al. 2001) and the Optical Monitor (OM, Mason et al. 2001) data. Besides the HST-COS observation simultaneous to our XMM-*Newton* observation in the UV the source has been observed twice with the Far Ultraviolet Space Explorer (FUSE),

Table 2.2: OM, FUSE, and HST/COS continuum values for 1H0419-577.

Instrument	λ [a]	$\Delta\lambda$ [b]	F_λ [c]	$\frac{\Delta F_\lambda}{F_\lambda}$ [d]	Norm [e]
	Å	Å	erg s^{-1} cm^2 A^{-1}		
OM-b	4340	1307	3.37×10^{-15}	0.2%	$2.9^{+0.7}_{-0.7}$
OM-uvw1	2910	1829	1.10×10^{-14}	0.3%	$3.2^{+1.6}_{-1.1}$
OM-uvm2	2310	1333	1.32×10^{-14}	0.6%	$4.5^{+1.8}_{-0.9}$
OM-uvw2	2120	811	1.40×10^{-14}	0.9%	$3.1^{+2.5}_{-1.4}$
COS	1500	10	2.44×10^{-14}	4%	$2.2^{+1.2}_{-0.7}$
FUSE	1031	10	2.80×10^{-14}	14%	$1.1^{+1.8}_{-0.3}$
FUSE	1110	10	3.66×10^{-14}	16%	$1.7^{+2.2}_{-0.4}$

Notes. [a] Centroid of the spectral bin for each instrument. [b] Spectral bin width. For the OM-filters, we used the filter width. We assigned a narrow spectral width of 10 Å to the COS and FUSE flux measurements. [c] Flux density. [d] Statistical error for the flux density. [e] Intercalibration factor relative to the EPIC-pn, with errors.

respectively, in 2003 and 2006. In this analysis we used the FUSE flux measurements reported in the literature (Dunn et al. 2008, Wakker & Savage 2009). Finally, we retrieved all the available archival datasets from the XMM-*Newton* archive and we used them to study the source variability.

2.3.1 The X-ray data

We processed the present datasets and all the archival Observation Data Files (ODF) with the XMM-*Newton* Science Analysis System (SAS) version 10.0, and with the HEAsoft FTOOLS version 6.12. We refer the reader to Paper I for a detailed description of the data reduction.

For the present datasets, we extracted the EPIC-pn spectra from both 0604720301 and 0604720401 observation. We checked the stability of the spectrum in the two observations, and we found no flux variability larger than $\sim$ 7%. Therefore, we summed the two spectra into a single combined spectrum with a net exposure time of $\sim$ 97 ks after the background filtering. We used the FTOOLS `mathpha` and `addarf` to combine, respectively, the spectra and the Ancillary Response Files (ARF).

We reduced all the archival datasets following the same standard procedure described in Paper I, and we discarded the datasets with ID 0148000301 and 0148000701, because they show a high contamination by background flares. Hence, we created the EPIC-pn spectra and spectral response matrices for all the good datasets.

We fitted all the X-ray spectra in the 0.3–10 keV band and we rebinned them to have at least 20 counts in each spectral bin, although this is not strictly necessary when using the C statistics. In Table 2.1, we provide the most relevant information of each XMM-*Newton* observation, and we label them with numbers, following a chronological order.

2.3.2 The optical and UV data

As also described in Paper I, in our XMM-*Newton* observation OM data were collected in four broad-band filters: B, UVW1, UVM2, and UVW2. In the present analysis, we used the OM filters count-rates for the purpose of spectral fitting. Therefore, we also retrieved the spectral response matrices correspondent to each filter from the ESA website[1]. We corrected the flux in the B filter to account for the host galaxy starlight contribution. For this, we used the same correction factor (56%) estimated in M11 for the stellar bulge of Mrk 509. Since Mrk 509 hosts a BH with a mass similar to the one in 1H 0419-577 , the stellar mass of the bulge should also be similar in this two galaxies (e.g., Merritt & Ferrarese 2001).

In Paper I, we derived a value for the UV flux of the source at 1500 Å from the continuum of the HST-COS spectrum. Moreover, two other UV fluxes measured with FUSE are reported in the literature, at 1031 Å (Wakker & Savage 2009) and 1110 Å (Dunn et al. 2008), respectively. When the overlapping wavelength region between COS (2010 observation) and FUSE (2003 and 2009 observations) is considered, the level of the UV continuum of the source is the same (see Wakker & Savage 2009, Edmonds et al. 2011).Therefore, we could safely fit the FUSE fluxes with the COS, OM, and the EPIC-pn data that were simultaneously taken in 2010. For this purpose, we converted the UV fluxes back to count rates. We used the HST-COS sensitivity curve and the FUSE effective area (see also M11) for this. We outline all the UV and optical continuum values for 1H 0419-577 in Table 2.2. To check for a possible variability of the source in the optical-UV, we also obtained the OM fluxes from the archival XMM-*Newton* observations. For all the archival datasets, except Obs.1, OM data were available in the U, B, V, UVW1, and UVW2 filters.

2.4 Spectral modeling

2.4.1 A phenomenological model

We started with a pure phenomenological modeling of the present EPIC-pn spectrum using SPEX (Kaastra et al. 1996) version 2.04.00. We first attempted to fit the spectrum in the 2.0–10.0 keV energy region with a canonical simple power law ($\Gamma \sim 1.6$). The broadband residuals (Fig. 2.2) show large deviations from this simple model. Besides a prominent soft excess in the 0.3–2.0 keV band, the model does not account for a broad trough between 2.0 and 4.0 keV. To phenomenologically account for this nontrivial spectral shape, a combination of four different spectral slopes would be required all over the 0.3–10.0 keV band. Nonetheless, a prominent peak in the model residuals (Fig. 2.2) at ~ 0.5 keV is still unaccounted. We identified this feature as due to the blend of the O VII-O VIII lines that we detected in the simultaneous RGS spectrum (Paper I). Furthermore, a shallow excess is seen at ~ 5.5 keV. Fitting this feature with a delta-shaped emission line which is centered at the nominal rest frame energy of the Fe Kα line-transition, does not leave any prominent structure in the residuals. If the line width is left free to vary, the fitted

---

[1] `http://xmm2.esac.esa.int/external/xmm_sw_cal/calib/om_files.shtml`
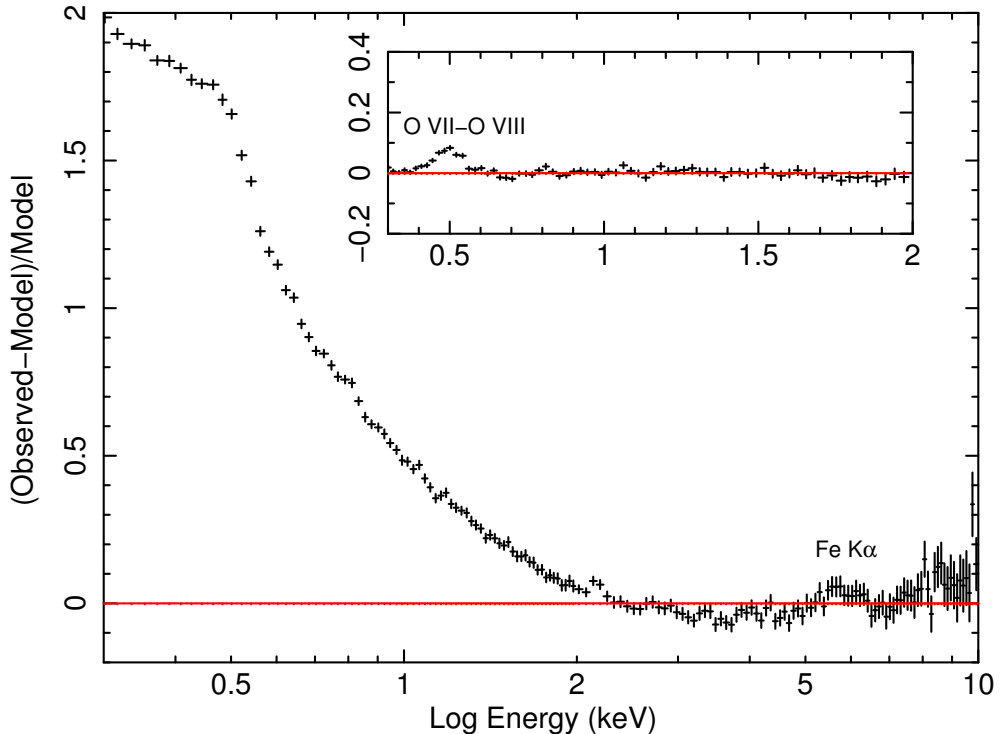
Figure 2.2: *Main Panel*: Model residuals to a power law model in the 0.3–10.0 keV band. A prominent soft excess in the ∼ 0.3–2.0 keV band and a shallow excess at the rest frame energy of the Fe Kα transition are seen. *Secondary Panel*: Model residuals to the broadband phenomenological model in 0.3–2.0 keV band. An arc-shaped feature at the rest frame energy of the O VII-O VIII transitions is seen.

line-width ($\sigma = 300 \pm 200$ eV) is well consistent with what was previously reported for this source (Turner et al. 2009, Pounds et al. 2004a,b). We also attempted also to decompose the Fe Kα in a combination of a broad plus a narrow component, but this exercise did not lead to a conclusive result. Despite the good data quality of the present dataset, the line-width of the broad component and the normalization of the narrow component cannot be constrained simultaneously.

In conclusion, the long exposure time of the present EPIC-pn spectrum unveiled a complex continuum spectral structure, which calls for more physically motivated modeling to be fully understood.

2.4.2 Reflection fitting

At first, we tested a disk reflection scenario for the present spectrum. As noticed in Sect. 2.1, this model has already been successfully applied to Obs. 1–5 (F05). Besides the main

Table 2.3: Best fit parameters for the reflection fitting.

Simple reflection model[a]	
Γ [b]	2.17 ± 0.01
$R_{\rm in}$ [c]	$1.6 \pm 0.1\ R_{\rm g}$
$R_{\rm break}$ [d]	$7 \pm 2\ R_{\rm g}$
$q_{\rm in}$ [e]	5.9 ± 0.3
$q_{\rm out}$ [f]	2.6 ± 0.2
Incl. [g]	20 ± 8
ξ [h]	20.8 ± 0.3
$F_{\rm pow}$ [i]	$16.6 \pm 0.07 \times 10^{-12}\,{\rm erg\ s^{-1}\ cm^2}$
$F_{\rm ref}$ [l]	$7.4^{+0.47}_{-0.08} \times 10^{-12}\,{\rm erg\ s^{-1}\ cm^2}$
C/d.o.f	$383/240$
Composite disk model[m]	
Γ [b]	2.13 ± 0.01
$R_{\rm in,2} = R_{\rm out,1}$ [n]	$1.90 \pm 0.06\ R_{\rm g}$
Incl [g]	41 ± 2
$q_{\rm in}$ [o]	6 ± 2
$\xi_{\rm in}$ [p]	89 ± 11
$q_{\rm out}$ [q]	3.7 ± 0.2
$\xi_{\rm out}$ [r]	20 ± 1
$F_{\rm pow}$ [i]	$15.9 \pm 0.1 \times 10^{-12}\,{\rm erg\ s^{-1}\ cm^2}$
$F_{\rm ref}$ [l]	$8.0 \pm 0.1 \times 10^{-12}\,{\rm erg\ s^{-1}\ cm^2}$
C/d.o.f	$354/240$

Notes. [a] Xspec syntax: PHABS*(POW+KDBLUR2(REFLIONX)). [b] Photon index. [c] Disk inner radius. [d] Break radius above which the emissivity profile of the disk changes slope. [e] Index of the emissivity profile of the disk for $r \leq R_{\rm break}$. [f] Index of the emissivity profile of the disk for $r \geq R_{\rm break}$. [g] Disk inclination. [h] Disk ionization parameter. [i] Unabsorbed flux of the main power law in the 0.5–10 keV band. [l] Unabsorbed flux of the reflected power law in the 0.5–10 keV band. [m] Xspec syntax: PHABS*(POW+KDBLUR(REFLIONX)+KDBLUR(REFLIONX)). [n] Inner radius of the second reflection, which is coupled with the outer radius of the first one. [o] Index of the disk emissivity profile for the first reflection. [p] Disk ionization parameter for the first reflection. [q] Index of the disk emissivity profile for the second reflection. [r] Disk ionization parameter for the second reflection.

power law continuum, the second relevant spectral component in this model is a relativistically smeared reflected power law, which is thought to be produced in an ionized accretion disk.

We fitted the spectrum with Xspec (Arnaud 1996) version 12.0, and we used PHABS to account for the Galactic hydrogen column density along the line of sight. We used REFLIONX (Ross & Fabian 2005) to model the reflected component, and we left the ionization parameter of the reflector free to vary. Hence, we accounted for the relativistic effects
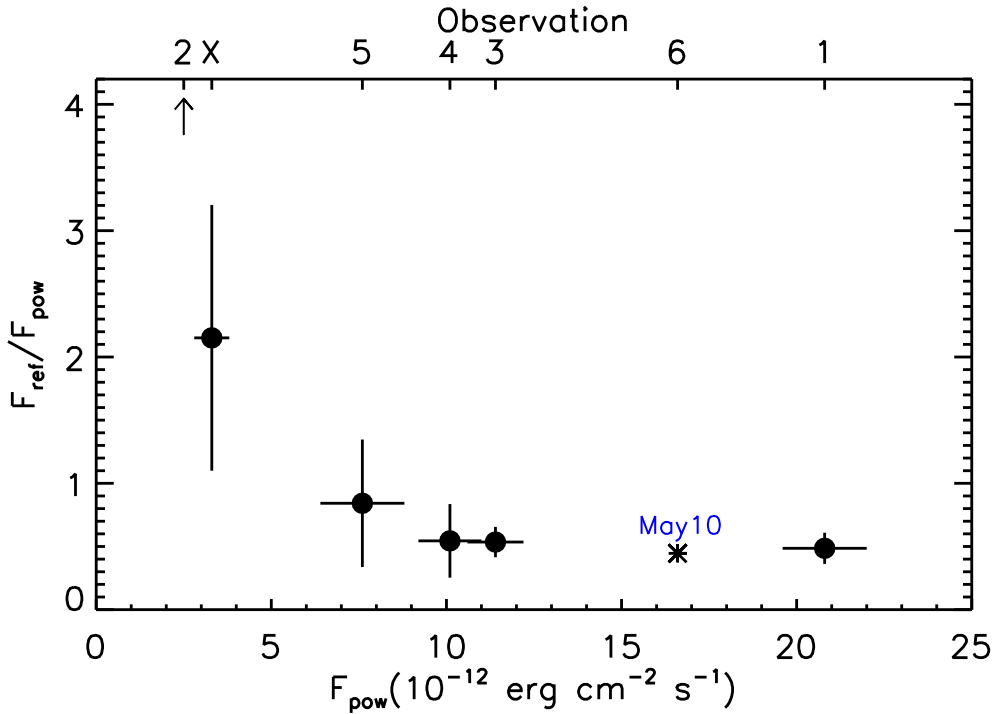
Figure 2.3: Reflection fraction as a function of the power law flux with errors. The reflection fraction is given by the ratio between the 0.5–10.0 keV fluxes of the reflected component to the primary power law. The value for the present dataset is labeled, while all the others data points, including a lower limit indicated by an arrow, are taken from F05. The observation numbers for each data point are labeled on the upper axes (see Table 2.1). Note that the data point labeled with a "X" has not been used in the present analysis (see Sect. 2.3.1).

from an accretion disk that surrounds a rotating black hole (Laor 1991) with KDBLUR2. The free parameters in this component are the disk inclination and inner radius, along with the slopes and the break radius of the broken power law shaped emissivity profile. We kept the outer radius frozen to the default value of 400 gravitational radii (R_g), and we set the iron abundance to the solar value (Anders & Grevesse 1989). We extended the model calculation to a larger energy range (0.1–40 keV) to avoid spurious effects due to a truncated convolution. We also attempted to fit the spectrum with a composite disk model (see F05), by splitting the disk in two regions with different ionization parameters to mimic a more realistic scenario where the disk ionization varies with the radius. However, with a simple reflection model we already obtained a statistically good fit, which was not strikingly improved ($\Delta C = 29$) by using a more complex composite disk model. We list the best fit parameters of the reflection fitting in Table 2.3. Overall, our result agrees with the main predictions of the physical picture proposed in F05. The black hole hosted in 1H 0419-577 may be rapidly spinning, as suggested by the proximity of the fitted disk

inner radius to the value of the innermost stable orbit of a maximally rotating Kerr black hole. The steep emissivity profile of the disk indicates that it is illuminated mostly in its inner part, as it is expected if the primary continuum is emitted very close to the BH. In this framework, the historical source variability is due to the variable light bending, which may produce a negative trend of the reflection fraction with the power law flux. Our results are consistent with the general trend noticed in F05 (Fig. 2.3).

2.4.3   Broadband spectral modeling

The AGN emission can be also produced by thermal Comptonization (see Sect. 2.1). This model has the advantage of explaining AGN emission in a consistent way over the entire optical, UV, and X-ray energy range (e.g., Mrk 509, M11, P13). Indeed, the disk blackbody temperature that can be constrained from a fit of the optical/UV data serves as input for the Comptonized components that produce the X-ray continuum. The model includes both a warm (hereafter labeled as "wc") and a hot Comptonizing corona (hereafter labeled as "hc") to cover the entire X-ray bandpass. Given the simultaneous X-ray, UV, and optical coverage available in the present case, it is worthwhile testing also this scenario.

We fitted the EPIC-pn spectrum of 1H 0419-577 with the COS, FUSE, and OM count-rates with SPEX. We left the normalization of each instrument relative to the EPIC-pn as a free parameter to account for the diverse collecting area of different detectors. In the fit, we both accounted for the Galactic absorption and for the local warm absorber that we detected in Paper I. For the former, we used the SPEX collisionally-ionized plasma model (HOT), setting a low temperature (0.5 eV) to mimic a neutral gas. The cosmological redshift (z=0.104) was also considered in the fit. The final multicomponent model is plotted in Fig. 2.4.

We used the disk-blackbody model (DBB) in SPEX to model the optical-UV emission of 1H 0419-577. This model is based on a geometrically thin, optically thick, Shakura-Sunyaev accretion disk (Shakura 1973). The DBB spectral shape results from the weighed sum of the different blackbody spectra emitted by annuli of the disk located at different radii. The free parameters are the maximum temperature in the disk (T_{max}) and the normalization $A = R_{in}^2 \cos i$, where R_{in} is the inner radius of the disk and i is the disk inclination. Instead, we kept the ratio between the outer and the inner radius of the disk frozen to the default value of 10^3. The best-fit parameters of the disk-blackbody (Fig. 2.4, long dashed line) are: $T_{max} = 56 \pm 6$ eV and $A = (1.2 \pm 0.6) \times 10^{26}$ cm^2. The fitted intercalibration factors between OM, COS, FUSE, and EPIC-pn with errors are reported in Table 2.2. The effect of these intercalibration corrections is within the errors of the disk blackbody parameters given above.

We used the COMT model in SPEX, which is based on the Comptonization model of Titarchuk (1994) to model the X-ray continuum. The seed photons in this model have a Wien-law spectrum with temperature T_0. In the fit, we coupled T_0 to the disk temperature T_{max}. The other free parameters are the electron temperature T and the optical depth τ of the Comptonizing plasma. A combination of two Comptonizing components fits the entire EPIC-pn spectrum. The warm corona ($T_{wc} \sim 0.7$ keV) is optically thick ($\tau_{wc} \sim 7$) and produces the softer part of the X-ray continuum below $\sim$2.0 keV (Fig. 2.4, dotted line). On
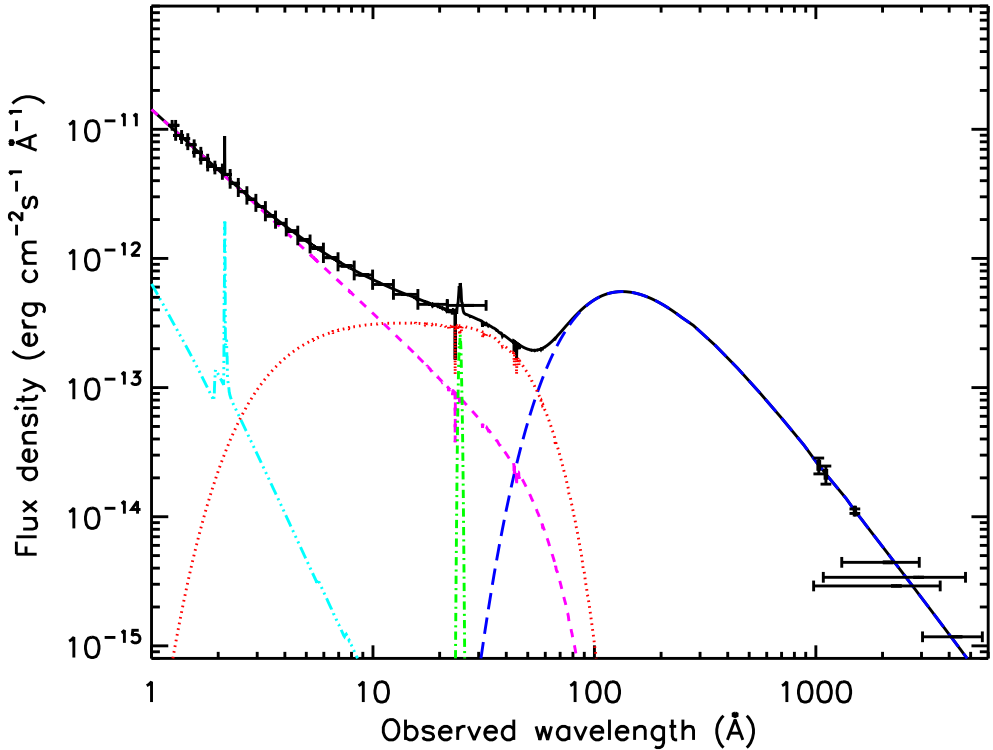
Figure 2.4: Best fit Comptonization model for 1H 0419-577. Solid line: Total model. Crosses: Fluxed EPIC-pn spectrum (rebinned for clarity), OM, COS, and FUSE data points with errors. Long dash line: Disk blackbody component. Dot line: Warm Comptonized component. Dash line: Hot Comptonized component. Dash dot line: Gaussian O VII (triplet) emission line. Dash dot dot line: Cold reflection component, accounting for the Fe Kα emission lines.

the other hand, the hot corona ($T_{hc} \sim 160$ keV) is optically thin ($\tau_{hc} \sim 0.5$) and accounts for the X-ray emission above $\sim$2 keV (Fig. 2.4, dashed line).

 Hence, we identified the remaining features in the model residuals as due to the O VII–O VIII (Fig. 2.4, dash dot line) and Fe Kα emission lines (Fig. 2.4, dash dot dot line). We added a broadened Gaussian line to the fit with the line-centroid and the line-width frozen to the values that we obtained in the RGS fit (Paper I) to account for the O VII emission. The fitted line luminosity is consistent with what is reported in Paper I. The shallower O VIII line that was present in the RGS spectrum is undetected in the EPIC data. In a Comptonization framework, a possible origin for the Fe Kα emission is reflection from a cold, distant matter (e.g., from the torus). We have shown in Sect. 2.4.1 that the Fe Kα line in 1H 0419-577 might also be broad. Detailed study of the properties of the Fe Kα emission line produced in cold matter show that the line may appear broadened in some conditions because of the blend between the main line core and the so-called

Table 2.4: Luminosities of the broadband model components.

Model component	$\log L$ [a]
	erg s^{-1}
Disk blackbody	45.70
Warm corona	44.79
O VII emission line	42.83
Hot corona	45.64
Cold reflection	43.78

Notes. [a] Total intrinsic luminosity.

"Compton shoulder" (see Yaqoob & Murphy 2011). The predicted apparent line broadening is consistent with what we have obtained in Sect 2.4.1 from a phenomenological fit of a possible line-width. We added a REFL component to the fit to test this possibility. We considered an incident power law with a cutoff energy of 150 keV with the same slope and normalization that we derived from the phenomenological fit (Sect. 2.4.1). We set a null ionization parameter and a low gas temperature ($T \sim 1\,eV$) to mimic a neutral reflector, and, to adapt the model to the data, we left only the scaling factor [2] (s) free to vary. A reflected component with $s = 0.3 \pm 0.1$ satisfactorily fits the Fe Kα line and slightly adjusts the underlying continuum ($\Delta C = -7$).

We list the luminosities of all the model components in Table 2.4, while the parameters and errors of the Comptonized components are outlined in Table 2.5.

2.5 The historical spectral variability

2.5.1 The baseline model

In Fig. 2.5, we plot the historical X-ray, optical, and UV fluxes of 1H 0419-577 from the archival XMM-*Newton* observations and from the present dataset. The optical-UV flux of the source has been stable throughout the ~8 years during which OM observations are available (Obs 2–6). Nevertheless, as already pointed out in Sect. 2.2 the source has been observed by XMM-*Newton* in a variety of flux states in the soft X-rays (see Fig. 2.5), ranging from the deep flux minimum of September 2002 (Obs.2) to the highest state of December 2000 (Obs.1). We used the Comptonization model that successfully fitted the present dataset as a baseline model for the fit of the past XMM-*Newton* observations. Because the maximum observed variability in the optical-UV ($\sim 20\%$) is within the errors in the disk blackbody parameters that we derived in the broadband fitting (Sect. 2.4.3), we assumed the same seed photons temperature of the present dataset in the baseline model.

---

[2] In the REFL model, the total spectrum $N(E)$ is given by $N(E) = N_i(E) + sR(E)$, where $N_i(E)$ is the incoming spectrum, $R(E)$ is the reflected spectrum, and s is the scaling factor. See the SPEX manual for details.
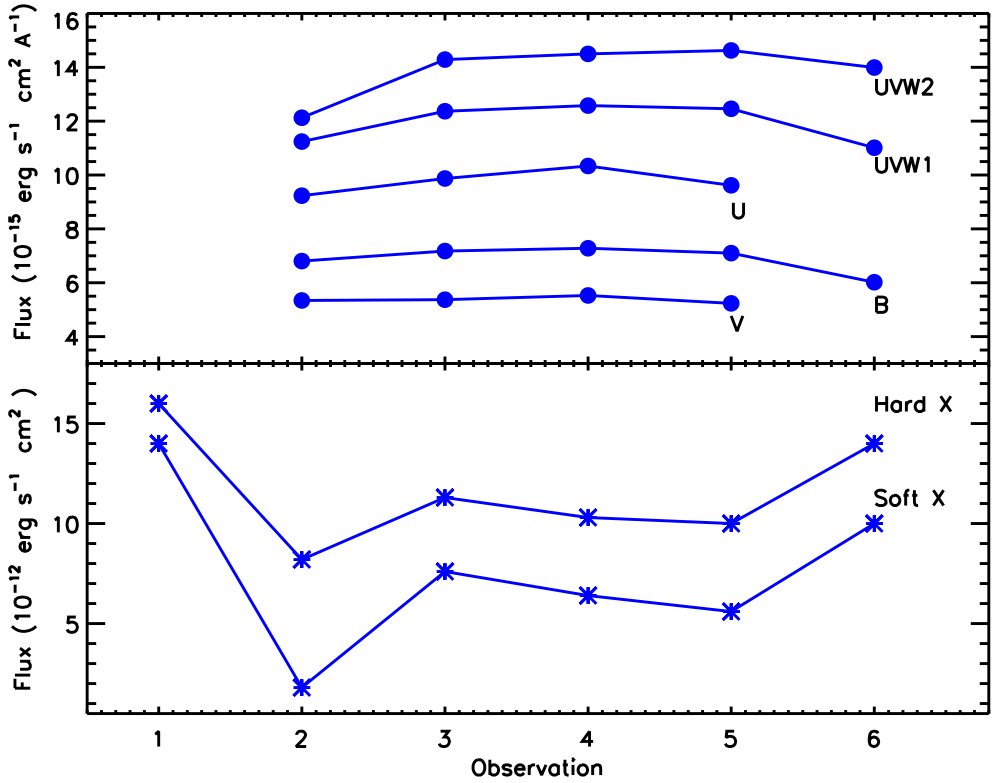
Figure 2.5: *Upper panel*: Variability of the optical and UV fluxes in the OM broadband filters for the archival and present XMM-*Newton* datasets. *Lower panel*: Variability of the soft (0.5–2.0 keV) and hard (2.0–10.0 keV) X-ray fluxes.

In Fig. 2.6, we plot the historical fluxes of the Fe Kα emission line that were measured from a phenomenological fit of the archival and present XMM-*Newton* datasets in the 2.0–10.0 keV band. Although the line is not well constrained in any of the archival datasets, its flux is, however consistent to have been stable in the ∼ 10 years long period covered by XMM-*Newton* observations. Therefore, the cold reflection continuum associated to the Fe Kα line should have remained constant. Since we are mainly interested in studying the source variability in the soft X-ray band, we included just a delta function to account for the Fe Kα emission line in the baseline model. Indeed, the addition of a cold reflection continuum is not critical for the resulting parameters. Finally, we included unresolved O VII-f and O VIII-Lyα emission lines in the baseline model. Previous analysis of the RGS spectrum (Pounds et al. 2004b) has shown that O VII and O VIII lines were present in Obs 2–5. The baseline model provides a formally acceptable fit for all the datasets except Obs. 2, namely the lowest flux state.
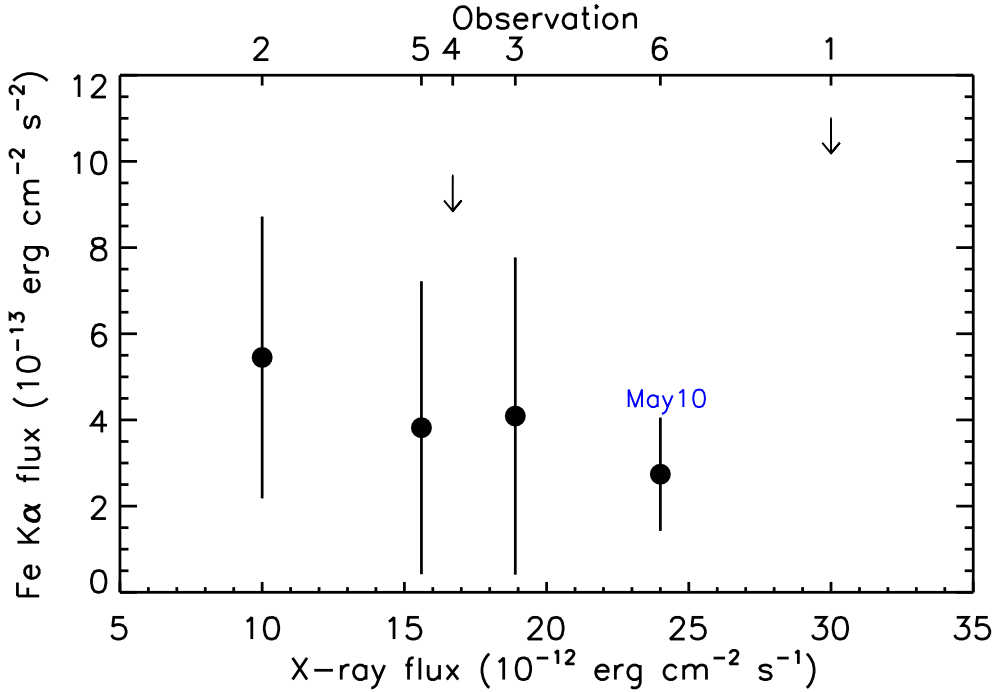
Figure 2.6: Historical and present observed fluxes of the Fe Kα emission line with errors as a function of the source flux in the 0.5–10.0 keV band. The arrows represent upper limits for the line flux. The value for the present dataset is labeled, and the observation numbers for each data point (see Table 2.1) are labeled as well on the upper axes.

2.5.2   The low flux state

We show a comparison between the low-state spectrum and the present dataset in Fig. 2.7. At a first glance, the spectrum appears much flatter in the $\sim$1.0-2.0 keV band and displays a peak at $\sim$0.5 keV resembling the shape of an emission line. Indeed, this feature is well modeled by the O VII-O VIII emission lines that are present in the baseline model. The fitted line fluxes ($F_{O\,VII} = (16 \pm 8) \times 10^{-5}$ photons s^{-1} cm^{-2} and $F_{O\,VIII} = (8 \pm 4) \times 10^{-5}$ photons s^{-1} cm^{-2}) are consistent with what previously reported for the RGS spectrum of this dataset (Pounds et al. 2004a). The residuals to the baseline model display a deep trough, approximately in the same energy region where the spectrum flattens out with respect to the present dataset. We added to the fit a neutral absorber located at the redshift of the source, modeled by a cold (T=0.5 eV) collisionally-ionized plasma (HOT model in SPEX) to attempt adapting the baseline model to the low-state spectrum. By letting all the Comptonized emission being absorbed by a partially covering ($\sim$ 60%), thick ($N_H \sim 5 \times 10^{22}$ cm^{-2}) cold gas, we achieved a statistically good (C/d.o.f.=163/152) fit to the data, accounting for all the features left in the residuals by an unabsorbed model.
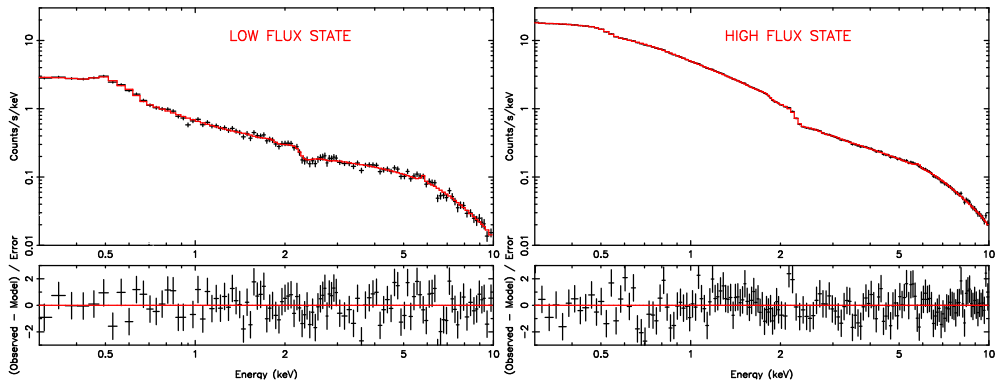
Figure 2.7: EPIC-pn spectrum of 1H 0419-577 in the low flux state (Obs.2, *left panel*) and in the present intermediate flux state (Obs.6, *right panel*). The best fit Comptonization model is displayed as a solid line. Model residuals, in terms of σ, are also shown. We rebinned the spectra for clarity purposes. Note that error bars are as large as the thickness of the model line for the present dataset.

2.5.3   Partial covering of the baseline model

Prompted by the results of the low state fit, we checked if the addition of a cold absorber could also improve the fit of the other datasets. We outline the results of this exercise for all the archival datasets in Table 2.5. An additional partially-covering absorbing component with a similar covering factor ($\sim 50\%$) but a lower column density provides a significant improvement of the fit for Obs. 3–5. In contrast, no absorbing component is statistically required in the fit of Obs. 1 and and 6, namely the two highest flux states. For these datasets, we set an upper limit to the absorbing column density by keeping the covering factor fixed to ~ 0.5. In Fig. 2.8, we plot the parameters of the absorber as a function of the source flux. The absorbing column density shows a negative trend with the flux, while the covering fraction is consistent to be constant. The variable absorbing component does not, however, account for all the source variability. As we show in Fig. 2.9, we still observe an intrinsic variability in both the two Comptonized components after removing the effect of the variable absorption.

We also tested a different scenario where the absorber is constant in opacity and its variability is driven only by a variable covering fraction. At this purpose, we attempted to fit Obs. 4 and 5 keeping the absorber column density frozen to the value observed in the low-flux state and letting only the covering factor free to vary. In both cases, we had to release the parameters of the underlying continuum to achieve an acceptable fit. In detail we obtained a covering factor of $\sim 4\%$ for Obs. 4 but the model residuals are important between 2 and 5 keV. In Obs. 5, the fit erases the absorber pushing the covering factor to a much lower value ($\sim 0.03\%$). In both cases, the fit is statistically worse (C/d.o.f=216/152 and 152/139 respectively) than what is reported in Table 2.5. Thus, we rejected this possibility, and we concluded that the absorber model outlined in Table 2.5 better fits the data.

Table 2.5: Best fit parameters and errors, for the absorbed Comptonization model.

Obs	T_{wc} [a] keV	τ_{wc} [b]	$F^{wc}_{0.5-10.0\,keV}$ [c] 10^{-12}erg s^{-1} cm^2	T_{hc} [a] keV	τ_{hc} [b]	$F^{hc}_{0.5-10.0\,keV}$ [c] 10^{-12}erg s^{-1} cm^2	C/d.o.f. [d]	N_H [e] 10^{21} cm^{-2}	C_V [f]	ΔC [g]
1	1.1 ± 0.2	6.5 ± 0.9	5.8 ± 0.5	140 ± 30	0.2 ± 0.1	24 ± 1	157/141	≤1	0.5 (f)	-7
2	0.6 ± 0.1	5.3 ± 0.6	0.45 ± 0.05	150^{+80}_{-40}	0.7 ± 0.3	9.1 ± 0.6	314/151	47 ± 10	0.6 ± 0.1	-143
3	0.7 ± 0.1	6.3 ± 0.5	4.6 ± 0.8	160 ± 60	0.3 ± 0.2	14.3 ± 0.3	187/151	7 ± 3	0.5 ± 0.1	-26
4	0.67 ± 0.09	7.6 ± 0.7	4.3 ± 0.9	130^{+70}_{-40}	$0.6^{+2}_{-0.2}$	13 ± 1	158/139	9 ± 4	0.5 ± 0.2	-14
5	0.46 ± 0.05	9.0 ± 0.7	2.9 ± 0.5	170 ± 40	0.3 ± 0.2	12.6 ± 0.1	202/139	11 ± 3	0.5 ± 0.2	-62
6	0.7 ± 0.4	6.9 ± 0.5	5.9 ± 0.6	160 ± 30	0.5 ± 0.1	18.1 ± 0.2	293/240	≤0.002	0.5 (f)	-0.3

Notes. [a] Plasma temperature of the Comptonized components. [b] Plasma optical depth of the Comptonized components. [c] Observed flux of the Comptonized components in the quoted band. [d] C-statistic for the unabsorbed model. [e] Column density of the local neutral absorber. [f] Covering fraction of the local neutral absorber. [g] Decreasing of the C-statistic with respect to the unabsorbed model.

2.6 Discussion

2.6.1 The X-ray spectrum of 1H 0419-577

The long exposure XMM-*Newton* observation of 1H 0419-577 that we presented in this paper provided a high-quality X-ray spectrum which is suitable for testing physically motivated models against real data. Exploiting the simultaneous coverage in the optical/UV that was provided in the present case by the OM and by HST-COS, we successfully represented the broadband spectrum of 1H 0419-577 using Comptonization. The emerging physical picture provided that the optical-UV disk photons ($T \sim 56$ eV) are both Comptonized by an optically thick ($\tau_{wc} \sim 7$) warm medium ($T_{wc} \sim 0.7$ eV) and by an optically thinner ($\tau_{hc} \sim 0.5$) and hotter ($T_{hc} \sim 160$ keV) plasma to produce the entire X-ray spectrum.

A similar interpretation has been recently proposed for the broadband simultaneous spectrum of Mrk 509 (M11, P13) and also for a sample of unobscured type 1 AGN (Jin et al. 2012). A reasonable configuration for these two media in the inner region of AGN is possible. Two different Comptonizing coronae may be present. The geometrically compact hot corona may be associated with the inner part of the accretion flow, while the warm corona may be a flat upper layer of the accretion disk (P13). Alternatively, according to a model proposed in Done et al. (2012), the warm Comptonization may take place in the accretion disk itself below a critical radius after which the radiation cannot thermalize anymore. It is in principle also possible that the seed photons are provided to the hot corona by the soft excess component (e.g., PKS 0558-504, Gliozzi et al. 2013). We note that the broadband spectrum of 1H 0419-577 is consistent with a "nested-Comptonization" scenario provided a slightly thicker warm Comptonized component ($\tau \sim 11$). Finally, we suggest that the Fe Kα emission line in 1H 0419-577 is produced by reflection in a cold thick torus. The long-term flux stability of the line that we note in Fig. 2.6 supports this
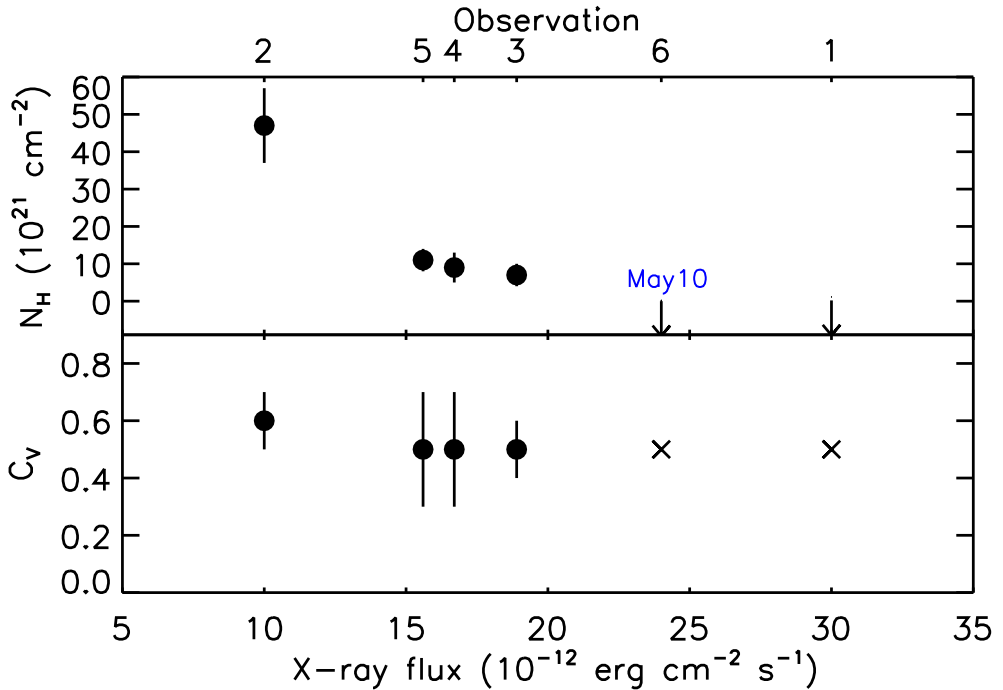
Figure 2.8: Variability of the local neutral absorber in 1H 0419-577. The gas column density (*upper panel*) and and covering factor (*lower panel*) with errors are plotted against the observed source flux in the 0.5–10.0 keV band. Arrows represent upper limits for the column density. Crosses represent fixed values for the covering factor. The values for the present dataset are labeled, and the observation numbers for each data point (see Table 2.1) are labeled as well on the upper axes.

interpretation.

Tombesi et al. (2010) reported the detection of an ultra fast outflow (UFO) in 1H 0419-577. According to these authors, the signature of the UFO is a blushifted Fe XXVI-Ly α absorption line located at a restframe energy of $\sim$7.23 keV which is possibly accompanied by a Fe XXV feature at ~ 8.4 keV. Despite the high signal-to-noise ratio none of these features is evident in the present spectrum. We estimated upper limits for the equivalent width (EW) of the main UFO absorption lines, assuming the same outflow velocity given in Tombesi et al. (2010, v$\sim$11100 km s^{-1}). The deepest UFO that is consistent with our dataset is much shallower than what previously reported, because we found $EW \lesssim 12$ eV and $EW \lesssim 9$ eV for the Fe XXVI-Ly α and Fe XXV-Heα transition, respectively.

2.6.2 The historical spectral variability of 1H 0419-577

The Seyfert galaxy 1H 0419-577 is well known for showing a remarkable flux variability in the X-rays that is accompanied by a dramatical flattening of the spectral slope as the
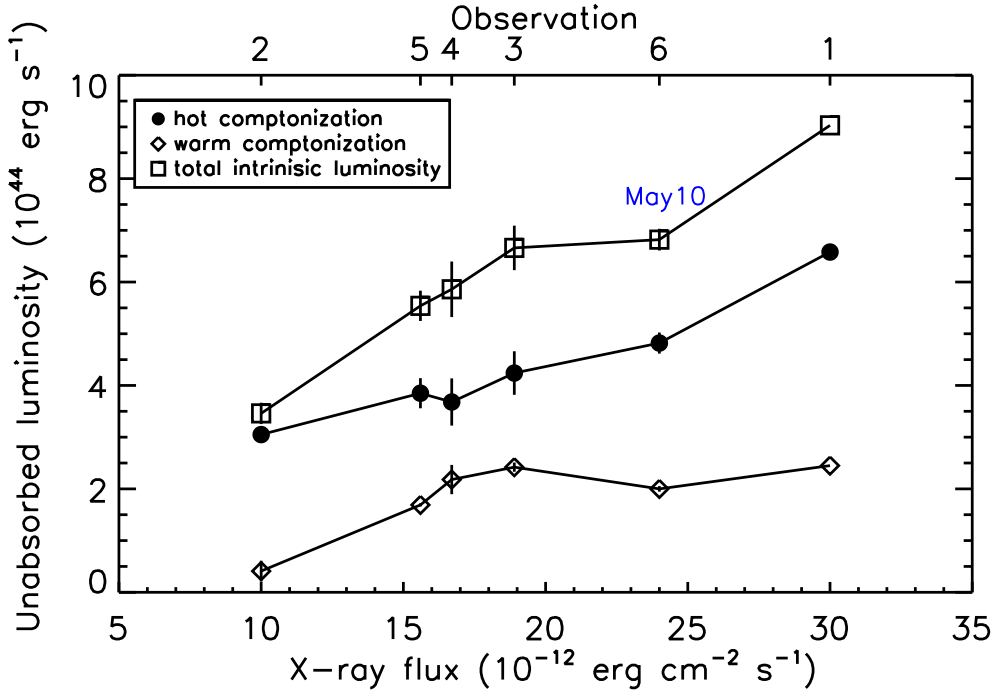
Figure 2.9: Variability of the intrinsic 0.5–10.0 keV luminosity in 1H 0419-577. The unabsorbed luminosities of the hot and the warm Comptonized component, along with the total intrinsic luminosities are plotted against the observed source flux in the 0.5–10.0 keV band. The symbols are outlined in the legend. Error bars, when larger than the size of the plotted symbols, are also shown. The values for the present dataset are labeled and the observation numbers for each data point (see Table 2.1) are labeled as well on the upper axes.

source flux decreases. Nonetheless, the optical/UV fluxes that were observed in diverse X-ray flux states are rather stable. In Sect. 2.5, we showed that a Comptonization model can explain the historical spectral variability of 1H 0419-577 , provides an intrinsic variability of the two Comptonized components, and a partially-covering, cold absorption variable in opacity.

The intrinsic variability of the X-ray Comptonized continuum is easy to justify. Indeed, Monte Carlo computations of X-ray spectra from a disk-corona system show that coronae may be intrinsically variable even when given an optical depth and a electron temperature. Without requiring variations in the accretion rate that would be inconsistent with the stability of the optical/UV flux, a substantial variability may be induced, for instance, by geometrical variations (e.g., Sobolewska et al. 2004) or by variations in the bulk velocity of the coronal plasma (e.g., in a non static corona, Malzac et al. 2001).

However, apart from the smaller intrinsic variation, the variable cold absorption causes the bulk of the observed spectral variability. In this respect, 1H 0419-577 is not a unique

case. So far, cold absorbers variable on a broad range of timescales (few hours–few years) have been detected in a handful of cases, (e.g., NGC 1365, NGC 4388, and NGC 7582, Risaliti et al. 2005, Elvis et al. 2004, Piconcelli et al. 2007) including some optically unobscured, standard type 1 objects (e.g., NGC 4151, 1H0557-385, Mrk 6 Puccetti et al. 2007, Longinotti et al. 2009, Immler et al. 2003) and narrow line Seyfert 1 (e.g., SWIFT J2127.4+5654 Sanfrutos et al. 2013). In most of these cases, discrete clouds of cold gas with densities and sizes typical of the BLR clouds may cause the variable absorption. The estimated location of these clouds is within the "dust sublimation radius", which nominally separates the BLR and the obscuring torus. This indicates that the distribution of absorbing material in AGN may be more complex than the axisymmetric torus that is prescribed by the standard Unified Model (see Bianchi et al. 2012, and references therein). The variation of the cold absorber in 1H 0419-577 is driven by a decreasing opacity, which seems to show a trend with the increasing flux (Fig. 2.8, upper panel). In in the two highest flux spectra, the absorbing column density is consistent to have been at least a factor ~ 40 thinner than in the lowest flux spectrum. At the same time, the absorber covering factor remained constant (~ 0.5) within the given errors. A simple explanation for this behavior is that the neutral column density became ionized in the highest flux dataset because it responded to the enhanced X-ray ionizing continuum. An inspection of the archival RGS spectra (Pounds et al. 2004a,b) may provide additional support to this hypothesis. The broad emission features from O VII and O VIII that we detected in the RGS spectrum of the present dataset (Paper I) are also present in all the past RGS spectra. We note, however, that in the present dataset, the luminosity of both these lines is lower than what was observed, for instance, in the lowest flux state (e.g., by a factor ~ 2 and ~ 5, respectively) Moreover, we clearly detected a broad line from a more highly ionized species (Ne IX, see Paper I), which is undetected in all the archival RGS spectra. This may be a qualitative indication of a more highly ionized gas in the BLR during the higher flux state. The enhanced flux may have increased the ionization of the gas, causing the enhancement of the Ne IX and the decrease of the O VII-O VIII. The difference in unabsorbed continuum luminosities that we observed, for instance, between the lowest flux state of September 2002 and the following observation of March 2003 ($\Delta L \sim 3 \times 10^{44}$ erg s^{-1}, see Fig. 2.9) may indeed ionize a cloud of neutral hydrogen with typical BLR density in the observed timescale ($\Delta t \lesssim 7$ months). Assuming that the absorber is a cloud of pure hydrogen that does not change in volume as a consequence of the ionization, then the fraction of hydrogen that became completely ionized in March 2003 is as follows:

$$f_{\mathrm{H}} = \frac{N_{\mathrm{H,Sep02}} - N_{\mathrm{H,Mar03}}}{N_{\mathrm{H,Sep02}}} \sim 85\%. \tag{2.1}$$

If the cloud is illuminated by ΔL the conservation of energy, assuming spherical symmetry implies that:

$$\frac{C_{\mathrm{V}} \Delta L \Delta t}{f \frac{4\pi}{3} d^3} \sim U_{\mathrm{H}} f_{\mathrm{H}} n_{\mathrm{H}}. \tag{2.2}$$

where C_v is the absorber covering factor, d is the absorber distance, U_{H}=13.6 eV is the ionization threshold of hydrogen, n_{H} is the absorber density, and $f = 10^{-2}$ is the volume

filling factor of the broad line region (Osterbrock 1989). Taking the dust sublimation radius ($R_{\mathrm{DUST}} \sim 0.6\,\mathrm{pc}$ [3]) as an upper limit for the absorber distance from Equation 2.2 follows that

$$n_{\mathrm{H}} \gtrsim 6 \times 10^8\,\mathrm{cm}^{-3}. \tag{2.3}$$

This lower limit is well consistent with the typical range of densities of the BLR clouds ($10^8 - 10^{12}\,\mathrm{cm}^{-3}$, Baldwin et al. 1995).

We also note that this scenario resulted in a statistically better fit of the data than a model mimicking a single cloud with a constant opacity crossing the line of sight (see Sect. 2.5.3). Indeed, the time interval of a few months separating the XMM-*Newton* observations of 1H 0419-577 is inconsistent with the expected duration of an occultation event due to a single BLR cloud. For instance the occultation observed in NGC 1365 (in April 2006, see Risaliti et al. 2007) lasted ~4 days. A similar eclipse, lasting only 90 ks, has been observed in SWIFT J2127.4+5654 (Sanfrutos et al. 2013).

In the scenario we are proposing for 1H 0419-577, when the continuum source is found in a low flux state, the surrounding gas is on average less ionized. We suggest, therefore, that in these conditions the number of neutral clouds along the line of sight may be larger, making obscuration events more probable.

We finally remark that a simple argument can explain the stability of the optical/UV continuum in 1H 0419-577 in this framework. The optical/UV continuum source is 10 times larger in radius than the X-ray source (see e.g., Elvis 2012). Therefore, a covering on the order of $\sim 50\%$ of the X-ray source implies a negligible covering of the $\sim 0.5\%$ for the optical/UV source.

2.6.3 The geometry of AGN

We can put significant constraints on the geometry of 1H 0419-577 from the fitted parameters of the disk blackbody (Sect. 2.4.3). The fitted disk blackbody normalization A is linked to the disk inclination angle i. Analytically,

$$A = R_{\mathrm{in}}^2 \cos i, \tag{2.4}$$

where R_{in} is the inner radius of the disk. The disk inner radius may be set by the radius of the innermost stable circular orbit (R_{ISCO}), which is allowed in the space-time metric produced by the black hole mass ($M \sim 3.8 \times 10^8\,\mathrm{M}_\odot$ in this case, O'Neill et al. 2005) and by its spin. The two extreme cases are a maximally rotating black hole and a non-rotating Schwarzschild black hole (see Bambi 2012). Therefore, according to this general prescription, R_{in} may only vary in the range:

$$R_{\mathrm{in}} \sim R_{\mathrm{ISCO}} = [1-6]\,R_{\mathrm{g}}, \tag{2.5}$$

where $R_g = 2GM/c^2$ is the gravitational radius, G is the gravitational constant, and c is the speed of light. Combining Equations 2.4 and 2.5, we obtain:

$$i = [70^\circ - 89^\circ]. \tag{2.6}$$

---

[3]We estimated the dust sublimation radius of 1H 0419-577 using the ionizing luminosity given in Paper I and the formula of Barvainis (1987), assuming T=1500 K for the dust sublimation temperature and a=0.05 μm for the dust grains size.

To set a more robust lower limit for the disk inclination angle, we additionally considered the error of the disk normalization (Sect. 2.4.3) and of the black hole mass (~ 0.5 dex, see O'Neill et al. 2005, and references therein) in the calculation. With these tighter constraints:

$$i \gtrsim 54°. \tag{2.7}$$

These inclination values are well consistent with the intermediate spectral classification of 1H 0419-577 as Seyfert 1.5. It is therefore possible that our viewing direction toward 1H 0419-577 is grazing the so-called "obscuring torus" that is prescribed by the standard Unified Model (Antonucci 1993). In this framework, the inner part of the torus may be responsible for the X-ray obscuration.

The structure of the obscuring medium in AGN may be more complex than the classical donut torus paradigm. Indeed, this model faces difficulties in explaining several theoretical and observational issues, including, for instance, the wide range of X-ray obscuring column densities (see Elvis 2012, and references therein). A clumpy torus (Nenkova et al. 2008) may alleviate part of these problems. In the latter case, when the numerical density of clouds along the line of sight is low, even a source viewed from a high inclination angle may appear like a Seyfert 1 (see also Elitzur 2012). Moreover, in this model, the BLR and the torus itself are part of the same medium, decreasing in ionization as the distance from the central source increases. Indeed, it has been proposed (see Nenkova et al. 2008) that the clumpy torus extends inward beyond the dust sublimation point. The innermost torus clouds, being more exposed to the ionizing radiation, are probably dust free and may dominate the X-ray obscuration. Given the high viewing angle derived above, 1H 0419-577 may possibly fit in this framework.

2.6.4   A comparison with other models

The model that we presented in this paper explains both the optical/UV/X-ray broadband spectrum and the historical variability of 1H 0419-577 in a reasonable geometrical configuration. However, the hard X-ray energy range above 10 keV is not covered by the present spectral analysis. In that range, 1H 0419-577 displays a "hard-excess" (Turner et al. 2009, Pal & Dewangan 2013, Walton et al. 2010) over a simple power law model, that shows some evidence of variability (a factor ~ 2, see Turner et al. 2009). The extrapolation to harder energies of our broadband model predicts a flux of $\sim 2.9 \times 10^{-11}$ erg s^{-1} cm^2 in the 10–50 keV band. This flux is higher than the 70 month-averaged flux observed with BAT in the same band ($\sim 2.2 \times 10^{-11}$ erg s^{-1} cm^2, Baumgartner et al. 2013) but well consistent with the latest *Suzaku* measurement taken only 5 months before our XMM-*Newton* observations ($\sim 2.7 \times 10^{-11}$ erg s^{-1} cm^2, Pal & Dewangan 2013). Because of this relatively short time interval between the *Suzaku* and XMM-*Newton* observation, it is indeed likely that *Suzaku* caught the source in the same flux condition of our observation (see also Fig. 2.1). In the context of the *Suzaku* data analysis (Pal & Dewangan 2013), the authors also attempted to fit a Comptonization model to the May 2010 EPIC-pn spectra. They obtained, however, a poor result mainly because of a prominent excess in the residuals near ~ 0.5 keV. In the present analysis, thanks to the higher resolution provided by the

RGS, we could easily identify that feature as due to the O VII line complex. Apart from this discrepancy, the parameters they obtained for the warm Comptonized component reasonably agree with our result.

On a different occasion (July 2007), *Suzaku* caught the source in a bright state, similar to what was observed by XMM-*Newton* in December 2000 (Obs.1). The hard X-ray curvature that was observed in that case ($F_{15-50\,keV} \sim 2.6 \times 10^{-11}$ erg s^{-1}) can be fitted using a Compton-thick, highly ionized absorption, covering $\sim$66% of the line of sight. To check if our model could also explain this historical hard X-ray maximum, we compared the hard X-ray flux extrapolated by the fit of Obs. 1 with the one observed by *Suzaku*. We noted a small disagreement as the flux predicted by our model is by a factor of 1.6 lower than the observed one. Thus, we cannot definitively rule out that a partially-covering ionized absorber was present in the high flux state of July 2007. In the framework proposed in this paper, it may in principle be the ionized counterpart of the cold absorber present in the low flux state.

Besides our interpretation, the light bending model may also explain the variable X-ray spectrum of this source and fits both the XMM-*Newton* and the *Suzaku* datasets (F05, Walton et al. 2010, Pal & Dewangan 2013, this paper). We note, however, that a variable absorption is required to fit the data even in this disk-reflection framework. Indeed, a cold absorber showing the same trend noticed here (with a column density dropping from $N_H \simeq 10^{21}$ cm^{-2} to 0) is present in the F05 model. Additionally, an O VII edge with a variable depth, which mimics an ionized warm absorber, is also included. The latter is somewhat at odds with what we reported in Paper I because the warm absorber in 1H 0419-577 is too lowly ionized to produce any strong O VII absorption features. Moreover, a short timescale variation of the ionized absorption edges, as required in F05, is difficult to reconcile with the galactic scale location (see Paper I) of the warm absorber in this source. In our analysis, solar abundances are adequate to fit the data. In the light bending model, the metal abundance in the disk is a free parameter, and it has been reported to vary from supersolar in September 2002 ($\sim$ 3.8, F05) to undersolar in January 2010 ($\sim$0.5, Pal & Dewangan 2013). This is another issue that is difficult to explain. Finally, we note that a physical interpretation of the source variability that is observed with *Suzaku* is not possible in the context of the light bending model alone, and additional variability in the disk-corona geometry, possibly caused by a variability in the accretion rate (that would be however inconsistent with the stability of the optical/UV flux noticed here) has to be invoked (Pal & Dewangan 2013).

In conclusion, the Comptonization model proposed here for the present and historical broadband spectrum of 1H 0419-577 does not rule out other possible interpretations. It has, however, the advantage of explaining all the observational evidences collected in the last ten years over the broadest range of wavelength available without requiring any special *ad hoc* assumption. A future observation in the entire X-ray band with XMM and NuSTAR would be important to solve the long-standing ambiguity in the interpretation of the spectral variability in this peculiar Seyfert galaxy.

2.7 Summary and conclusions

We modeled the broadband optical (XMM-OM), UV (HST-COS, FUSE), and X-ray (EPIC-pn) simultaneous spectrum of 1H 0419-577 taken in May 2010 using Comptonization. The X-ray continuum may be produced by a warm ($T_{wc} \sim 0.7$ keV, $\tau_{wc} \sim 7$) and a hot Comptonizing medium ($T_{hc} \sim 160$ keV, $\tau \sim 0.5$) which are both fed by the same optical/UV disk photons ($T_{dbb} \sim 56$ eV). The hot medium may be a geometrically compact corona located in the innermost region of the disk. The warm medium may be an upper layer of the accretion disk. Reflection from cold distant matter is a possible origin for the Fe Kα emission line. Despite the long exposure time of our dataset, we do not find evidence of the ultra fast outflow features that have been reported in the past for this source.

Providing a partially covering ($\sim$50%) cold absorber with a variable opacity ($N_H \sim [10^{19} - 10^{22}]$ cm^{-2}) and a small variability intrinsic to the source, this model can also reproduce the historical spectral variability of 1H 0419-577. The opacity of the absorber increases as the continuum flux decreases. We argue that the absorber may have the typical density of the BLR clouds and that it becomes optically thinner in the higher flux states because it gets ionized in response to the enhanced X-ray continuum.

Relativistic light-bending remains an alternative explanation for the spectral variability in this source. We note, however, that a variable elemental abundance and a variable absorption are required in this scenario. The latter is difficult to reconcile with the UV/X-rays absorber that we have determined to be located at a $\sim$ kpc scale.

Finally, we suggest that 1H 0419-577 may be viewed from a high inclination angle which marginally intercepts a possibly clumpy obscuring torus. In this geometry, the X-ray obscuration may be associated with the innermost dust free region of the obscuring torus.

The present spectral analysis in the optical/UV/X-ray represents a substantial step forward in the comprehension of this intriguing Seyfert galaxy. However, further investigations (e.g., with NuSTAR) are needed to understand the true nature of the spectral variability of this source.

3 ⸺ Anatomy of the AGN in NGC 5548:

V. The short-term variability of the outflows

Abstract

During an extensive multiwavelength campaign that we performed in 2013-14, we found the prototypical Seyfert 1 galaxy NGC 5548 in an unusual condition of heavy and persistent obscuration. The newly discovered "obscurer" absorbs most of the soft X-ray continuum along our line of sight and lowers the ionizing luminosity received by the classical warm absorber. We present the analysis of the high resolution X-ray spectra collected with XMM-*Newton and Chandra throughout the campaign, which are suitable to investigate the variability of both the obscurer and classical warm absorber. The time separation between these X-ray observations range from two days to eight months. On these timescales the obscurer is variable both in column density and in covering fraction. This is consistent with the picture of a patchy wind. The most significant variation occurred in September 2013 when the source brightened for two weeks. A higher and steeper intrinsic continuum and a lower obscurer covering fraction are both required to explain the spectral shape during the flare. We suggest that a geometrical change of the soft X-ray source behind the obscurer causes the observed drop in the covering fraction. Because of the higher soft X-ray continuum level, the September 2013 Chandra spectrum is the only X ray spectrum of the campaign in which individual features of the warm absorber could be detected. The spectrum shows absorption from Fe-UTA, O IV, and O V, consistent with belonging to the lower-ionization counterpart of the historical NGC 5548 warm absorber. Hence, we confirm that the warm absorber has responded to the drop in the ionizing luminosity caused by the obscurer.*

3.1 Introduction

In the X-ray band, active galactic nuclei (AGN) are variable emitters. The origin of this variability, which can be even large and fast (e.g., Matt et al. 2003), is not fully understood yet (see e.g. McHardy et al. 2006, Turner et al. 2009, Ponti et al. 2012). Variable absorption of the X-ray radiation along the line of sight is one of the possible explanations. Indeed, many absorbing components, spanning a broad range in ionization, can be detected in AGN X-ray spectra.

Cold neutral absorption is able to strongly suppress the soft X-ray flux and to change the curvature of the X-ray spectrum. In recent years, evidence for variability due to cold X-ray absorption in both type 1 and type 2 AGN has increased. In many cases, changes in the absorber column density and/or covering fraction, on timescales of a few hours or a few years, have been reported, e.g., in NGC 4388 (Elvis et al. 2004), NGC 4151 (Puccetti et al. 2007), and 1H 0557-385 (Coffey et al. 2014). On these same timescales, the X-ray absorbing column density may even drastically switch from Compton thick to Compton thin as observed in several type 2 AGN, e.g., NGC 7582 (Piconcelli et al. 2007), UGC 4203 (Risaliti et al. 2010), and NGC 454 (Marchese et al. 2012). This rich phenomenology suggests that cold gas is present even in the innermost region of AGN (see Bianchi et al. 2012). This material is probably patchy and may belong to the broad line region (BLR) or to a clumpy torus (e.g., Miniutti et al. 2014). In the best studied Seyfert 1.8 source, NGC 1365, a single cloud was monitored while eclipsing the central X-ray source for a few hours (Risaliti et al. 2009). In the last decade, this source was observed in a vast variety of spectral appearances, ranging from Compton thick (Risaliti et al. 2005) to an almost unobscured condition more reminiscent of a pure type 1 AGN (Walton et al. 2014).

Absorbers at higher ionization (the so-called warm absorbers, WA) imprint discrete absorption lines on $\sim$50% of type 1 AGN spectra (Crenshaw et al. 2003b). These features, which fall mainly in the soft X-ray (e.g., from Ne II–Ne X, Fe X–Fe XXIV, and O IV–O VII) and in the UV (e.g., O VI, Mg II, C II–C IV, and Si II–Si IV) domain, are usually blueshifted with respect to the systemic velocity, therefore indicating a global outflow of the absorbing gas (Crenshaw et al. 2003b). In local Seyfert 1 galaxies, absorption lines usually have a narrow profile (*FWHM*$\sim 10^2$ km s^{-1}). In about 15% of optically selected quasars (Weymann et al. 1991), broad absorption lines (BAL) with a typical width of 10^4 km s^{-1} have also been observed (Hamann & Sabra 2004). In the last ten years, observational campaigns providing simultaneous high resolution UV and X-ray spectroscopy have been performed for a handful of local AGN (see Costantini 2010, for a review). In some cases (e.g., NGC 4151, Kraemer et al. 2005 Mrk 279, Arav et al. 2007, Costantini et al. 2007 1H 0419-577 Di Gesu et al. 2013), it has been established that X-ray and UV narrow absorption lines (NAL) may be the manifestation of the same outflow, even though it is not trivial to determine how the X-ray and UV absorbing gas are physically and geometrically related. The UV and X-ray absorbing gas could be colocated (e.g., Mrk 509, Ebrero et al. 2011), and the UV absorbing components could be denser clumps embedded in a more highly ionized wind (e.g., NGC 4051, Kraemer et al. 2012). The WAs are usually complex multicomponent winds spanning a broad range in velocity and in ionization. The lower ionization components produce the UV lines, while the higher ionization phases are only seen in the

X-rays. An intermediate phase producing absorption lines in both bands may in some cases be present.

Variability in the warm absorption may in principle contribute to the overall X-ray variability of AGN on different timescales. To assess the WA variability on long (e.g., ∼years) timescales it is necessary that high quality multiepoch spectroscopy is available, which is seldom the case. A multiepoch study of the WA was attempted, for instance, in Mrk 279 (Ebrero et al. 2010) without finding significant variability. In a different case (Mrk 841, Longinotti et al. 2010), comparing two different observations taken ∼4 years apart, a moderate decrease in the WA ionization as the continuum dims was observed. An even more noticeable long-term WA variability was reported in the case of Mrk 335 (Longinotti et al. 2013), where the emergence of an ionized outflow that was not historically present was observed in 2009. On shorter timescales, changes in the WA opacity or ionization were observed for instance in NGC 3783 (∼31 days, Krongold et al. 2005) and NGC 4051 (few ks–few months, Krongold et al. 2007, Steenbrugge et al. 2009).

The timescale over which absorption lines are observed to vary can be used to measure the distance of the absorbing gas from the ionizing source (see Crenshaw et al. 2003b). Indeed, for photoionized gas in equilibrium, the recombination timescale depends on the gas number density n. Besides the distance r, the gas density is the only other unknown parameter in the definition of ionization parameter $\xi = L_{\mathrm{ion}}/n r^2$ (where L_{ion} is the ionizing luminosity in the 1–1000 Ryd band). Searching for absorption line variability on short timescales and thus constraining the location of the WA is the main motivation for conducting monitoring campaigns of AGN (e.g., Mrk 509, see Kaastra et al. 2012). The knowledge of the location is crucial to estimate the mass outflow rates and kinetic luminosities associated with these absorbers (e.g., Crenshaw & Kraemer 2012), and thus, to evaluate their potential impact on the host galaxy environment.

With this aim, during the summer of 2013 and the winter of 2013-14 we performed a large multiwavelength monitoring campaign on the bright Seyfert 1 NGC 5548. The overview of the campaign is presented in Mehdipour et al. (2015, hereafter Paper I). NGC 5548 is a prototypical Seyfert 1 galaxy, which has been studied for decades from optical (e.g., Peterson & Wandel 1999) to X-ray wavelengths (e.g., Nandra et al. 1993, Iwasawa et al. 1999). From a dynamical modeling of the BLR (Pancoast et al. 2014), it is inferred that this source is observed at an inclination angle of ∼ 30° and hosts a supermassive black hole (SMBH) of ∼ 3×10^7 M$_\odot$ in its center. Previously, high resolution UV (Crenshaw & Kraemer 1999, Crenshaw et al. 2003a) and X-ray (Kaastra et al. 2000, 2002, Steenbrugge et al. 2003, 2005) spectra have revealed several deep NAL that can be ascribed to a moderate velocity (v_{out}=200–1200 km s^{-1}) ionized outflow.

Unexpectedly, throughout the whole 2013-14 campaign, NGC 5548 appeared dramatically different than it appeared in the past (e.g., from the *Chandra* observation of 2002, Steenbrugge et al. 2005): the object was ∼25 times less luminous in the soft X-rays. Moreover, NGC 5548 showed broad, asymmetric absorption troughs in the blue wings of the main UV broad emission lines (e.g., in Ly α, C IV, N V). In Kaastra et al. (2014, hereafter K14), we proposed that all these changes can be ascribed to the onset of a persistent, weakly ionized, fast (v∼5000 km s^{-1}), wind (hereafter "the obscurer"). The obscurer is
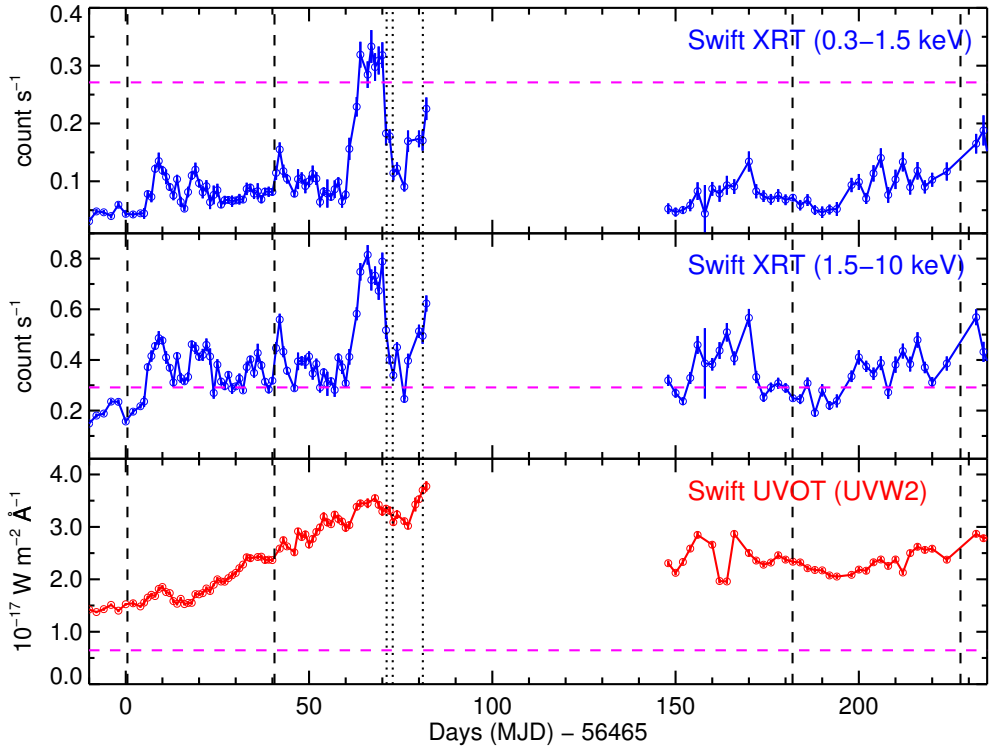
Figure 3.1: From top to bottom panel: the observed light curves of NGC 5548 in two X-ray bands and in the UV (λ=2030 Å). These curves are obtained from the daily Swift monitoring performed during our campaign. In each panel, the pink horizontal dashed line marks the flux level measured by Swift at unobscured epochs (2005 and 2007). From left to right, vertical lines indicate first and last XMM-*Newton* observation of summer 2013 (dashed lines), the three *Chandra* observations of September 2013 (dotted lines), and the last two observations of the XMM-*Newton* program (in December 2013 and February 2014, dashed lines).

located within or just outside the BLR, at a distance of a few light days from the SMBH, and may have been launched from the accretion disk. It blocks ~90% of the X-ray flux along our line of sight, thereby lowering the ionizing luminosity received by the WA. Indeed, in this obscured condition, the historical NGC 5548 WA is still present, but with a lower ionization. In the X-rays, the WA is consistent with being ~3 times less ionized than what was observed in 2002 (K14), and, at the same time, in the UV it shows new lower-ionization NAL (from, e.g., C II and C III, Arav et al. 2015).

In this paper, we use all the high resolution X-ray spectra collected during our campaign to assess what drives the spectral changes of NGC 5548 on timescales as short as few days. This is the typical time separation between the X-ray observations of the campaign. These spectra are suitable to investigate the absorption variability because they cover the energy band where the main ionized and neutral absorption features of, e.g., oxygen and

iron, fall. During the campaign, the source was always weak in the soft X-rays, except for a sudden brightening in September 2013 (Fig. 3.1). On that occasion, we triggered a *Chandra*-LETGS observation. In the following, we also investigate the possible causes and consequences of this sudden brightening.

The paper is organized as follows: in Sect. 3.2 we briefly present the data sets that we use in this analysis, and in Sect. 3.3 we describe the template spectral model that we apply to all the data sets in Sect. 3.4. Finally in Sect. 3.5 we discuss our results, and in Sect. 3.6 we outline the conclusions.

The C-statistic (Cash 1979) is used throughout the paper, and errors are quoted at 68% confidence level ($\Delta C = 1.0$). In all the spectral models presented in the following, we use the Galactic hydrogen column density from Wakker et al. (2011, $N_{\mathrm{H}} = 1.45 \times 10^{20}$ cm^{-2}). The cosmological redshift that we adopted for NGC 5548 is 0.017175 (de Vaucouleurs et al. 1991).The cosmological parameters are set to: $H_0 = 70$ km s^{-1} Mpc^{-1}, $\Omega_{\mathrm{m}} = 0.3$ and $\Omega_{\Lambda} = 0.7$.

3.2   The data

The XMM-*Newton* observed NGC 5548 between June 2013 and February 2014 using both the EPIC cameras (Turner et al. 2001, Strüder et al. 2001) and the Reflection Grating Spectrometer (RGS, den Herder et al. 2001). The core of the campaign consisted of 12, ∼50 ks long, XMM-*Newton* observations that were taken every ∼ 2–8 days in June and July 2013. After these, two other observations were acquired in December 2013 and February 2014, providing 14 XMM-*Newton* data sets in total. The details of all the observations, which we hereafter label in chronological order as XM1–XM14, are given in Table 3.1. During the entire campaign, the source was also monitored daily by Swift (Gehrels et al. 2004), both in the X-rays with the X-Ray Telescope (XRT, Burrows et al. 2005) and in the UV with the UV Optical Telescope (UVOT, Roming et al. 2005). Swift-UVOT flux measurements in the UVW2 (λ=2030 Å) filter, corrected for reddening and for the host galaxy contribution as explained in Paper I, are also used in the present analysis.

In September 2013 we triggered a *Chandra* observation because Swift observed a sudden brightening (Fig. 3.1). The observation was performed with the Low Energy Transmission Grating Spectrometer (LETGS, Brinkman et al. 2000) in combination with the High Resolution Camera (HRC-S). The observing time was split into three observations (Obs. CH1–CH3) of 30, 67, and 123 ks. The first two were taken on September 1st and 2nd, while the third and longest observation was taken a week later on September 10th. Simultaneously with this observation a higher energy spectrum was acquired with the Nuclear Spectroscopic Telescope Array (NuSTAR, Harrison et al. 2013) satellite. In the occasion of this flaring event, no XMM-*Newton* observation was available.

A detailed description of the data reduction procedure for all the instruments is given in Paper I. In the present analysis, we fit the high resolution RGS and LETGS spectra. The simultaneous EPIC-pn and NuSTAR spectra at higher, less absorbed energies provide the continuum baseline over which the absorption is superposed. Ursini et al. (2015), hereafter U15, provide a detailed modeling of the continuum at high energies.

Table 3.1: List of XMM-*Newton* and *Chandra* data sets used for present analysis.

Obs.	Date yyyy-mm-dd	Satellites	F_{2030} [a] (10^{-14}erg s^{-1} cm^2 A^{-1})	$F_{0.3-2.0\,\mathrm{keV}}$ [b] (10^{-12}erg s^{-1} cm^2)	$F_{2.0-10.0\,\mathrm{keV}}$ [b]
XM1	2013-06-22	1 4	2.07	1.1	13.2
XM2	2013-06-30	1 4	2.28	3.5	29.9
XM3	2013-07-07	1 4	2.07	2.1	21.2
XM4	2013-07-11	1 4	2.32	3.6	32.1
XM5	2013-07-15	1 4	2.57	2.6	26.9
XM6	2013-07-19	1 4	2.74	2.3	27.4
XM7	2013-07-21	1 4	2.88	2.3	23.5
XM8	2013-07-23	1 4	3.09	2.2	25.1
XM9	2013-07-25	1 4	2.97	3.2	29.8
XM10	2013-07-27	1 4	3.29	3.0	29.4
XM11	2013-07-29	1 4	3.21	2.8	26.4
XM12	2013-07-31	1 4	3.21	2.2	23.6
CH1	2013-09-01	2 4	4.54	7.7	38.7
CH2	2013-09-02	2 4	4.48	4.4	29.7
CH3	2013-09-10	2 3 4	4.89	5.7	36.1
XM13	2013-12-20	1 4	3.27	2.1	21.8
XM14	2014-02-05	1 4	3.49	4.1	24.4

Notes. Instruments are labeled with numbers, as followed: 1: XMM-*Newton*, 2: *Chandra*, 3: NUSTAR, and 4: Swift. [a] UV flux measured by Swift-UVOT, corrected for reddening. [b] Observed flux in the quoted bands, as derived from our best-fit model.

As in K14, we fitted the EPIC-pn in the 1.03–10.0 Å ($\simeq$1.24–12 keV) band together with the RGS in the 5.68–38.23 Å ($\simeq$0.32–2.2 keV) band. Thus, the two instruments overlap in a small band allowing us to check for possible intercalibration mismatches. In all our fits, the intercalibration factor used in K14 ($\sim$ 1.027) was adequate. Because of an incomplete correction for the gain of the EPIC-pn (not corrected in the SAS v13 we used, see Paper I), the Fe Kα line appears blueshifted (see Cappi et al. in prep. for a detailed discussion), which we correct for with an artificial redshift for these spectra. However, this solution leads to a poor fit near the energy of the gold M-edge of the telescope mirror. For this reason, we omitted the interval 5.0–6.2 Å ($\simeq$2.0–2.5 keV) from all our fits.

We fitted the *Chandra*-LETGS spectra between 2 and 40 Å ($\simeq$0.3–6.2 keV). We used the NuSTAR spectrum simultaneous to CH3 in the 0.2–2.5 Å ($\simeq$5–60 keV) band. Since *Chandra*-LETGS and NuSTAR were consistent in the overlapping band, we did not apply any intercalibration correction in the joint fit.

3.3   The template model

To assess the variability of NGC 5548, we used the same template model to fit all the spectra. This template is close to the model adopted in K14, differing from it only in the modeling of the "soft-excess" (Arnaud et al. 1985) component. We performed all the spectral analysis with the latest version of SPEX (v. 2.05, Kaastra et al. 1996). In our template model, we considered the cosmological redshift and the Galactic absorption. For the latter, we use a collisionally ionized plasma model (HOT), with a nominal temperature of 0.5 eV for a neutral gas.

Our continuum model includes a primary and reflected power law, on top of which lies a soft-excess component. In NGC 5548 the reflection is consistent with being constant (see U15), thus producing a steady narrow Fe Kα line (see Cappi et al., in prep.). In the present analysis we used the reflection parameters obtained in U15, i.e., Γ=1.9 and $E_{\rm cut}$=300 keV for the photon index and the high energy cutoff of the primary power law, in the SPEX reflection model REFL. This model includes both a Compton reflected continuum (Magdziarz & Zdziarski 1995) and the Fe Kα line (Zycki & Czerny 1994). To adjust the fit of the Fe Kα line, we allowed the normalization of REFL to be free to vary within the errors of the U15 model. When using EPIC-pn data, we applied to REFL an artificial blueshift (z=-1.25×10^{-2}) to correct for an apparent centroid shift of the Fe Kα line (see also Sect. 3.2).

The X-ray obscuration affects the spectrum mainly below 2.0 keV and therefore makes the detection of the soft excess from X-ray spectra elusive. Nevertheless, this component contributes to the continuum in the band where most of the absorption is seen, thus its modeling is critical for evaluating the absorption variability. In Paper I we show that the soft-excess component is likely to be the tail of a component extending from UV to soft X-rays, which is produced by Compton up-scattering of the disk photons in a warm, optically thick plasma. Therefore, in this framework, the UV emission (which is not affected by the obscuration) is a proxy for the X-ray soft excess. We used COMT (based on Titarchuk 1994) to model the soft-excess component and we used the UV flux (F_{2030}) listed in Table 3.1 for each observation to set the normalization. The 0.3–2.0 keV luminosity of the soft-excess is given by: ($L_{0.3-2.0\,\rm keV}^{\rm COMT}/10^{34}$W)$= 2.093 + 2.893 \times (F_{2030}/10^{-34}$Jy), valid for the range of observed UV fluxes used here (Mehdipour, private communication). Hence, consistent with the long-term variability analysis in Mehdipour et al. (in prep.), we kept the COMT component constant in shape in all the fits, with its 0.3-2.0 keV flux varying according to the UV flux. We use the mean values given in Paper I for the other COMT parameters, namely the Wien temperature of the incoming photons ($T_0 = 0.8$ eV), the temperature ($T_1 = 0.17$ keV), and the optical depth ($\tau = 21$) of the plasma.

A detailed modeling of the X-ray emission features of NGC 5548 will be presented in Whewell et al, in preparation. The X-ray narrow emission lines are consistent with being constant during the XMM-*Newton* campaign, and thus could be kept frozen in all our fits. For the narrow lines, we obtained the values in the K14 fit, while for the broad emission features we used the fluxes given in Steenbrugge et al. (2005).

In K14, we found that the obscurer causing the persistent flux dimming of NGC 5548 comprises two ionization phases (hereafter labeled as "warm" and "cold"). The warm phase is mildly

ionized ($\log\xi = -1.25$) and has a larger covering fraction (e.g., $C_{V,warm} \sim 86\%$, $C_{V,cold} \sim 30\%$, K14) and a lower column density (e.g., $N_{H,warm} \sim 10^{22}$ cm^{-2}, $N_{H,cold} \sim 10^{23}$ cm^{-2}, K14) than the cold phase, which is consistent with being neutral. In SPEX, we used a photoionized absorber model (XABS) for both the obscurer components and we adopted for them the same kinematics (outflow and broadening velocity) used in K14. The ionization balance for both the obscurer components is computed using the intrinsic, unabsorbed spectral energy distribution (SED).

Finally, we included six more XABS components in the template model to account for the lower ionized counterpart of the historical NGC 5548 warm absorber. The ionization balance for all the WA components is computed using a SED filtered by the obscurer. We label the WA components with capital letters, from A to F as the ionization increases. As in K14, we assumed that the WA varies only in ionization when the ionizing SED illuminating it changes. Indeed, from UV spectra we know that the kinematics of the WA components has not changed over at least 16 years, and Ebrero et al. (in prep.) shows no historical evidence for total hydrogen column density variations. We kept therefore the kinematics and the equivalent hydrogen column density of all the WA components frozen to the parameters obtained from the unobscured 2002 spectrum (see the updated fit in Ebrero et al., in prep.).

In the following, we apply this template model to all the XMM-*Newton* and *Chandra* data sets of our monitoring campaign. In all the fits, the free parameters are the slope and the normalization of the primary power law, column density, and covering fraction of the two obscurer phases. Besides these, in the fits of those data sets in which either the continuum or the obscurer parameters change significantly, we also allow the ionization parameters of the warm absorber to vary. The variability in flux of the soft excess component was determined directly from the Swift UV flux, as explained above.

3.4 Fitting the variability

3.4.1 The core of the campaign: from June to August 2013

The XMM-*Newton* monitoring campaign began on June 22nd, catching NGC 5548 at the lowest flux level observed in any of the high resolution spectra of the campaign ($F_{0.3-2.0\,keV} \sim 1.1 \times 10^{-12}$ erg s^{-1} cm^2, for Obs. XM1, see Table 3.1). Throughout all the summer of 2013, (Obs. XM2–XM12) the 0.3–2.0 keV flux remained quite stable (within a factor ~ 1.3) around an average level of $\sim 2.7 \times 10^{-12}$ erg s^{-1} cm^2. The stacked XMM-*Newton* spectrum of Obs. XM1–XM12 is published in K14. In that paper, we consistently determine both the average obscurer parameters and the average obscured SED illuminating the WA. Accordingly, we compute the ionization balance and the ionization parameters for all the WA components.

We fitted Obs. XM1–XM12 assuming the average WA determined in K14. Hence, only the continuum and the two obscurer phases were left free in the fits. Furthermore, we set a lower limit for the continuum slope ($\Gamma \geq 1.5$) in the fits to be consistent with what was observed during the campaign at higher energies and with the analysis repeated by Cappi
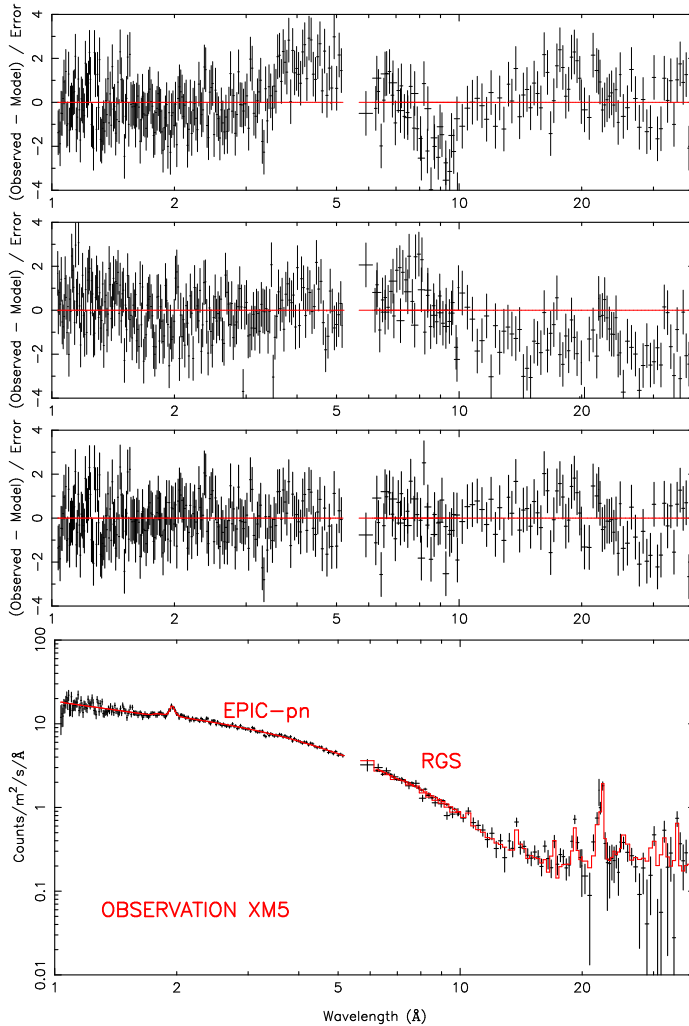
Figure 3.2: Examples of fits the XMM-*Newton* spectrum of Obs. XM5. From top to bottom panel: fit residuals when only the obscurers covering fractions are allowed to vary from the values obtained for the average spectrum; fit residuals when only the obscurers column densities are allowed to vary from the values obtained for the average spectrum; fit residuals of the best-fit model where both column densities and covering fractions are permitted to vary freely; spectrum of observation XM5. The solid line represents the best-fit model. We rebinned the data for clarity.

et al, in preparation. Indeed, when fitting this absorbed spectra below ∼10 keV, a flatter intrinsic continuum becomes degenerate with a stronger obscuration. The assumption on the slope aimed at minimizing this ambiguity, however, did not affect the final results (as we checked *a posteriori*, see below).

As a first step we fit the spectra, allowing for both the obscurer phases with just one of the parameters (column density, and covering factor) free. When only the covering fractions are allowed to vary, the fit displays strong residuals, for instance, the negative residuals just below ∼10 Å (See Fig. 3.2, first panel). In the observation where they are more evident (Obs. XM5) the C-statistic is 600 for an expected value of 340. When we fixed the covering factors but instead allowed the column densities to vary, more systematic residuals be-

Table 3.2: Best-fit parameters and errors, for the individual XMM-*Newton* and Chandra observations. In the last row, we list also the parameters derived in K14 for the average XM1–12 spectrum for comparison.

Obs	Γ [c]	Obscurer components [a]				WA components [b]						C/Expected C[g]
		$N_{\rm H,warm}$ [d] $(10^{22}\,{\rm cm}^{-2})$	$C_{\rm V,warm}$ [e]	$N_{\rm H,cold}$ [d] $(10^{22}\,{\rm cm}^{-2})$	$C_{\rm V,cold}$ [e]	$\xi_{\rm A}$ [f]	$\xi_{\rm B}$ [f]	$\xi_{\rm C}$ [f]	$\xi_{\rm D}$ [f]	$\xi_{\rm E}$ [f]	$\xi_{\rm F}$ [f] (log erg cm s^{-1})	
XM1	1.5 **	1.7 ± 0.1	0.86 ± 0.01	12 ± 1	0.47 ± 0.02							384/334
XM2	1.58 ± 0.03	1.04 ± 0.04	0.927 ± 0.005	10 ± 2	0.170 ± 0.03							422/345
XM3	1.5 **	1.42 ± 0.06	0.909 ± 0.005	11 ± 3	0.18 ± 0.02							379/337
XM4	1.60 ± 0.03	1.17 ± 0.04	0.922 ± 0.004	14 ± 2	0.19 ± 0.03							406/346
XM5	1.57 ± 0.03	1.44 ± 0.05	0.915 ± 0.004	8 ± 1	0.24 ± 0.03							435/335
XM6	1.5 **	1.4 ± 0.1	0.916 ± 0.005	5 ± 1	0.30 ± 0.08	0.33*	1.06*	1.70*	1.91*	2.48*	2.67*	415/341
XM7	1.5 **	1.40 ± 0.05	0.909 ± 0.005	12 ± 2	0.27 ± 0.03							394/340
XM8	1.53 ± 0.03	1.62 ± 0.07	0.88 ± 0.05	9 ± 1	0.35 ± 0.03							389/339
XM9	1.64 ± 0.03	1.58 ± 0.05	0.896 ± 0.004	11 ± 2	0.24 ± 0.03							390/340
XM10	1.57 ± 0.03	1.43 ± 0.05	0.911 ± 0.004	9 ± 1	0.24 ± 0.03							434/344
XM11	1.56 ± 0.03	1.46 ± 0.05	0.902 ± 0.004	10 ± 2	0.23 ± 0.03							399/340
XM12	1.5 **	1.43 ± 0.04	0.922 ± 0.005	12 ± 2	0.27 ± 0.03							447/338
CH1	1.83 *	1.7 ± 0.2	0.74 ± 0.03	17 *	≤ 0.23	0.38 *	1.11 *	1.75 *	1.96 *	2.53 *	2.72 *	149/152
CH2+3	1.83 ± 0.02	1.49 ± 0.08	0.79 ± 0.07	17 ± 3	0.35 ± 0.03	0.38	1.11	1.75	1.96	2.53	2.72	530/311
XM13	1.5 **	1.7 ± 0.1	0.87 ± 0.02	9 ± 2	0.33 ± 0.03	0.33*	1.06 *	1.70*	1.91*	2.48 *	2.67*	415/340
XM14	1.59 ± 0.01	1.22 ± 0.03	0.917 ± 0.003	10*	≤ 0.003	0.39	1.12	1.76	1.97	2.54	2.73	485/342
K14 ***	1.566 ± 0.009	1.21 ± 0.03	0.86 ± 0.02	9.6 ± 0.5	0.30 ± 0.10	0.33	1.06	1.70	1.91	2.48	2.67	

Notes. [a] For the warm obscurer: $\log\xi = -1.25$. For the cold obscurer: $\log\xi = -4$ [b] For Obs. CH2+3, XM14, and K14, the ionization parameters given the output of the iterative fitting procedure described in Sect. 3.4.2. [c] Photon index of the primary continuum. [d] Column density of the obscurer components. [e] Covering fraction of the obscurer components. [f] Ionization parameters of the warm absorber components. [g] C-statistics of the final best-fit model. (*) Frozen parameters. (**) Lower limit of the fitting range. (***) Best-fit parameters derived in K14 for the coadded XM1–12 spectrum.

tween 10 and 20 A are apparent (Fig. 3.2, second panel). Therefore, we conclude that the two phases of the obscurer have to be variable both in column density and the covering fraction to adapt the template model to all the individual XMM-*Newton* observations. We tested however the possibility that the obscurer varies in ionization rather than in covering fraction. For most of the data sets, a statistically acceptable fit can be achieved keeping the covering fraction of both the obscurer phases frozen to the average values derived in K14, and allowing the ionization parameter of the warm obscurer to vary instead. However, with these constraints the best fit prefers an almost neutral obscurer (e.g., $\log\xi \leq -3.5$), which would be too lowly ionized to produce, for instance, the broad C IV absorption lines that are seen in the UV. Hence, we discarded these fits.

The final best-fit parameters are listed in Table 3.2. In a couple of cases, the fit stopped at the lower limit we had imposed for Γ. We checked how much further the fit of these data sets could be improved allowing an even flatter continuum. In all cases, releasing the spectral index resulted in a negligible improvement of the fit (e.g., for Obs. XM1, $\Delta C = -1$ for $\Gamma = 1.46$).

The RGS spectra of the individual observations are rather noisy and the residuals do not

show any hint of unaccounted WA features. However, as a final test, we checked how sensitive are the best fits to possible variations in the WA ionization. We attempted to refit each observation setting the WA ionization parameters according to the variation from the average of the continuum normalization. All the fits were insensitive to this variation, (e.g., $\Delta C \sim -1$) with the free parameters remaining the same within the errors. Therefore, we concluded *a posteriori* that assuming a constant WA in the core of the XMM-*Newton* campaign was reasonable. We show in Fig. 3.2 (third and fourth panel) an example of best fit (Obs. XM5).

3.4.2 The flare of September 2013 as seen with *Chandra*-LETGS and NuSTAR

In September 2013 we triggered a series of 3 *Chandra*-LETGS observations because it seemed that NGC 5548 was recovering from the obscuration. Indeed, in a few days, the X-ray flux in both the Swift-XRT bands rose above the level measured at unobscured epochs and remained steady for about a week. This brightening was however a short-lived flare, and after a few days the source fell again to the typical low flux level of the XMM-*Newton* campaign (Fig. 3.1). Our triggered *Chandra*-LETGS observations missed the peak of the flare. The first two observations were taken during its declining tail, while a week later the third one caught a smaller rebrightening.

To understand if and how the absorbing components had responded to these continuum changes we needed to use in the photoionization modeling of the obscurer a SED representative of NGC 5548 during the flare (Fig. 3.3, solid line). To construct it, we used the Comptonization model of Paper I, which extends from the UV to the soft X-rays. At the same time, NuSTAR provided the continuum slope at high energies. In the UV, we took the model values corresponding to $\lambda = 2987$ Å, $\lambda = 1493$ Å $\lambda = 909$ Å. We then interpolated 20 data points in the model between 0.03 and 100 keV. Finally, we cut off the SED at low energies (below 0.01 Ryd).

We consistently derived the obscurer parameters and the WA ionization parameters using the same iterative method of K14. At each iteration of this fitting routine new obscurer parameters are fitted. Next, the new obscured continuum is used as the ionizing SED in the photoionization modeling of the six WA components. The new ionization parameters are assigned by rescaling those observed in the unobscured spectrum of 2002 to the level of the current obscured continuum. Explicitly, the ionization parameters at the N_{th} iteration are given by: $\xi_N / \xi_{2002} \sim L_{\text{ion,N}} / L_{\text{ion,2002}}$. Finally, the ionization balances for the new ionization parameters are recomputed before moving to the next iteration. The final outputs of this procedure are the obscurer parameters, the obscured SED illuminating the WA, and the rescaled WA ionization parameters.

At first, we dealt with the third and longest *Chandra*-LETGS spectrum (Obs. CH3) and we fitted it jointly with the simultaneous NuSTAR spectrum. We started with a few iterations where only the continuum was allowed to vary. However, since in this way the fit was left with large residuals (C/Expected C=846/307, Fig. 3.4, first panel), we released first the covering fractions (Fig. 3.4, second panel) and in turn the column densities of both the
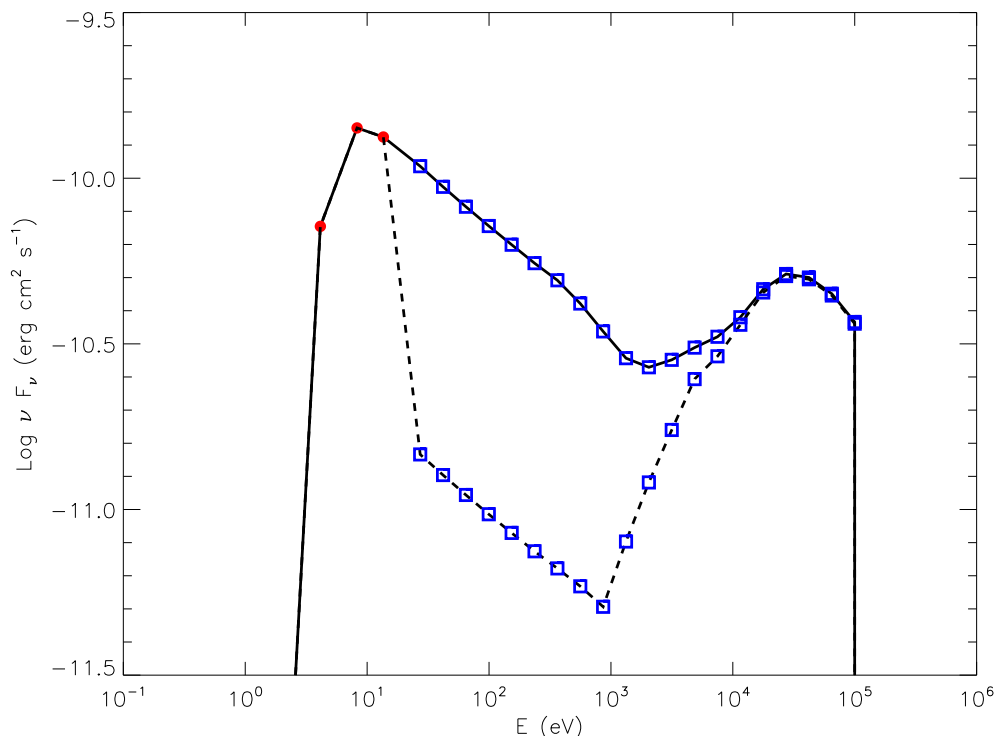
Figure 3.3: The unobscured (solid line) and obscured (dashed line) spectral energy distributions for NGC 5548 during the September 2013 flare, which were used for the photoionization modeling of the absorbers. The three data points in the UV (filled circles) are taken from the Comptonization model of Paper I. The data points from the EUV to hard X-rays (open squares) are also interpolated from the X-ray continuum model. See Sect. 3.4.1 for details.

obscurer phases (Fig. 3.4, third panel). Once we achieved the best fit, we applied it to the other two *Chandra*-LETGS spectra, for comparison. For obs. CH1, the fit tends to steepen the continuum up to $\Gamma \sim 2.2$. In contrast, we could easily fit Obs. CH2 just by renormalizing the model. Therefore we decided that we can stack observations CH2 and CH3, and thus increase the signal-to-noise ratio of the spectrum.

We fitted this stacked spectrum (hereafter labeled as Obs. CH2+3) together with NuSTAR using the iterative procedure just described. The final best-fit model is shown in Fig. 3.4 (fourth panel) and the final obscured SED produced in the iterative fitting is plotted in Fig. 3.3 with a dashed line. Using the above best fit, we tested whether the difference in photon index for observation CH1 could be due to changing properties of the obscurer. If we keep the continuum shape frozen, the best fit prefers zero covering fraction for the cold obscurer. For this data set, we favor this solution because a large variation of the continuum slope would be inconsistent with what NuSTAR and INTEGRAL have shown for the whole campaign (see U15).

Figure 3.4: Examples of fit for the *Chandra*-LETGS plus NuSTAR spectrum of NGC 5548 during the September 2013 flare. From top to bottom panel: fit residuals when only the continuum is allowed to vary from the values obtained for the average spectrum; fit residuals when only the obscurers covering fraction is allowed to vary from the values obtained for the average spectrum; fit residuals for the final best-fit model. The solid line represents the best-fit model. We rebinned the data for clarity.
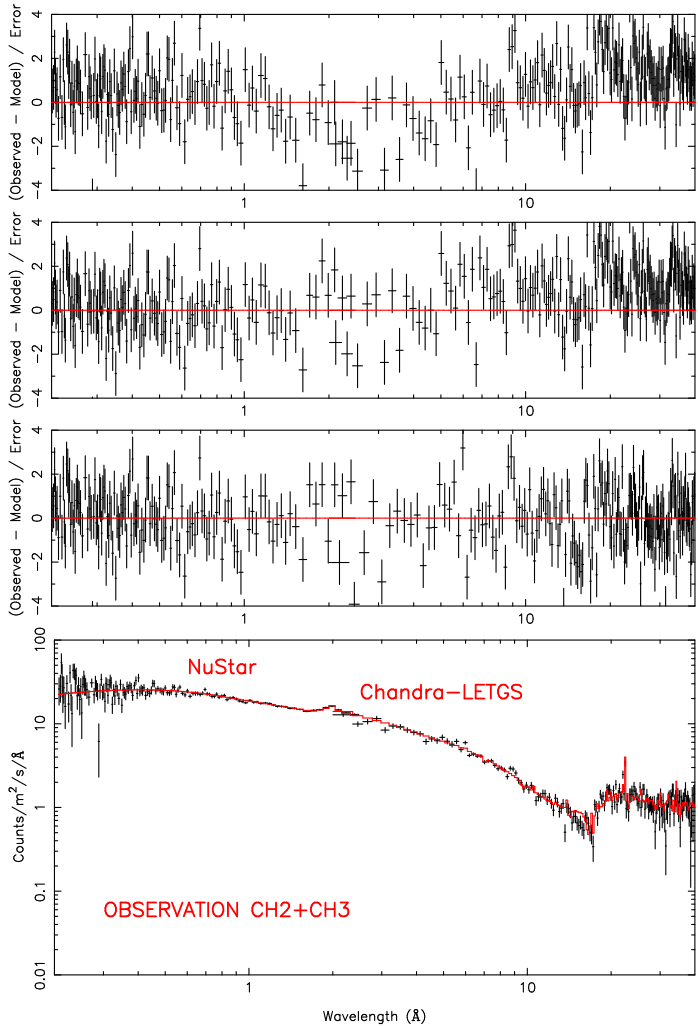
All the best-fit parameters for the *Chandra* observations are shown in Table 3.2. Compared to the spectra of the core of the campaign, the *Chandra* spectra require both a steeper continuum ($\Gamma \sim 1.8$) and a lower covering fraction of the warm obscurer ($C_{V, warm} \sim 0.8$). However, in principle, it is possible that a change in the ionization state of the obscurer mimics a drop in the covering fraction. The data quality is not sufficient to fit the ionization parameter, therefore we refitted the spectrum with the ionization parameter of the warm obscurer expected if it responds immediately to flux changes. We used the UVW2 flux to calculate the expected increase in ionization parameter. In the fi,t we used the covering fractions as given in K14. With these constraints, the resulting fit is statistically worse (C/Expected C=647/311) and shows larger positive residuals in the *Chandra*-LETGS band.
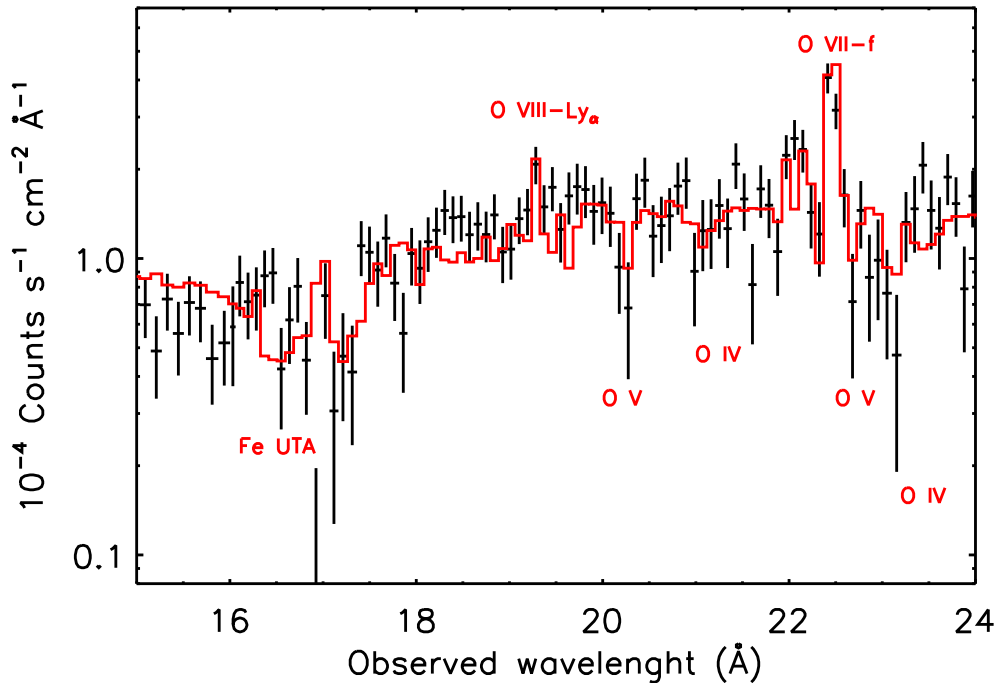
Figure 3.5: The *Chandra*-LETGS spectrum of NGC 5548 in the 15–24 Å wavelength region. The solid line represents our best-fit model. The most prominent emission and absorption features are labeled. The spectrum shows some WA signatures (Fe-UTA, O IV–O V) that were not detected during the XMM-*Newton* campaign.

We derive a better fit by leaving the ionization parameter of the warm obscurer free, but the obtained ionization parameter ($\log \xi \sim 0.9$) is unrealistically high ($\sim$100 times than the average value) considering the increase by only a factor 2 in the UVW2 flux during the flare. Therefore, we can exclude that a change in the ionization of the obscurer is the dominant cause of the observed flare.

During the XMM-*Newton* campaign, the discrete features of the WA are always blended with the obscured continuum and not detectable. During the *Chandra* observation the source was about twice as bright, and some WA signatures are visible in the stacked CH2+3 spectrum (Fig. 3.5). These features are consistent with the WA model computed via our iterative procedure. The broad trough at $\sim$ 16 Å is a blend of unresolved transition array (UTA) from several ionized iron species. Between 20 and 24 Å, some O IV-O V absorption lines are present. In Table 3.3, we list which of the O IV and O V lines predicted by our WA model contribute to each feature. The WA comprises six ionization components that could be distinguished thanks to the excellent data quality of the 2002 spectrum. Here, the lower statistics does not allow us to overcome the blending among the components.

Table 3.3: List of the O IV and O V lines predicted by our WA model that contributes to the features visible in Fig. 3.5.

Ion	WA component	Outflow velocity km s^{-1}	λ_{obs} ^{a} Å	τ ^{b}
O V	C	1148	20.23	27
	B	547	20.27	7
	D	254	20.29	3
	E	792	20.26	1
O IV	B	547	21.04	3
	C	1148	21.00	2
O V	C	1148	22.67	143
	B	547	22.71	34
	D	254	22.73	16
O IV	C	1148	23.04	10
	B	547	22.08	5

Notes. $^{(a)}$ Predicted wavelength, considering the cosmological redshift and the blueshift due to the outflow. $^{(b)}$ Line optical depth.

3.4.3 The end of the campaign: the observations of December 2013 and February 2014

In the last two XMM-*Newton* observations of the campaign, NGC 5548 was again at the same flux level of summer 2013. Therefore, at first we attempted to fit them again using the same WA of the average spectrum. The parameters of the continuum and of the two phases of the obscurer were free. This attempt resulted in a satisfactory fit for XM13, while for Obs. XM14, we obtained a high column density for the cold obscurer ($N_{\mathrm{H,cold}} \sim 7 \times 10^{23}$ cm^{-2}) largely inconsistent with what was observed throughout the campaign. Thus, we attempted to refit this data set freezing the cold column density to the average value measured in the previous observations. This resulted in negligible covering fraction for the cold obscurer ($C_{\mathrm{V,cold}} \lesssim 10^{-2}$) and in a flatter continuum ($\Gamma \sim 1.6$ instead of ~ 1.7). This lower value of Γ is also similar to the other values measured at this luminosity (Fig. 3.8). For these reasons, we considered this solution more physically plausible. For this data set, a solution with a negligible covering fraction of the cold obscurer and a flatter continuum is also found in U15 when including in the fit INTEGRAL data at higher energies.

Considering the large change in the obscurer, also for this observation, we used our iterative method to determine the ionization of the WA (for details see Sect. 3.4.1). We built the SED for Obs. XM14 interpolating the Comptonization model of Paper I repeating all the steps already described in Sect. 3.4.1. In this case, the slope of the continuum at X-ray energies is provided by the fit of the EPIC-pn data. Starting from the solution just described, the fit converged in a few iterations. We also made some iterations where the ionization parameter of the warm obscurer was left free. However, since it was not possible to constrain it, we finally kept it frozen to the value found in K14 (see Sect. 3.3).
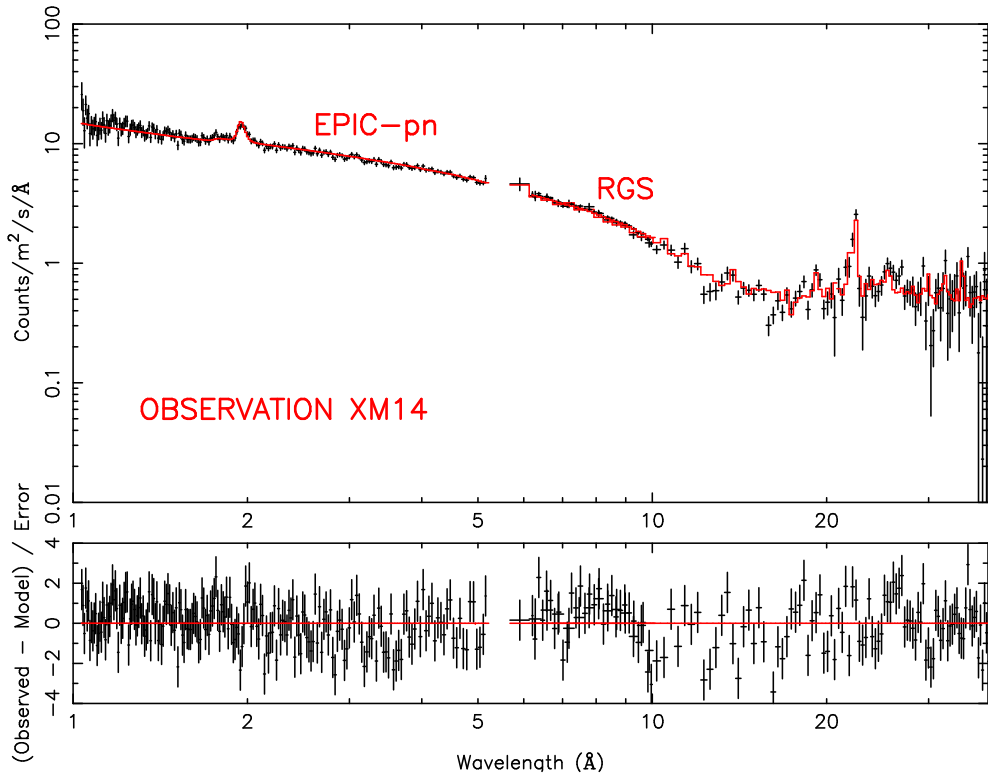
Figure 3.6: XMM-*Newton* spectrum and model residuals for Obs. 14. The solid line represents our best-fit model. We rebinned the data for clarity.

We adopt the final result of the iterative routine as our best-fit model. The parameters resulting from this exercise are outlined in Table 3.2.

We show the final best-fit model for Obs. XM14 in Fig. 3.6. The final WA model that we found is only slightly different from the average model. The residuals of the best-fit model display some possible features at ~10.3 Å and ~12.3 Å, which are close to the expected wavelength of the Ne IX-K edge (10.54 Å) and Ne X-Lyα (12.34 Å), respectively. We checked whether adding additional absorbing column density in Ne IX-Ne X could improve the fit. For this, we used the SLAB model in SPEX, which allows us to fit a single ionic column density regardless of the ionization balance with the other ions. We found however that this additional component is not required by the fit ($\Delta C = -1$).

3.5   Discussion

3.5.1   The short-term variability

During our extensive monitoring campaign in 2013 and early 2014, NGC 5548 was always obscured. In this analysis we applied the model developed in K14 for the average spectrum of the core of the campaign to all the individual observations, with the aim of understanding how the source varies. When both the intrinsic continuum and the obscurer are allowed to vary, the model is able to explain the variability on the two days to eight-month timescale sampled in the monitoring campaign. The obscuring material that is causing the soft X-ray flux depression of NGC 5548 varies along our line of sight, both in column density and in covering fraction. The scenario proposed by K14, that the source is obscured by a patchy wind, is consistent with our variability findings. In this framework, the variability of the obscuration may well be due to several reasons, e.g., motion across the line of sight and changing ionization with continuum variability.

The best-fit parameters for the continuum and the two phases of the obscurer are shown in Fig.3.7 as a function of time. During the core of the XMM-*Newton* campaign (Obs. XM1–XM12) the source was steadily obscured and the variability in flux was relatively small ($\sim 27\%$). The only clear outlier with a flux significantly different from the average is Obs. XM1. The values we found for the warm obscurer parameters (Fig. 3.7 4th and 6th panel) deviate from those found in K14, the coadded XM1–XM12 spectrum. This is because we used a different method to model the soft excess, which dominates the continuum in the band where the absorption from this component is more effective. In our modeling, the Comptonized soft-excess, whose normalization is set by the UV flux measured by Swift for each observation, is always more luminous ($L_{0.3-2.0\,\mathrm{keV}}^{\mathrm{COMT}} = [0.8-1.4] \times 10^{43}$ erg s^{-1}) than the phenomenological blackbody fitted in K14. Throughout the core of the campaign, the intrinsic continuum is fairly constant in shape (with a standard deviation of the spectral index $\sigma_\Gamma \sim 3\%$) and slightly variable in normalization ($\sigma_{\mathrm{UVW2}} \sim 17\%$, $\sigma_{\mathrm{Norm}} \sim 24\%$ for the soft-excess and the power-law component, respectively). For the obscurer, the cold component was the most variable ($\sigma_{C_{\mathrm{V,cold}}} \sim 31\%$ and $\sigma_{N_{\mathrm{H,cold}}} \sim 23\%$). In contrast, for the warm component the covering fraction is stable ($\sigma_{C_{\mathrm{V,warm}}} \sim 2\%$) and the column density shows rather small variability ($\sigma_{N_{\mathrm{H,warm}}} \sim 13\%$). The large deviation from the average of the cold covering fraction suggests that the obscurer inhomogeneity, which is possibly dominated by the cold phase, may have caused most of the variability observed during this phase of the campaign.

We also presented the *Chandra*-LETGS data sets, which were acquired in September 2013, when NGC 5548 underwent a two-week brightening. With respect to the core of the campaign changes in both the continuum and the obscurer are required to fit these spectra. At the time of the *Chandra* observation, the UV flux measured by Swift, which in our interpretation is a tracer for the soft X-ray excess, was the highest of the whole campaign. At the same time, the continuum at hard X-ray energies increased in flux and became steeper. For both observations the warm obscurer component has a significantly lower covering fraction. In the first observation, the covering fraction of the cold component is

also lower. As pointed out in Sect. 3.4.2, a variation in the obscurer ionization alone is insufficient to explain the observed variation in spectral shape.

The decrease in covering fraction, in principle, can be due either to a local thin patch of the obscurer passing in our line of sight at the moment of the *Chandra* or to a geometrical change of the UV/soft X-ray continuum source behind the obscurer. The former possibility, although it cannot be excluded, would however require that the intrinsic continuum and the obscurer change properties in synchrony, which seems *ad hoc*. In the Comptonization model of Petrucci et al. (2013), the UV/soft X-ray spectrum is supposed to be produced via Comptonization of the UV disk photons in a "warm" ($T \sim 1$ keV) and moderately thick ($\tau \sim 10-20$) corona. A "hot" corona, with higher temperature (~ 100 keV) and smaller optical depth (~ 1), in turn Compton upscatters these UV/soft X-ray photons to hard X-ray energies. In this interpretation, an increase in physical size of the warm corona, while naturally augmenting both the UV and the soft X-ray flux, would also result in a drop of the observed obscurer covering fraction. Moreover, the increase in the UV/soft X-ray photon flux will more effectively cool the hot corona, hence producing a steeper hard X-ray spectrum, which is in agreement with the observation.

Because of increased soft X-ray flux in the *Chandra* observations, some discrete WA features (Fe UTA, O IV–O V) became evident in the spectrum. These are the only detectable WA signatures in any X-ray spectrum of our campaign. These features are best fitted by a WA, which has a significantly lower degree of ionization than observed in the unobscured 2002 spectrum. Like K14, for all the WA components we found best-fit ionization parameters, which are 0.40 dex lower than the 2002 values ($\log \xi_{A-E}^{2002} = 0.78, 1.51, 2.15, 2.36, 2.94,$ and 3.13). This means that the ionizing luminosity received by the WA decreased by a factor of ~ 4. Thus, our analysis confirms the K14 finding. The decrease in the WA ionization, which is also seen in the UV (Arav et al. 2015) is explained when the newly discovered obscurer is located between the nucleus and the WA. In this geometry, the obscurer shadows the central source and prevents most of the ionizing flux from reaching the warm absorber.

The absorbers in NGC 5548 changed again in the last observation of the campaign, namely Obs. XM14. We found that in this data set, the covering fraction of the cold obscurer became negligible. At the same time, the continuum above 2.0 keV is similar to what is observed throughout the XMM-*Newton* campaign, while the soft-excess component is only slightly higher. Thus, the most likely cause of the spectral changes observed in this data set is again the inhomogenity of the obscuration.

Variability in the continuum and obscurer parameters is also noticed in the U15 analysis of six XMM-*Newton* and one *Chandra* observations, which were acquired simultaneously with a higher energy observation. However, the parameters obtained fitting the EPIC-pn jointly with RGS as done here are not directly comparable with those obtained fitting the EPIC-pn jointly with NuSTAR and/or INTEGRAL, as done in U15. This is both because of cross-calibration issues between the instruments and of differences in the analysis. In particular, as noticed also in U15, RGS and EPIC-pn are mismatched in flux in the overlapping band as a function of energy (e.g., Detmers et al. 2009). On the other hand, NuSTAR spectra are systematically steeper than EPIC-pn spectra ($\Delta\Gamma \sim 0.1$ see Cappi et al.,
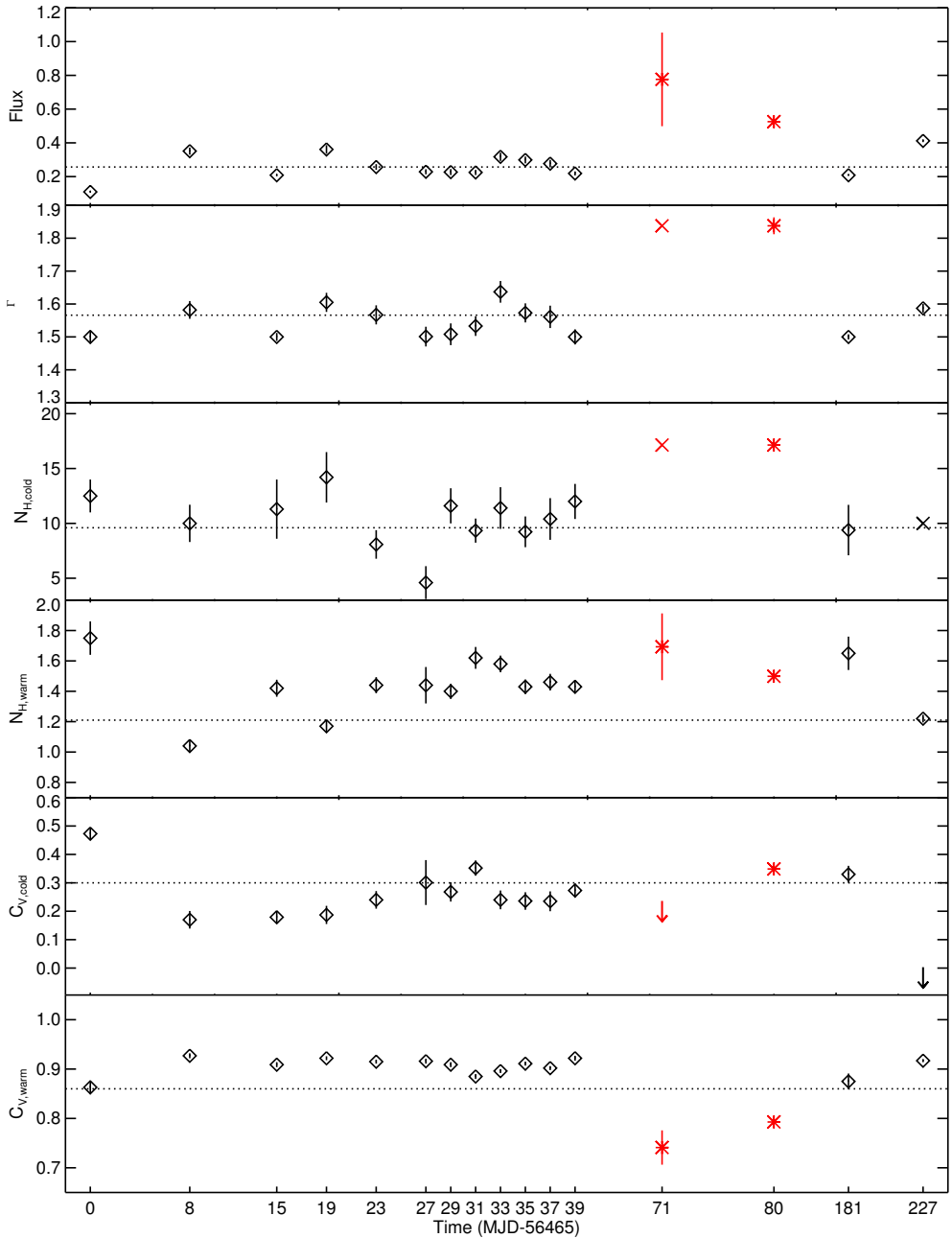
Figure 3.7: From top to bottom panel: observed flux in the 0.3–2.0 keV band, photon index of the primary continuum, column densities of the cold and the warm obscurer, and covering fractions of the cold and warm obscurer are shown as a function of time. The flux is plotted in units of 10^{-11} erg s^{-1} cm^2. The column densities are plotted in units of 10^{22} cm^{-2}. The Modified Julian Day (MJD) correspondent to each observation is labeled on the horizontal axes, which we shrunk for display purpose. Black diamonds and red asterisks identify parameters measured with XMM-*Newton* and Chandra-LETGS, respectively. Error bars, when larger than the size of the plotting symbol, are also shown. Upper limits are plotted as an arrow. Crosses represent values that were kept frozen in the fits. In each panel, the dotted horizontal line indicates the parameter value derived in K14 for the coadded XM1–12 spectrum.
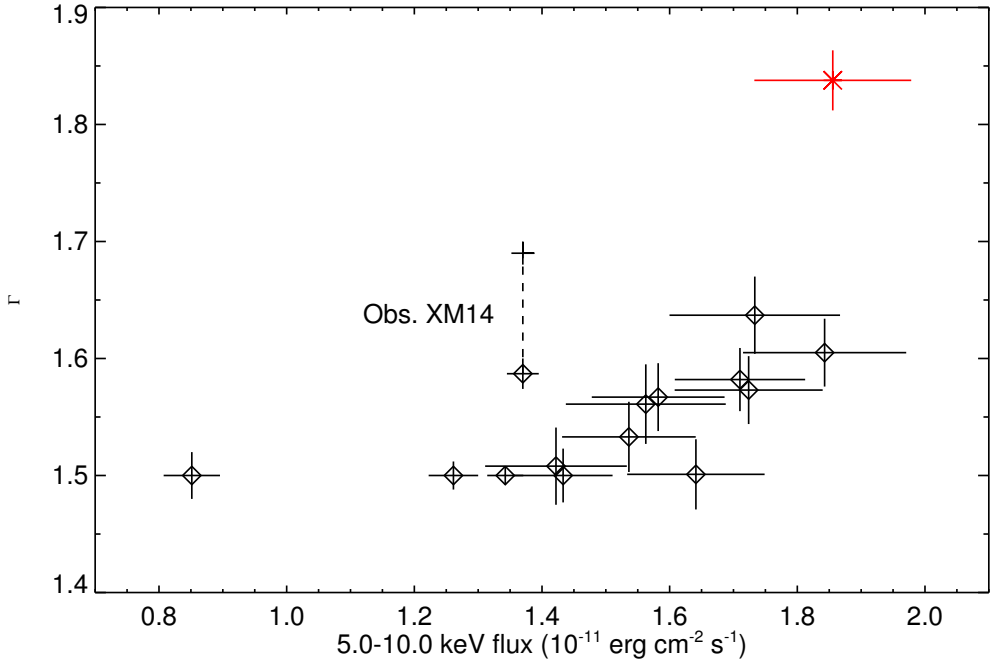
Figure 3.8: Fitted continuum slope as a function of the observed 5.0–10.0 keV flux for all XMM-*Newton* and *Chandra* data sets, with errors. Black diamonds and red asterisk identify parameters measured with XMM-*Newton* and Chandra-LETGS, respectively. The black cross represents the higher value of Γ that, for Obs. XM14, would be required by a fit including the cold obscurer (see Sect. 3.4.3).

in prep). In the present analysis, we also consider the ionized phase of the obscurer (K14), while U15 use two purely neutral components. This can affect the broadband curvature of the model. Moreover U15 has an additional degree of freedom in the high-energy cutoff of the continuum. For all these reasons, the only meaningful comparison is among the overall trend of the parameters. Even taking the differences between our analysis and the one presented in U15 the parameters into account, trends that we discuss below still hold.

3.5.2 What drives the variability?

To understand if there are some systematic factors driving the short-term variability of the source, we looked for correlations among the best-fit parameters and the unobscured flux measured for the 16 data sets presented here. We used the hard X-ray flux in the 5.0–10.0 keV band and the UVW2 flux listed in Table 3.1 as tracers of the intrinsic continuum, as they are almost unaffected by the obscuration. Even considering these unabsorbed bands, the range of flux sampled in the monitoring campaign is narrow (a factor of ∼2), with
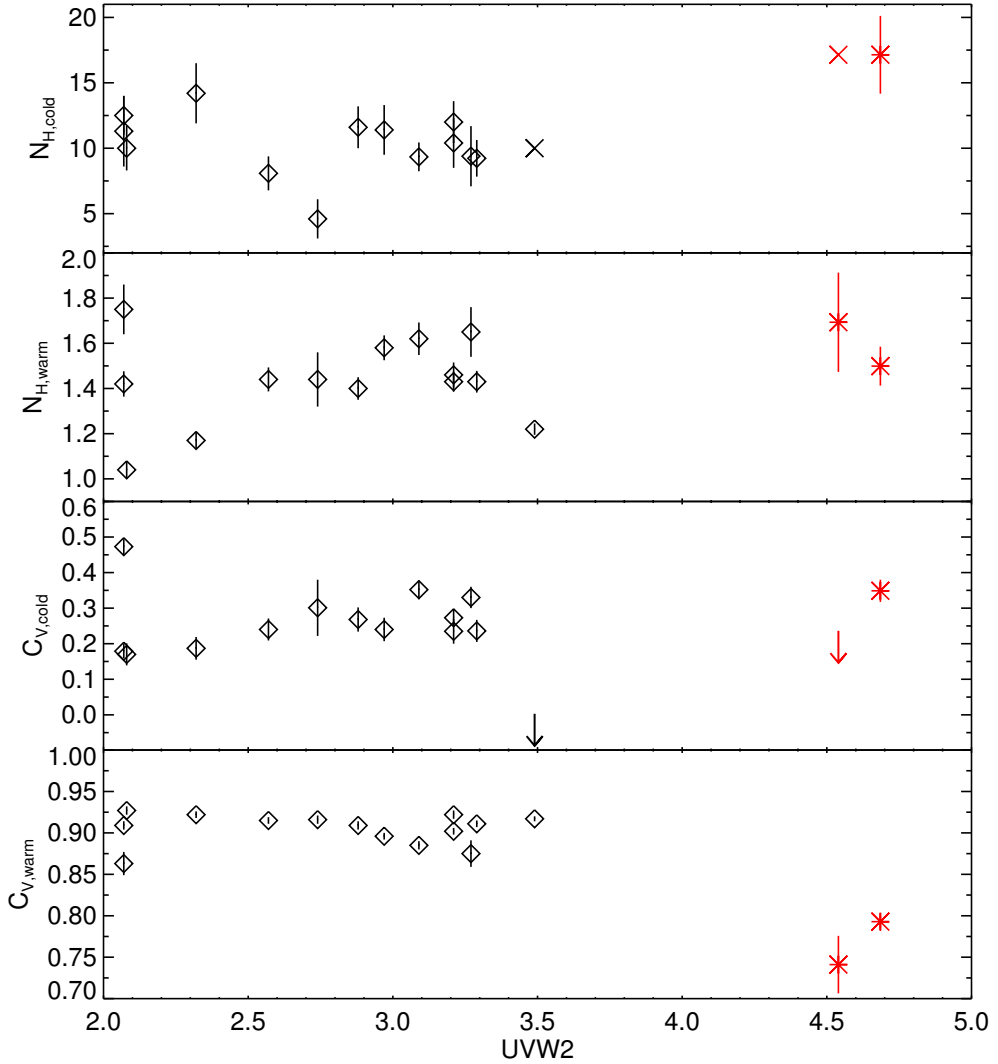
Figure 3.9: From top to bottom panel: the column densities of the cold and the warm obscurer, covering fraction of the cold and the warm obscurer are plotted as function of the flux in the UVW2 filter. Column densities are plotted in units of 10^{22} cm^{-2}. The UVW2 flux is plotted in units of 10^{-14} erg s^{-1} cm^2 A^{-1}. Black diamonds and red asterisks identify parameters measured with XMM-*Newton* and Chandra-LETGS, respectively. Error bars, when larger than the size of the plotting symbol, are also shown. Upper limits are plotted as an arrow. Crosses represent values that were kept frozen in the fits.

the only outliers at lower and higher flux being Obs. XM1 and Obs CH2+3. Therefore, to evaluate the reliability of any correlations we checked if this still holds when we remove these two data points from the computation of the Pearson correlation coefficient.

In Fig. 3.8 we show that the best-fit continuum slope steepens as the hard X-ray flux increases. For the complete sample the correlation is extremely significant. The Pearson correlation coefficient is $R_{all} = 0.85$, implying a probability $p \sim 10^{-5}$ for the null hypothesis. When excluding Obs. XM1 and Obs. CH2+3 from the computation, the degree of correlation still remains significant ($R_{XM2-XM14}$=0.68, $p_{XM2-XM14}$=1%). This trend has already been noticed in the past for NGC 5548 in Kaastra et al. (2004) and has also been reported in other Seyfert galaxies (e.g., MCG 6-30-15 Shih et al. 2002), with different interpretations (see, e.g., Ponti et al. 2006, Giacchè et al. 2014). In the same Fig. 3.8 we show also that for Obs. XM14, the higher value of Γ that would be required by a fit, including a thick cold obscurer (that we rejected, see. Sect. 3.4.3), is inconsistent with the correlation valid for all the other data sets.

In Fig. 3.9 we plot the parameters of both the obscurer phases as function of the UVW2 flux. The only parameter showing a possible trend with the intrinsic continuum is the warm covering factor. Namely, the drop observed during the *Chandra* observations may be the tail of a mild decreasing trend visible also for the XMM-*Newton* data points (Fig. 3.9, bottom panel). Formally, when the two *Chandra* data points are included in the computation, a significant correlation ($R_{all} = -0.73$, p_{all}=1%) is present. When considering only the XMM-*Newton* sample, the trend is only qualitative ($R_{XM1-XM14} = -0.03$ $p_{XM1-XM14}$=25%). In Sect. 3.5.1 we suggested that the drop in covering fraction observed during the September 2013 flare is due to an increase in the size of the soft X-ray/UV source. A clear correlation between the warm covering fraction and intrinsic continuum, supported by more numerous data points at different flux values, would favor the hypothesis that this is a systematic effect producing at least part of the observed covering fraction variability. This trend is not apparent for the cold covering fraction. This could be due to a higher degree of inhomogenity in the cold phase that would also explain its larger variability in covering fraction (e.g., it went from 0.47 in Obs XM1 to 0 in Obs. XM14).

In conclusion, a combination of changes in the continuum and in the obscurer physical parameters is required to explain the short-term spectral variability of NGC 5548 during our 2013-2014 campaign. The lack of correlation between the intrinsic continuum (as traced by the UVW2 flux) and obscurer parameters indicate that the obscurer must physically change properties independent of the source flux level. The case of the September 2013 spectrum suggests that the soft X-ray emitting region change geometry as the flux increases. This could be a systematic effect contributing to the overall covering fraction variability.

3.6   Summary and conclusions

During the multiwavelength monitoring campaign that we performed in 2013-2014 for the Seyfert 1 galaxy NGC 5548, the source had a soft X-ray flux well below the long-term average, except for a two-week-long flare in September 2013. In K14, we have ascribed

this condition to the onset of a persistent, weakly-ionized but high-velocity wind that blocks ∼90% of the soft X-ray flux and lowers the ionizing luminosity received by the WA. Thus, in this condition, the normal WA that was previously observed in this source is still present, but with a lower ionization. We fitted all the high resolution XMM-*Newton* and *Chandra* data sets that were taken during the campaign with a model that consistently accounts for a variable continuum, the newly discovered obscurer, and the new ionization conditions of the historical WA. We found that on the timescales sampled in the monitoring campaign (2 days–8 months) both the intrinsic continuum and the obscurer are variable. The obscuring material varies both in column density and in covering fraction. This rapid variability is consistent with the picture of a patchy wind proposed by K14. The *Chandra* spectra that were taken just after the peak of the flare in September 2013 are explained by both an increase and a steepening of the intrinsic continuum and a drop in the obscurer covering fraction. The latter is likely to be because of a geometrical change of the soft X-ray continuum source behind the obscurer.

Moreover, the spectrum show absorption from Fe-UTA, O IV, and O V, consistent with belonging to the lower-ionized counterpart of the historical NGC 5548 warm absorber. These are the only individual WA features in any X-ray spectrum of the campaign. We also looked for correlation between the fitted parameters and some tracers of the intrinsic continuum flux. A positive correlation between the X-ray continuum slope and the observed 5.0–10.0 keV flux holds for both the XMM-*Newton* and *Chandra* data sets. The addition of the two *Chandra* points produce a formal anticorrelation between the warm obscurer covering fraction and the intrinsic continuum luminosity, as traced by the observed UVW2 flux.

ACKNOWLEDGEMENTS

4 _ The warm absorber in the radio-loud quasar 4C +74.26

L. Di Gesu and E. Costantini

··· **Abstract** ···

Outflows of photoionized gas are commonly detected in the X-ray spectra of Seyfert 1 galaxies. However, the evidence for this phenomenon in broad line radio galaxies, which are the analogous of Seyfert 1 in the radio-loud regime, has so far been scarce. Here, we present the analysis of the X-ray absorption in the radio-loud quasar 4C +74.26. With the aim of characterizing both the kinetic and the ionization conditions of the absorbing material, we fitted jointly the XMM-Newton-RGS and the Chandra-HETGS spectra, that were taken 4 months apart. The intrinsic continuum flux did not vary significantly during this time lapse. The spectrum shows the absorption signatures (e.g., Fe-UTA, O VII, and Ne VII–Ne X) of a photoionized gas outflow ($N_H \sim 3.5 \times 10^{21}$ cm^{-2}, $\log \xi \sim 2.6$, $v_{out} \sim 3600$ km s^{-1}) located at the redshift of source. We estimate that the gas is located outside the broad line region but within the boundaries of the putative torus. This ionized absorber is consistent to be the X-ray counterpart of a polar scattering outflow reported in the optical band for this source. The kinetic luminosity carried by the outflow is insufficient to produce a significant feedback is this AGN. Finally, we show that the heavy soft X-ray absorption that was noticed in the past for this source arises mostly in the Galactic ISM.

···

4.1 Introduction

In the last fifteen years, thanks to the advent of high resolution X-ray spectrometers, such as the XMM-*Newton* Reflection Grating Spectrometer (RGS) or the *Chandra* Low and High Energy Transmission Grating Spectrometers (LETGS and HETGS), our knowledge of the circumnuclear gaseous environment of Active Galactic Nuclei (AGN) significantly advanced.

It is now established that roughly half of all local Seyferts galaxies host a photoionized warm absorber (WA) that produces features detectable in the X-ray and in the UV band (Crenshaw et al. 2003b). These absorption lines are usually blueshifted with respect of the systemic velocity, which indicates a global outflow of the absorbing gas. Spectroscopical observations allow to characterize the physical conditions (kinematics and ionization) of the gas with high accuracy (see Costantini 2010, for a review). In photoionization equilibrium, the ionization parameter $\xi = L_{ion}/n r^2$ (where L_{ion} is the ionizing luminosity between 1 and 1000 Ryd, n is the gas density, and r is the distance from the ionizing source) parameterizes the state of the gas. In the X-ray band, a plethora of transitions from e.g., ionized C, N, O, Ne, and Fe reside, which allows to determine an accurate solution for ξ. From spectroscopical observables, useful constraints can be put on the gas location (Blustin et al. 2005), which serve to quantify how much momentum is transferred by the outflow to the surrounding medium (e.g., Crenshaw & Kraemer 2012).

The studies of WA in Seyfert galaxies show that these outflows span roughly four orders of magnitude in ionization ($\log \xi \sim 0-4$), and reach velocities of few thousands km s^{-1} (McKernan et al. 2007). They are often located as far as the putative torus (Blustin et al. 2005). Some outliers may be located closer to the nucleus, at the distance of the accretion disk, or farther out in the galaxy at $\sim$kpc distance from the center (Di Gesu et al. 2013). In most of the cases, the kinetic power of the WA is found to be negligible with respect to the AGN radiative power (e.g., Ebrero et al. 2016). Thus, WA are not expected to play a significant role in a possible negative AGN feedback (Scannapieco & Oh 2004, Somerville et al. 2008, Hopkins et al. 2008, Hopkins & Elvis 2010, King & Pounds 2015).

A different class of photoionized winds are the so-called ultrafast outflows (UFO). These may be present in 35% (Tombesi et al. 2010) of Seyfert galaxies and differ from classical WA because of the higher outflow velocity (v$\sim$0.1 c, where c is the speed of light) and of the higher ionization ($\log \xi \geq 3$, Tombesi et al. 2011). Hence, because of the higher energy and higher blueshift of their transitions (e.g., Fe XXV–Fe XXVI), UFO are detectable only in lower-resolution CCD spectra. These powerful winds are believed to be a nuclear phenomenon originating from the accretion disk (Tombesi et al. 2012, Nardini et al. 2015).

The detection of photoionized features in broad line radio galaxies (BLRG), which are the analogous of Seyfert 1 in the radio loud regime, was expected to be difficult because of the presence of a relativistic jet. Indeed, the Doppler-boosted, non-thermal radiation of a jet located close to the line of sight could mask the absorption features. Although this view has now been overcome, the statistics of known WA in BLRG relies on a handful of cases, of which only three are WA detection in a high resolution X-ray dataset.

Hints of photoionized absorption were noticed, for instance, in the ROSAT-PSPC spectrum of 3C 351 (Fiore et al. 1993) and 3C 212 (Mathur 1994). Interestingly, these two sources

display WA features also in the UV (Mathur et al. 1994, Yuan et al. 2002). More recently, Molina et al. (2015) reported the detection of O VII and of Fe XX absorption edges in the EPIC-pn spectrum of IGR J14488-4008, a giant radio-loud galaxy discovered by INTEGRAL. The first case of a WA in a BLRG studied with a grating spectrum was a long *Chandra*-HETGS spectrum of 3C 382 (Reeves et al. 2009). The detection of this WA, which is consistent to be located at the distance of the narrow line region (NLR), was promptly confirmed by a subsequent RGS observation (Torresi et al. 2010). A second case is the remarkable photoionized outflow in 3C 445. In the *Chandra*-HETGS spectrum of this source Reeves et al. (2010) detected a low-ionization outflow consistent with moving at a sub-relativistic velocity. A deep Suzaku spectrum shows also indications of blueshifted absorption from highly-ionized iron (Braito et al. 2011). Both these spectra are consistent with a scenario where our line of sight intercepts an equatorial disk wind located at ~sub-pc scale. The low-ionization absorber may consist of sparse clumps embedded in a highly-ionized wind (Reeves et al. 2010). Besides these two cases, Torresi et al. (2012) report a WA detection in the RGS spectrum of 3C 390.3.

Signatures of more highly-ionized UFO have been also detected in the CCD spectra of a handful of radio loud sources (Tombesi et al. 2014), with a statistical incidence comparable, within the uncertainties, to what is found for radio-quiet Seyferts.

In this paper, we present the analysis of the X-ray grating spectrum, obtained with the RGS and the *Chandra* -HETGS, of the BLRG 4C +74.26. This source is located at a redshift of 0.104 (Riley et al. 1989). In the optical, it shows broad permitted lines, with a a *FWHM* of 10 000 km s^{-1} for the H$_\beta$ line (Winter et al. 2010). Using this line width a SMBH mass of 3×10^9 M$_\odot$ is inferred.

Because of its ~1 Mpc projected linear size (Riley et al. 1989), this source is the largest known radio source associated with a quasar. Its radio morphology is typical for a Fanaroff-Riley type II source (FRII), although the 178 MHz radio luminosity is border line with the type I class (FRI). Observations with the Very Large Array (VLA) have revealed a one-sided jet which is at least 4 kpc long (Riley & Warner 1990). The flux limit for a counter-jet, that could be set with a subsequent Very Long Baseline Interferometry (VLBI) observation (Pearson et al. 1992) implies that the source axis lies at $\lesssim 49°$ from our line of sight.

Evidence for a high-velocity outflow in 4C +74.26 was found in the optical spectropolarimetric analysis performed in Robinson et al. (1999). These authors noticed that the broad Hα line appears redshifted in polarized light, which can be explained if the scattering medium producing the polarization is part of a polar outflow.

Since 1993, 4C +74.26 has been targeted by many X-ray observatories, including ROSAT, ASCA, *Beppo*-SAX XMM-*Newton*, and *Suzaku*. Both in the XMM-*Newton* (Ballantyne & Fabian 2005) and in the Suzaku (Larsson et al. 2008) spectrum a broadened Fe Kα emission line has been clearly detected at 6.4 keV. Recently, in both the Suzaku (Gofford et al. 2013) and the XMM-*Newton* spectrum (Tombesi et al. 2014) additional absorption features in the Fe-K band were noticed. These could be due to a highly-ionized UFO, with a measured outflow velocity of the order of $\sim 0.1c$.

By studying the correlations between the Suzaku light-curves in different bands, Noda et al. (2013) were able to extract the stable soft-excess (Singh et al. 1985) component that

may dominate the continuum emission at soft energies (i.e. below 2.0 keV). According to these authors, the most likely origin for the soft-excess in this source is thermal Comptonization of the disk photons in a warm plasma (as in e.g., Noda et al. 2011, Done et al. 2012, Jin et al. 2012, Petrucci et al. 2013, Di Gesu et al. 2014, Giustini et al. 2015, Boissay et al. 2016).

It was however noticed that the soft-excess underlies a heavy soft X-ray absorption. For instance, absorption from a substantial column density of gas in excess at the Galactic column density was earlier on noticed in the ROSAT-PSPC (Brinkmann et al. 1998), ASCA (Brinkmann et al. 1998, Sambruna et al. 1999, Reeves & Turner 2000) and Beppo-SAX (Hasenkopf et al. 2002) spectrum. In a more recent XMM-*Newton* observation, Ballantyne (2005) detected a column of cold absorption greater than the Galactic value, with an intrinsic column of $\sim 1.9 \times 10^{21}$ cm^{-2}. Moreover, the broadband XMM-*Newton* spectrum shows evidence for a weak WA intrinsic to the source. The latter is highlighted by features identified as the O VII and O VIII absorption edges (Ballantyne & Fabian 2005).

Motivated by these indications for a complex absorption in this source, here we use the archival XMM-*Newton* Reflection Grating Spectrometer (RGS) and *Chandra* High Energy Trasmission Grating Spectrometer (HETGS) spectra of 4C +74.26 to characterize for the first time the kinematics and the ionization condition of the X-ray absorbing material.

In the following Sect. 4.2 we describe our data reduction procedure. Hence, in Sect. 4.3 we build the spectral energy distribution (SED), and in Sect. 4.4 we perform the spectral analysis. Finally in Sect. 4.5 we discuss our results and in Sect. 4.6 we state the conclusions.

The C-statistic (Cash 1979) is used throughout the paper, and errors are quoted at 68% confidence level ($\Delta C = 1.0$). In all the spectral models presented, we use the total Galactic hydrogen column density from Willingale et al. (2013, $N_\mathrm{H} = 2.31 \times 10^{21}$ cm^{-2}). In our luminosity calculations we use a cosmological redshift of z=0.104 and a flat cosmology with the following parameters: H_0=70 km s^{-1} Mpc^{-1}, Ω_m=0.3, and Ω_Λ=0.7.

4.2 Observations and data preparation

The radio-loud galaxy 4C +74.26 was observed with *Chandra* and XMM-*Newton* in October 2003 and February 2004, respectively. Thus, the time separation between these X-ray observations is only 4 months. In Table 4.1 we summarize the basic information of each observation.

Chandra observed 4C +74.26 for ∼70 ks in total using the HETGS in combination with the ACIS detector. The total exposure time was split into two observations that were taken two days apart. For both Obs-ID 4000 and 5195 we retrieved the Medium (MEG) and High Energy Grating (HEG) spectra and their respective response matrices from the *tgcat*[1] archive. We further treated these spectral products with the CIAO (version 4.6) tools. For each observation and for both HEG and MEG, we combined the first positive and negative spectral order using the CIAO script add_spectral_orders. Hence, we fitted jointly HEG and MEG (allowing a free intercalibration factor) with a simple phe-

---

[1] http://tgcat.mit.edu/

Table 4.1: XMM-Newton and *Chandra* observation log for 4C +74.26.

Date	Instrument	Observation ID	Net exposure [a] (ks)	$F_{0.3-2.0\,keV}$ [b]	$F_{2.0-10.0\,keV}$ [b]
				$(10^{-11}$ erg s^{-1} cm$^2)$	
2003/10/06	HETGS	4000	37	0.7	2.8
2003/10/08	HETGS	5195	31	0.8	2.9
2004/02/06	RGS	0200910201	34	0.9	3.0

Notes. [a] Resulting exposure time after correction for background flares. [b] Observed flux in the quoted bands.

nomenological power law to check for variability between the two observations. The fitted slopes ($\Gamma_{4000} = 1.32 \pm 0.02$, $\Gamma_{5195} = 1.34 \pm 0.02$) and normalizations ($Norm_{4000} = (9.9 \pm 0.1) \times 10^{53}\,\mathrm{ph\,s^{-1}\,keV^{-1}}$, $Norm_{5195} = (10.5 \pm 0.2) \times 10^{53}\,\mathrm{ph\,s^{-1}\,keV^{-1}}$) were well consistent with each other (see below for a physically motivated fit). Therefore, we could sum up the spectra of individual observations into a single spectrum to improve the signal-to-noise. We did this using the CIAO script add_grating_spectra.

We reduced the raw XMM-*Newton* Observation Data Files (ODF), available at the ESA archive[2], using the Science Analysis Software (SAS, version 13) and the HEASARC FTOOLS. We created calibrated EPIC-pn event files selecting only the unflagged single events. To check the time stability of the background we used the light curve in the hard 10–12 keV band, that is background dominated. A high level of background due to soft proton contamination is evident towards the end of the observation. Thus, we cleaned the event file using a time filter, following the same procedure explained in Di Gesu et al. (2013). For RGS-1 and RGS-2 we created calibrated event files and background light curves taking the background from CCD 9. The RGS background light curve was quiescent. Next, for all the instruments, we extracted the source and background spectra and we created the spectral response matrices.

Finally, we extracted the source count rate in all the available OM filters, namely U ($\lambda_{\mathrm{eff}} = 3440$ Å), $UVW2$ ($\lambda_{\mathrm{eff}} = 2910$ Å) and $UVM2$ ($\lambda_{\mathrm{eff}} = 2310$ Å). Using the interactive SAS tool omsource, we computed the source count in a circular region centered on the source coordinates and 6 pixels large. For the background we used another circular region of 12 pixels, free from other sources and instrumental contaminations. We converted the count rates to fluxes using the standard conversion factors provided in the SAS watchout web page[3]. Hence, assuming R_V=3.1, we corrected all the fluxes for the Galactic reddening ($E(B-V)$=0.39, Schlafly & Finkbeiner 2011). For the correction, we used the IDL routine ccm_unred, which dereddens a user-defined vector of fluxes using the Galactic extinction curve of Cardelli et al. (1989).

---

[2]http://xmm.esac.esa.int/xsa/
[3]http://xmm.vilspa.esa.es/sas/7.1.0/watchout/Evergreen_tips_and_tricks/uvflux_old.shtml
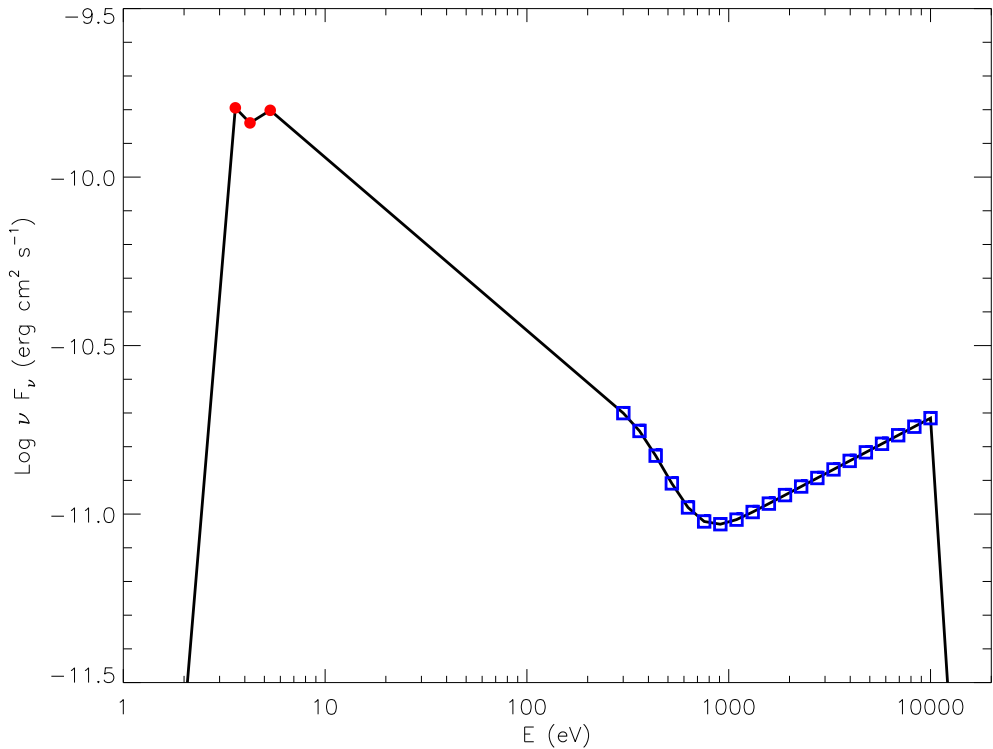
Figure 4.1: Spectral energy distributions for 4C +74.26. Filled circles: OM fluxes corrected for the Galactic extinction. Open squares: X-ray intrinsic continuum, obtained from a phenomenological fit of the EPIC-pn spectrum.

4.3 The spectral energy distribution

As a preliminary step of our analysis we constructed the Spectral Energy Distribution (SED) of the source. This is needed for the photoionization modeling of the absorbers. The OM fluxes together with the EPIC-pn spectrum constrain the SED from optical/UV up to X-ray energies. We fitted the EPIC-pn data with a phenomenological model including a black-body ($T_{BB} = 109$ keV) at soft energies, a power-law ($\Gamma = 1.7$) at hard energies, and a broad Fe Kα line (*FWHM*=0.5 keV). All these components are absorbed by the Galactic column density of N_H =2.31 ×10^{21} cm^{-2} (see the discussion below). We adopted the unabsorbed phenomenological continuum of this fit as the the X-ray SED. Combining this X-ray continuum (Fig. 4.1, open squares) with the OM fluxes corrected for the Galactic extinction (Fig. 4.1, filled circles) we obtained the SED shown in Fig 4.1. We cut off the SED at low and high energy, respectively at 0.01 Ryd and 100 keV.
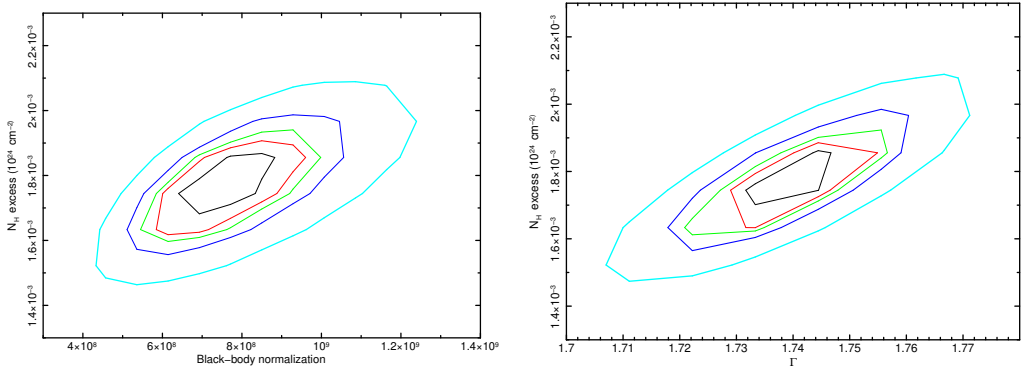
Figure 4.2: Confidence level contour plot for the excess of N_H over the Galactic value of Kalberla et al. (2005) vs the normalization of the modified blackbody (*left panel*) and the power-law slope (*right panel*). The curves were obtained from a phenomenological fit of the EPIC-pn (Sect. 4.3). In each panel, the curves correspondent to a confidence level of 68%, 90%, 99% and 99.99% are shown.

4.4 Spectral Analysis

4.4.1 The Galactic absorption

The X-ray spectrum of 4C +74.26 showed a heavy soft X-ray absorption in excess at the Galactic column measured by 21 cm surveys (e.g., $N_H = 1.16 \times 10^{21}$ cm^{-2}, Kalberla et al. 2005) in all the historical records (Sect. 4.1). We illustrate this issue using our phenomenological fit of the EPIC-pn spectrum (Sect. 4.3). In Fig. 4.2, we show the confidence contour (i.e. curves of constant Δ C) of the N_H excess as a function of the modified black-body normalization (left panel) and of power-law slope (right panel) . An excess of N_H of at least $\sim 1.5 \times 10^{21}$ cm^{-2} is observed in both figures at a confidence level of 99.99%.

Part of this excess of absorption can be due the gas in our Galaxy rather than to some absorber intrinsic to the source. Indeed, the total foreground X-ray absorption may be, in some cases, significantly larger than what is inferred using the N_H value provided by 21 cm surveys (Kalberla et al. 2005, Dickey & Lockman 1990). The difference may be ascribed to the presence of hydrogen in molecular form (H_2) in the Galactic ISM (Arabadjis & Bregman 1999). The latter is indeed elusive to 21 cm measurements. We used the calibration of Willingale et al. (2013) [4] to infer the equivalent hydrogen column density of the the molecular hydrogen (N_{H_2}) along the line of sight of 4C +74.26. We found $N_{H_2} = 1.15 \times 10^{21}$ cm^{-2}. Thus, the total Galactic hydrogen column density absorbing the X-ray spectrum is: $N_H + N_{H_2} = 2.31 \times 10^{21}$ cm^{-2}, consistent with the total column density inferred from the broadband X-ray spectrum (Ballantyne 2005). Applying the standard Galactic $E(B-V)/N_H$ ratio (1.77×10^{-22}, Predehl & Schmitt 1995), this hydrogen column density is also consistent with the Galactic reddening of $E(B-V)$=0.39 (Schlafly

---

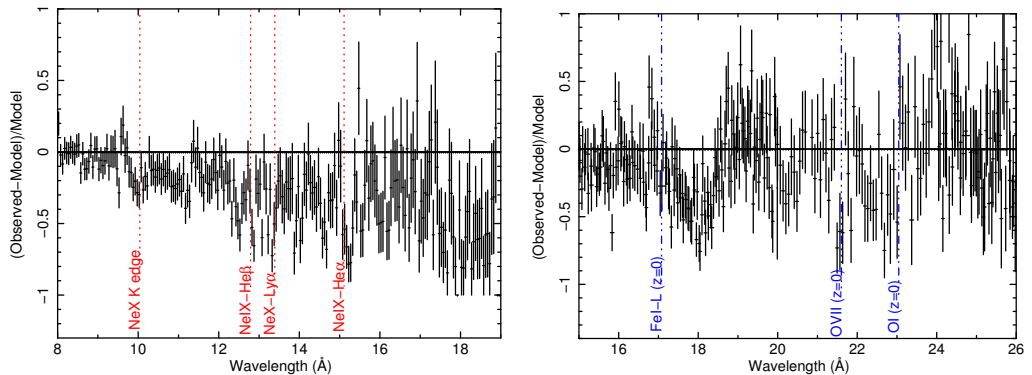[4] http://www.swift.ac.uk/analysis/nhtot/index.php

Figure 4.3: Relative residuals of the MEG (*left panel*) and the RGS (*right panel*) spectrum after a simple power law fit. Vertical lines indicate the wavelengths of the Galactic (dotted-dotted-dotted-dashed line) and intrinsic (dashed line) candidates absorption lines and edges. The spectra have been rebinned for clarity.

& Finkbeiner 2011). We use this Galactic column density value in all the spectral analysis here below. The remainder of the excess absorption is due to the photoionized gas of the outflow (see Sect. 4.4.8). In fact, as our model shows, there is no need for additional neutral gas when this outflow is taken into account.

4.4.2   A preliminary look at the spectral residuals

We performed the spectral analysis of the RGS and the HEG datasets using SPEX, version 3.0 (Kaastra et al. 1996). We began by fitting the RGS spectrum with a simple power law continuum absorbed by the Galactic hydrogen column density and we inspected the relative residuals (Fig. 4.3, right panel).

The most prominent features in the RGS residuals is a broad absorption trough visible at ~ 18 Å. We note that the Fe-L edges from the neutral absorber in our Galaxy cannot be responsible for this feature, as they would be expected at ~17.1 Å. Moving redward, a narrow feature, located at the wavelength expected for the O VII absorption line (~ 21.6 Å) at redshift zero, is clearly visible. Between 23 Å and 24 Å, where redshifted O VII transitions are expected, the residuals are systematically positive. This structure is a candidate broad emission line. Absorption from other transitions of ionized oxygen are also expected in this crowded spectral region (e.g., Detmers et al. 2011).

We repeated this exercise for the HETGS spectrum. Guided by the knowledge of the RGS spectrum, we could recognize also in the MEG the same absorption trough at ~ 18 Å. In the MEG this falls towards the end of the sensitive band, where the effective area starts degrading. Blueward of this, between 10 and 15 Å, the HETGS residuals show some candidate absorption lines from the main Ne IX–Ne X transitions, indicating that some photoionized absorption may affect this spectrum.
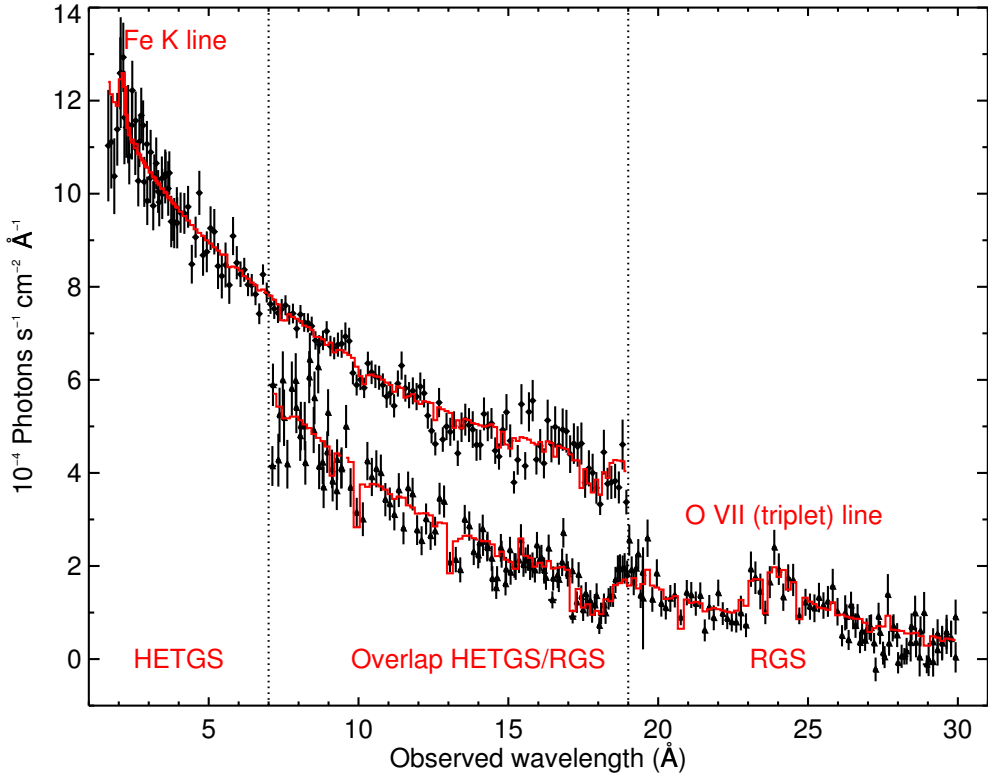
Figure 4.4: Best fit of the RGS and of the HETGS spectrum of 4C +74.26. The diamonds and the triangles indicate the HETGS and the RGS data points respectively. The HETGS spectrum has been shifted upwards (× 3) for displaying purpose. Vertical lines indicate the band where the instruments overlap. The solid lines represent our best fit models. Emission lines are labeled. The spectra have been rebinned for clarity.

4.4.3   Setup of the joint RGS/HETGS fit.

The qualitative analysis of the RGS and of MEG spectra shows hints of a complex ionized absorption in this source.

In order to accurately disentangle the multiple absorption components of this spectrum, we fit jointly the RGS and the HETGS data sets. The negligible variation in observed flux during the ~4 months separating these two observations (Table 4.1) is indeed an indication that the source and the absorbers were in the same conditions when these two spectra were taken. With a joint fit we take advantage of both the high HETGS spectral resolution at short wavelengths, where most of the features from higher ionization species are expected, and the high sensitivity of the RGS at long wavelengths, where the absorption features of e.g. ionized iron and oxygen reside.

In the fit, we used the RGS between 7 and 30 Å and the MEG between 2 and 19 Å. The

Table 4.2: Best fit parameters and errors for the final best fit model. Parameters without errors were kept coupled in the fit, either to the RGS or to the HETGS value.

Model component	Parameter	RGS value	HETGS value	Units
Power law	Γ [a]	1.67 ± 0.05	1.68 ± 0.02	
	$L_{0.3-10.0\,\text{keV}}$ [b]	13.7 ± 0.5	11.4 ± 0.3	10^{44} erg s^{-1}
Black-body	T_{BB} [c]	170 ± 15	170	eV
	$L_{0.3-10.0\,\text{keV}}$ [b]	1.7 ± 0.8	1.0 ± 0.8	10^{44} erg s^{-1}
Fe Kα line	w [d]	1.92	1.92 ± 0.08	Å
	$FWHM$ [e]	0.16	0.16 ± 0.13	Å
	$L_{\text{Fe K}\alpha\,\text{line}}$ [b]	7	6 ± 4	10^{42} erg s^{-1}
O VII (triplet) line	w [d]	21.7 ± 0.1	21.7	Å
	$FWHM$ [e]	1.0 ± 0.3	1.0	Å
	$L_{\text{O VII line}}$ [b]	9 ± 3	9	10^{42} erg s^{-1}
Warm Galactic absorber	N_{H} [f]	2 ± 1	1.2	10^{20} cm^{-2}
	T [g]	0.23 ± 0.04	0.20	keV
Intrinsic warm absorber	N_{H} [f]	3.5 ± 0.6	3.1 ± 0.3	10^{21} cm^{-2}
	$\log \xi$ [h]	2.5 ± 0.1	2.57 ± 0.06	erg cm s^{-1}
	v_{out} [i]	3600	3600 ± 70	km s^{-1}

Notes. [a] Power law slope. [b] Model component luminosity, in the quoted band. [c] Blackbody temperature. [d] Wavelength of the line centroid. [e] Full width at half maximum of the line. [f] Absorber column density. [g] Absorber temperature. [h] Absorber ionization parameter. [i] Absorber outflow velocity.

quality of the HEG spectrum is worse than the MEG, thus we use HEG only in the Fe Kα region between 1.5 and 5 Å. For the joint fit, we created two spectral sectors in SPEX, one for the RGS (RGS 1 and RGS 2) and one for the HETGS (HEG and MEG). In this way, each instrument is fitted independently, but the model parameters can be coupled. In the following, we fit jointly the HETGS and the RGS tying the absorption components together but allowing the continua to vary. In Fig. 4.4 we show the final best fit model in the total energy range covered.

4.4.4   Continuum

We set a simple continuum model comprising a power law and a phenomenological modified blackbody mimicking a soft-excess (Singh et al. 1985) component. For the latter we used the MBB model in SPEX, which includes the effect of Compton scattering (Kaastra & Barr 1989). In the fit we always kept the modified blackbody temperature of the HETGS model coupled to the RGS value because, in our fit, the band where the soft-excess component is supposed to dominate is mostly covered by the RGS. For the power-law component, we set the initial value of the slope to the one determined by the EPIC-pn fit. As the best fit was reached, the value of Γ settled at 1.67 ± 0.05, while we found $T_{\text{BB}} = 170 \pm 15$ eV. The final best fit values for the continua are given in Table 4.2, 1st and
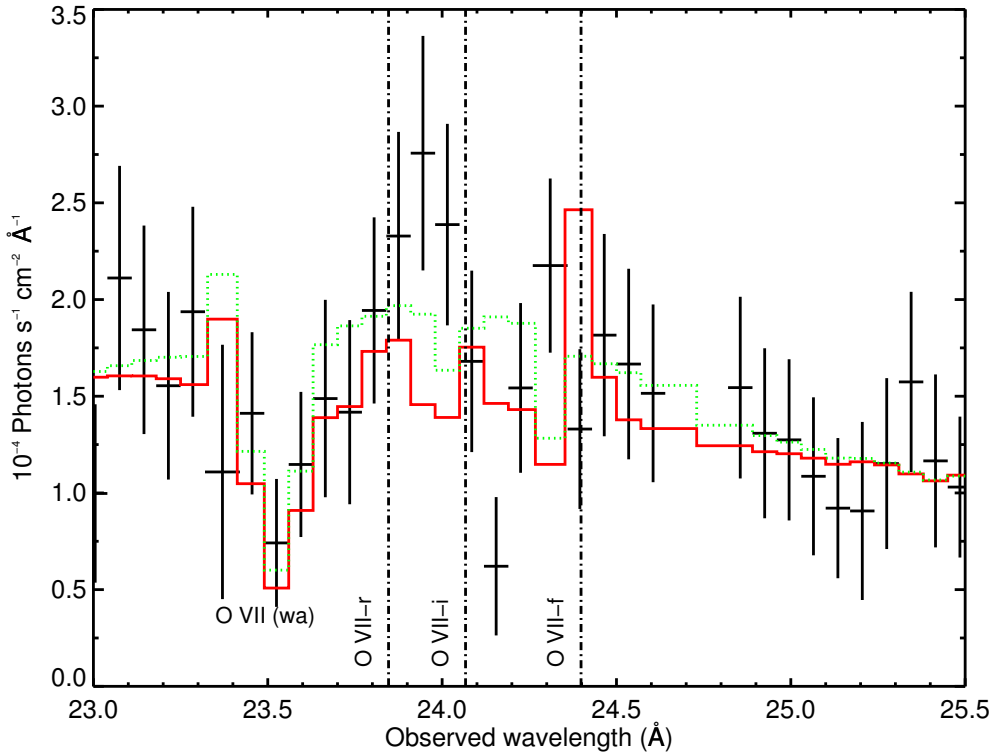
Figure 4.5: RGS-1 spectrum of 4C +74.26 in the 23.0–25.5 wavelength region. The vertical dash-dotted lines mark the position of the resonance, intercombination, and forbidden line. The solid line represents the fit with a narrow profiled O VII triplet, which we were forced to reject (see Sect. 4.4.5). The dotted line represents our best fit model with a single Gaussian line representing a broadened O VII triplet. In both cases, the triplet profile is affected by absorption from ionized oxygen (O VII) intrinsic to the source as labeled. The spectrum has been rebinned for clarity.

2nd panel. A small difference in the normalizations of the continuum components is sufficient to account for the change of flux between the HETGS and the RGS observations.

4.4.5   Emission lines

The presence of a broad Fe Kα emission line in 4C +74.26 is well established (Ballantyne & Fabian 2005, Larsson et al. 2008). The line is also well visible in the HETGS data (Fig. 4.4). We fitted it with a phenomenological Gaussian emission line with free centroid, width, and normalization. The values we obtained (Table 4.2, 3rd panel) are well consistent both with what is reported in the literature (Ballantyne 2005) and with our phenomenological fit of the EPIC-pn (Sect. 4.3).

In Fig. 4.5, we show the spectrum in the 23–25.5 Å range where we already noticed an

excess in the residuals (Sect. 4.4.2) reminiscent of a broad emission line. At first, we tested whether these residuals could be accounted for with a narrow-profiled O VII triplet. We added to the fit three delta-profiled emission lines (DELT model in SPEX) for the resonance (λ=21.6 Å), intercombination (λ=21.8 Å), and forbidden line (λ=21.1 Å), respectively. We let the normalization of the forbidden line free to vary and we assumed a ratio 1:3 for the other lines, as expected if photoionization occurs in a low-density plasma approximation (Porquet & Dubau 2000). This fit (Fig. 4.5) does not reproduce well the data and leaves large residuals between 23 and 24 Å.

Thus, we added to the fit a Gaussian profiled emission line. We let the line centroid free to vary among the nominal wavelengths of the O VII triplet and we used the width of the broad H_α line given in Winter et al. (2010) to set the fitting range for the width of a blended triplet (*FWHM*=[0.36–1.23]Å). A broad O VII line having *FWHM*=1.0 ± 0.3 better accounts for the excess in the residuals in the 23–25.5 Å region. For the final fit, the statistical improvement produced by the addition of the O VII broad line is $\Delta C = -24$ for 3 additional degrees of freedom. An F-test gives a probability of a chance improvement of $\sim 10^{-5}$. In this fit the normalization of the narrow components goes to zero, indicating that the data quality does not allow to deblend them from the broad component. The modeling of the broad emission line is critical for a correct evaluation of the absorption (e.g., Costantini et al. 2007, Di Gesu et al. 2013) because many transitions from ionized oxygen may in principle be detected within the line profile. We outline in Table 4.2, 3th and 4th panel, the final best fit values for the line parameters.

4.4.6   A line-by-line fitting of the absorption features

Before proceeding with a global modeling of the absorbing components, we first attempted to identify the absorption features of the spectrum on a line-by-line basis (e.g. Ebrero et al. 2013). We note however that not all the WA features can be identified with this method because of blending with neighboring transitions (as in e.g. the Fe-UTA) or with other components (e.g. Galactic). Moreover, only a global modeling is able to account also for the additional continuum curvature produced by e.g., an ionized absorber.

We visually identified in the spectrum the most prominent features, and for each of those, we added to the model a Gaussian profiled absorption line multiplied by a blueshift model. The line centroid was set the to the wavelength of the nearest known transition, while the line FWHM was set the default value of 0.1 Å. Thus, in this exercise, the free parameters were the line normalization and the blueshift.

In Table 4.3 we list our line identifications. In the RGS band we detected an O VII resonance line at redshift zero and at the redshift of 4C +74.26. The addition of an O VIII-Lyα line ($\lambda = 18.97$ Å) line at the redshift of the source resulted instead in a negligible improvement of the fit (ΔC=-3). In the HETGS band, we detected absorption from Ne IX at redshift 0 and from Ne IX, Ne X, Mg IX, Mg X and Mg XI in the source rest-frame. The magnesium lines are blended, so we fitted them simultaneously with the same blueshift. All the lines detected in the HETGS band show a similar blueshift, suggesting that they may be part of the same outflowing system.

Table 4.3: Identification of the main absorption features in the RGS and in the HETGS spectrum of 4C +74.26.

Wavelength [a]	z [b]	v_{out} [c]	ΔC [d]	Identification	
Å		km s^{-1}		Ion	Transition
21.602	0.104	2100 ± 900	-9	O VII	$1s^2 - 1s2p\,^1P_1$
21.602	0	0	-14	O VII	$1s^2 - 1s2p\,^1P_1$
13.447	0.104	3900 ± 200	-96	Ne IX	$1s^2 - 1s2p\,^1P_1$
13.447	0	0	-47	Ne IX	$1s^2 - 1s2p\,^1P_1$
12.132	0.104	4100 ± 300	-52	Ne X	$1s - 2p$ (Ly α)
9.378 *	0.104			Mg IX	$2s^2 - 1s2s^2 2p$
9.281*	0.104	3600 ± 100	-85	Mg X	$1s^2(^1S)2s - 1s(^2S)2s2p(^3P^0)$
9.169 *	0.104			Mg XI	$1s^2 - 1s2p\,^1P_1$

Notes. [a] Nominal laboratory wavelength of the line. [b] Redshift applied. [c] Blueshift applied. [d] Improvement of the C-statistics with respect to a model including only the continuum, the emission lines, and the Galactic neutral absorber. [*] Lines fitted simultaneously with the same blueshift.

4.4.7 Absorption at redshift zero

We modeled the Galactic cold absorption using a collisionally ionized plasma model in SPEX (HOT), setting a temperature of 0.5 eV for the neutral gas case. This component produces O I and Fe I absorption at ∼23.5 Å and ∼17.4 Å respectively.

As pointed out in Sect. 4.4.2 narrow absorption lines from O VII and Ne IX at redshift zero are detected, respectively in the RGS and in the HETGS spectrum. These could originate in the warm plasma of the Galactic corona, which is collisionally ionized (e.g., Yao & Wang 2005, Pinto et al. 2012). To model it, we added another HOT component to the fit. We let both T and the gas column density N_H free to vary. We kept instead the broadening velocity frozen to the default value of 100 km s^{-1}. The final best fit values that we found for all these free parameters are listed in Table 4.2, 5th panel.

4.4.8 Intrinsic photoionized absorption

We modeled the intrinsic photoionized absorption using the XABS model in SPEX which computes the transmission of a slab of material where all the ionic column densities are linked to each other through the photoionization balance prescribed by the SED (Fig. 4.1). We computed the latter with the SPEX auxiliary tool XABSINPUT and the photoionization code Cloudy (Ferland et al. 2013), version 13.01. For the XABS component, we allowed the column density, the ionization parameter, and the outflow velocity of the gas to vary, while we kept the broadening velocity frozen to the default value of 100 km s^{-1}.

We found that an intrinsic photoionized absorber with $N_H \sim 3 \times 10^{21}$ cm^{-2} and $\log \xi \sim 2.6$ best fits the candidate absorption features of the spectrum. The systematic blueshift of the lines corresponds to an outflow velocity of $v_{\mathrm{out}} \sim 3600$ km s^{-1}. We list in Table 4.2, 6th

Figure 4.6: From the top to the bottom: absorption features of 4C +74.26, in the 8–14 Å (*upper figure*), 14–20 Å (*middle figure*), and 20–26 Å band (*lower figure*). In each figure the transmission (*upper panel*) of the Galactic (long-dashed lines) and intrinsic (solid line) absorbing components is shown together with the ratio between the data and the continuum model (*lower panel*), highlighting the absorption features. The HETGS and the RGS data points are plotted as diamonds and triangles, respectively. The solid line represent the best fit model. Vertical lines mark the position of the most prominent Galactic (dotted-dotted-dashed lines) and intrinsic (dotted lines) absorption features.

panel, the best fit parameters for the WA. After achieving the best fit, we decoupled the column density and the ionization parameter of the RGS model from the HETGS values to check for a possible time variability of the WA in the 4 months separating the HETGS from the RGS observation. We found that during this time interval the WA parameters are consistent not to have varied. We note that a one zone WA is sufficient to best fit the ionized absorption features of the spectrum. Indeed, the fit erases any additional ionized absorbing components, either photoionized or collissionally ionized. The final C-statistics for a model including two Galactic absorbers and an intrinsic WA is C/Expected C=1065/931.

In Fig. 4.6, we show the transmission of all the absorbing components of the model, together with the ratio between the data and the continuum model, which highlights the absorption features. In the RGS band the most evident WA feature is the broad absorption trough visible at ~ 18 Å. This is mostly produced by the unresolved transitions array (UTA) from the ionized iron (e.g., Fe X–Fe XX) contained in the photoionized gas. Besides this, a O VII absorption line is prominent at ~23.5 Å. This feature is blended with the O I line from the neutral absorber in the Galaxy. In the HETGS band, the absorption lines are weak. The most apparent features are from highly-ionized species, such as Ne VII–Ne X and Mg VIII–Mg XI.

4.5 Discussion

We have presented a joint analysis of the RGS and of the HETGS spectrum of the heavily X-ray absorbed radio-loud quasar 4C +74.26. Thanks to the high spectral resolution of these grating spectra, we could reveal a rich spectrum of absorption features, originating from both Galactic and intrinsic material. In our analysis we used the total Galactic column density given in Willingale et al. (2013), which includes the contribution of molecular hydrogen. This is roughly twice the value provided by 21 cm surveys. The enhanced Galactic absorption explains the heavy suppression of the soft X-ray flux that was noticed in the past for this source (Brinkmann et al. 1998, Sambruna et al. 1999, Reeves & Turner 2000, Hasenkopf et al. 2002, Ballantyne & Fabian 2005).

The intrinsic absorption comprises a highly-ionized WA which produces a deep Fe-UTA trough in the RGS and the weak absorption features that are visible in the HETGS spectrum. We found that an outflow velocity of ~ 3600 km s^{-1} is required to best-fit the absorption features visible in both the spectra. This finding is a piece of evidence for WA absorption in radio-loud objects, which so far has been scarce. Indeed, besides 3C 382, 3C 445 and 3C 390.3, 4C +74.26 is the 4th radio-loud source where a photo ionized outflow has been well characterized in a high-resolution dataset. The column density, ionization parameter, and outflow velocity that we measured for the WA in 4C +74.26 are within the range observed in Seyfert 1 galaxies (McKernan et al. 2007) and are also in line with what is found in 3C 382 and 3C 390.3, the other two radio-loud galaxies hosting a classical WA. The case of 3C 445 is an outlier, as this source hosts a high-velocity, high-column UFO-like wind (see the review of Torresi et al. 2012).

In the following sections we use the results of our spectral analysis and the information

Table 4.4: Properties of 4C +74.26.

Source properties	Ref
$M_{\mathrm{BH}} = 3 \times 10^9 \, \mathrm{M}_\odot$	Winter et al. (2010)
$i \leq 49°$	Pearson et al. (1992)
$L_{\mathrm{bol}} = 9.7 \times 10^{46} \, \mathrm{erg \, s}^{-1}$	Sect. 4.5
$L_{\mathrm{bol}}/L_{\mathrm{Edd}} = 0.25$	Sect. 4.5
$\dot{M}_{\mathrm{acc}} = 17 \, M_\odot \, \mathrm{yr}^{-1}$	Sect. 4.5
$L_{\mathrm{ion}} = 8.8 \times 10^{46} \, \mathrm{erg \, s}^{-1}$	Sect. 4.5
$P_{\mathrm{jet}} = 2 \times 10^{44} \, \mathrm{erg \, s}^{-1}$	Sect. 4.5
$P_{\mathrm{jet}}/L_{\mathrm{Edd}} = 6 \times 10^{-4}$	Sect. 4.5
$R_{\mathrm{BLR}} = 0.2 \, \mathrm{pc}$	Sect. 4.5
$R_{\mathrm{TOR}} = 6 \, \mathrm{pc}$	Sect. 4.5
Ionized outflow properties	Ref
$1.6 \leq R \leq 1.8 \, \mathrm{pc}$	Sect. 4.5.1
$f = 7 \times 10^{-5}$	Sect. 4.5.1
$\dot{M}_{\mathrm{out}} = 0.4 \, M_\odot \, \mathrm{yr}^{-1}$	Sect. 4.5.1
$L_{\mathrm{kin}} = 1.5 \times 10^{42}$	Sect. 4.5.1

from the literature to infere a possible geometrical model for the outflow is this AGN. At this purpose, in Sect. 4.5.1 we estimate the possible location and the energetics of the warm absorber. In Table 4.4, upper panel, we outline some basic physical properties of the source that serve for an order of magnitude comparison. We took the black hole mass M_{BH} and the source inclination i, from the literature as already explained in Sect. 4.1. From a numerical integration of the SED of Fig. 4.1 we computed the ionizing luminosity L_{ION} between 1 and 1000 Ry and the bolometric luminosity over the whole optical and X-ray band. We note that the bolometric luminosity is probably underestimated because the radio emission at low energies and the gamma ray emission at high energies are not included in our SED. Hence, using these data we estimated the Eddington luminosity L_{Edd} and the mass accretion rate $\dot{M}_{\mathrm{acc}}$, for which we assumed an accretion efficiency $\eta = 0.1$. For the jet power P_{jet} we used the radio flux at 1.4 GHz (Condon et al. 1998) and the scaling relationship of Cavagnolo et al. (2010). The radius of the broad line region R_{BLR} scales with the optical luminosity at 5100 Å (Wandel 2002). The latter is given in Winter et al. (2010). Finally, the radius of the putative torus R_{TOR}, which is nominally set by the dust sublimation radius, scales with L_{ion} (Krolik & Kriss 2001).

4.5.1 Location and energetics of the ionized outflow

In Table 4.4, lower panel, we outline some physical properties of the ionized outflow that we estimated using our measured parameters, namely $N_{\mathrm{H}} \sim 3.1 \times 10^{21} \, \mathrm{cm}^{-2}$, $\log \xi \sim 2.6$, and $v_{\mathrm{out}} \sim 3600 \, \mathrm{km \, s}^{-1}$. We follow here the argumentation of Blustin et al. (2005) which assumes that the outflow is a partially filled spherical shell of gas, with a volume filling factor f. An analytical expression for the volume filling factor f is derived in Blustin et al.

(2005) from the prescription that that the kinetic momentum of the outflow must be of the order of the momentum of the absorbed radiation plus the momentum of the scattered radiation. For the ionized outflow in 4C +74.26 we found that the ionized gas fills only the ∼ 0.007% of the spherical volume, which suggests that it may consist of sparse clumps. We set a range of possible distances for the absorber from the conditions that the velocity of the outflow must exceed the escape velocity from the AGN and that the outflowing shell must not be thicker than its distance from the center ($\Delta r/R \leq 1$). Analytically:

$$\frac{2GM_{\text{BH}}}{v^2} \leq R \leq \frac{L_{\text{ion}}f}{\xi\,N_{\text{H}}}$$

where G is the gravitational constant. For our parameters, both these expressions return a value ∼2 pc (Table 4.4). This constrains the ionized outflow of 4C +74.26 to be located outside the BLR ($R_{\text{BLR}} = 0.2$ pc) but within the boundary of the putative torus ($R_{\text{TOR}} = 6$ pc)

A patchy ionized outflow located outside the BLR is a natural candidate for being the scattering outflow that is required in the Robinson et al. (1999) analysis of the polarized optical spectrum of this source. Their model prescribes that the observed redshift of the polarized Hα line is due to a high-velocity motion of the scattering material which polarizes the BLR light. In this framework, the outflow velocity inferred for the scatterer depends on the inclination of the scattering cone with respect to the jet axis. For the case of a scattering outflow coaligned with the radio jet, they quote a velocity of ∼5000 km s^{-1}. Interestingly, if we consider the same source inclination used in the Robinson et al. (1999) model (∼ 45°) and we assume that the WA found in our analysis is outflowing along the polar axis of the source, we obtain a deprojected velocity of $v_{\text{out}}/\cos 45°$ ∼5000 km s^{-1}(Fig. 4.7). This matches with what Robinson et al. (1999) predicts. This correspondence hints at the possibility that the WA detected here and the outflowing polar scatterer discovered in Robinson et al. (1999) are one and the same.

Given the velocity, the mass outflow rate is given by

$$\dot{M}_{\text{out}} = \frac{1.23 m_{\text{p}} L_{\text{ion}} f\, v_{out}\Omega}{\xi}$$

where m_p is the proton mass. and Ω is the solid angle of the outflow, that we set to 2.1 sr, as in Torresi et al. (2012). This is derived assuming that at least 50% of radio-loud objects host an outflow, like in Seyferts galaxy, and using the information that ∼33% of the radio galaxies belonging to the 3CR sample are type 1 AGN (Buttiglione et al. 2009). Hence, using the mass outflow rate, the kinetic luminosity of the outflow is readily computed as $L_{\text{kin}} = \frac{1}{2}\dot{M}_{\text{out}}v_{\text{out}}^2$.

The value we obtained for the latter is at least four order of magnitude lower than the bolometric luminosity. Theoretical AGN feedback models (e.g., Di Matteo et al. 2005, Hopkins & Elvis 2010) typically require kinetic luminosities of the same order of the bolometric luminosity for an outflow to be able to halt the star formation in a typical galactic bulge. Thus, this outflow is unable to deliver a significant feedback in this AGN. Moreover, as found for the other radio-loud galaxies hosting a WA, the kinetic luminosity of the outflow
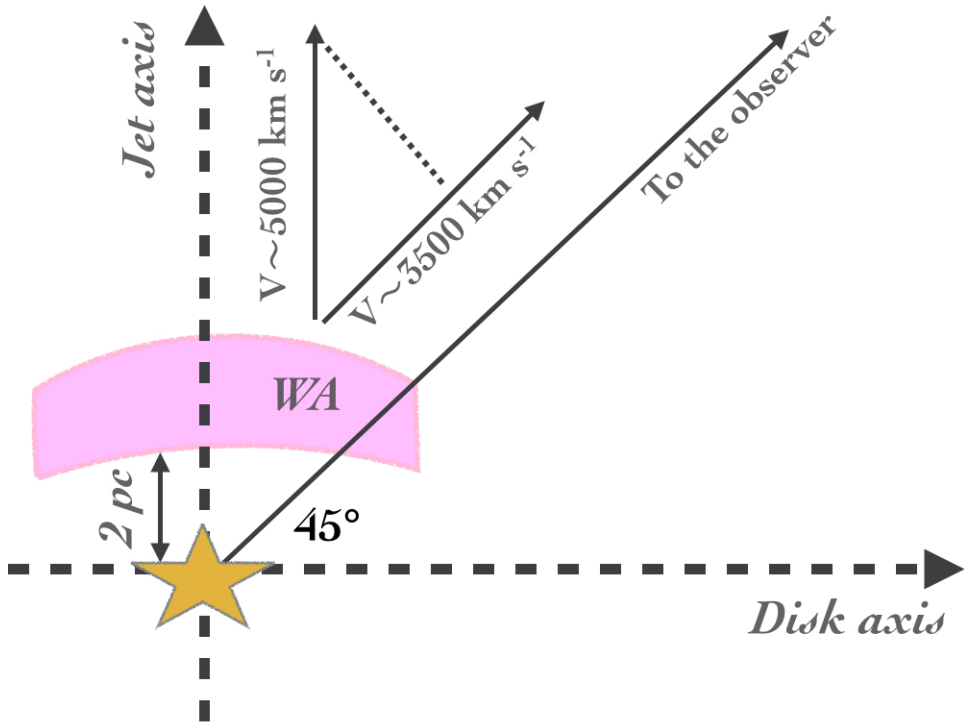
Figure 4.7: Sketch of the outflow in the inner region of 4C +74.26. The observer line of sight lies at 45° from the jet axis. The WA is part of a polar outflow located outside the BLR. The ionized gas outflows along the polar direction with a velocity of ~5000 km s^{-1}, which is observed as ~3500 km s^{-1} from the observer inclination angle.

is negligible compared to the jet power ($L_{kin} \sim 10^{-2} P_{jet}$). Thus, the case of 4C +74.26 confirms that the jet is a more likely driver of AGN feedback in radio-loud galaxies (Torresi et al. 2012).

4.6   Summary

We performed a joint analysis of the RGS and of the HETGS spectrum of the radio loud quasar 4C +74.26. The spectrum is affected by an heavy X-ray absorption, arising from both Galactic and intrinsic material.

The most of the absorption in the soft X-ray band is due to the Galactic ISM. We point out that when considering also the contribution of molecular hydrogen, the total Galactic N_H is roughly twice the standard value provided by 21 cm surveys.

A photoionized outflow ($N_{\rm H} \sim 3.2 \sim 10^{21}$ cm^{-2}, $\log \xi \sim 2.6$, $v_{\rm out} \sim 3600$ km s^{-1}) located at the source rest-frame produces a sharp Fe-UTA trough in the RGS and the weak absorption features visible in the HETGS. The kinetic luminosity carried by the outflowing gas ($L_{\rm kin} \sim 10^{-5} L_{\rm bol}$) is negligible for the AGN feedback in this source.

We discuss a scenario where the photoionized gas is part of a polar-scattering outflow, detected also in the optical-polarized spectrum.

ACKNOWLEDGEMENTS

Nederlandse Samenvatting

Motivatie

Melkwegstelsels zijn enorme door zwaartekracht gebonden systemen die honderden miljarden sterren bevatten. Elk melkwegstelsel bevat een Super Zwaar Zwart Gat (SZZG) in het centrum. Superzwaar betekent een massa van miljoenen tot miljarden keer de massa van de zon. Het centrale SZZG is in 17% van de melkwegstelsels actief. In deze Actieve Galactische Kernen (AGK, ook bekend als Seyfert stelsels of quasars), is de optische helderheid van de kern groter dan de helderheid van alle sterren in het melkwegstelsel bij elkaar. Deze enorme hoeveelheden straling, die uit het gehele spectrum van radiogolven tot gamma-straling bestaan, worden gevoed door het invallen van materiaal vanuit het melkwegstelsel naar het zwarte gat toe. Accretie door zwaartekracht is de meest efficiënte manier die de natuur kent om energie te onttrekken aan normale materie.

Astrofysische metingen laten zien dat de massa van het centrale SZZG ook de massa van de centrale bol van sterren bepaalt. Dit is de zogenaamde $M-\sigma$ relatie die we in Fig. 1 laten zien. Op de één of andere manier beïnvloedt de activiteit van het centrale SZZG de mogelijkheid van het melkwegstelsel om tijdens zijn evolutie sterren te vormen. Theoretische modellen voor deze AGK terugkoppeling verwachten dat een snelle gasvormige wind, gevoed door het actieve zwarte gat, uitzet in het omringende melkwegstelsel en op een gecompliceerde manier interactie daarmee ondergaat. Onder sommige omstandigheden is de wind zelfs in staat om grote uitstromen van gas te veroorzaken die uiteindelijk de hele koele gasvoorraad uit het melkwegstelsel blaast. Een tekort aan koel gas heeft voor het melkwegstelsel het gevolg dat er geen nieuwe sterren meer gevormd worden en dat het zwarte gat niet verder groeit. Men denkt dat dit mechanisme de $M-\sigma$ relatie reguleert. Er worden verschillende soorten AGK winden waargenomen in submillimeter, infrarood, optisch, UV en Röntgenstraling met spectroscopische technieken. Met behulp van een spectroscopische observatie kunnen de fysische eigenschappen van de wind worden gemeten. Deze kunnen vergeleken worden met de verwachtingen uit de huidige theoretische modellen. Het uiteindelijke doel van dit onderzoek is het vinden van observationeel bewijs dat AGK terugkoppeling bestaat.
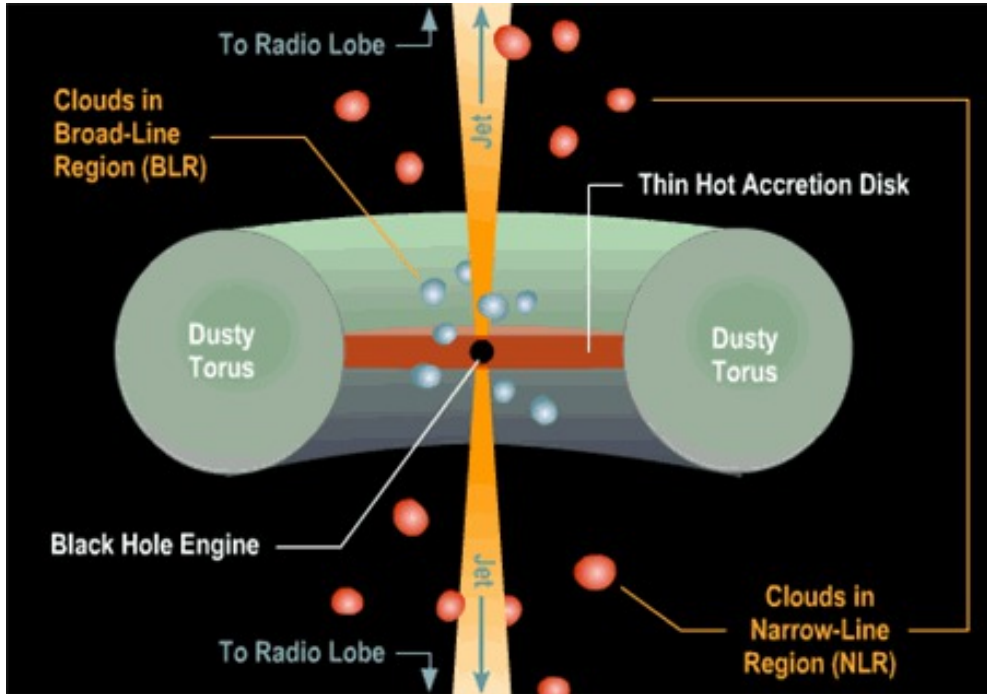
De anatomie van een AGK

De zichtbare eigenschappen van een AGK kunnen veel van elkaar verschillen. Sommige AGK zijn bijvoorbeeld sterke bronnen van radiostraling, terwijl anderen dat niet zijn. Vanuit spectroscopisch oogpunt kunnen AGK opgedeeld worden in twee klasses: Type I AGK laten zowel nauwe als brede emissielijnen zien in de optisch/UV/Röntgen band, terwijl het spectrum van Type II AGK alleen nauwe emissielijnen laat zien. We denken dat
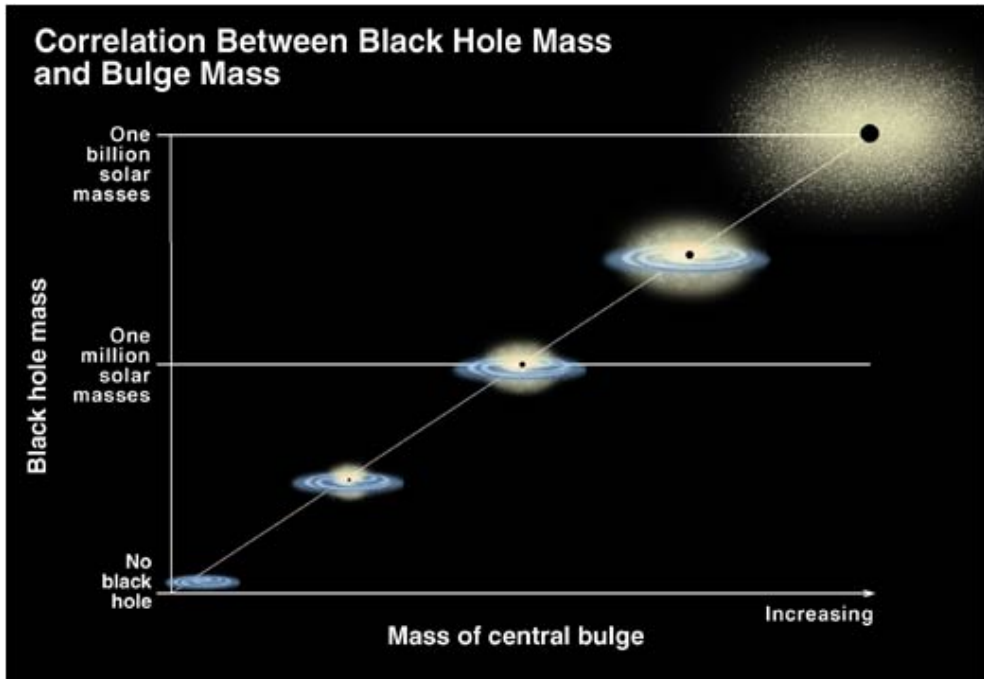
Figuur 4.8: Correlatie tussen de massa van get zwarte gat en de massa van de centrale bult van het melkwegstelsel. [Credit: K. Cordes & S. Brown (STScI)]

dit verschil wordt verklaard door een eenvoudig enkelvoudig model. In Fig. 2 laten we een illustratie van het model zien. Van binnen naar buiten bevat dit model het volgende:

1. Een SZZG omringd door een accretieschijf. De schijf zendt vooral thermische straling uit in de optische/UV band.

2. Een Brede-Lijn Regio (BLR) gevormd door wolken van geïoniseerd gas die in een snelle baan (met een snelheid in de orde van 10 000 km s^{-1}) rond het zwarte gat draaien. De BLR staat op maximaal een paar lichtdagen afstand van de kern.

3. Een torus van optisch dik en koud materiaal die de kern en de BLR omvat. De torus ligt op een paar lichtjaar afstand van de kern.

4. Een kegelvormige Nauwe-Lijn Regio (NLR) gevormd door geïoniseerde gaswolken die met ongeveer 100 km s^{-1} in een baan rond de kern draaien. De NLRs zijn zowel boven als onder de polen van de torus te vinden en kunnen op afstanden tot wel 100 lichtjaar van de kern staan.

5. Een nauwe straalstroom van relativistische deeltjes afkomstig vanuit de kern. De deeltjes in de straalstroom zenden synchrotronstraling uit in de radio band. De straalstroom is er niet altijd. Dit bepaalt of een AGK 'radio-luid' of 'radio-stil' is.

Figuur 4.9: Schematische weergave van de basisanatomie van een AGK, volgens het zogenaamde "geünificeerde model". [Credit: Brooks/Cole Thomson Learning]

Volgens deze geometrie zijn de kern en de BLR gezien vanuit een equatoriale gezichtslijn achter de torus verscholen. Deze objecten zien eruit als Type II AGK. AGK die daarentegen vanuit een polaire gezichtslijn worden bekeken, zien eruit als Type I AGK.

AGK in de Röntgenband

In dit proefschrift bestuderen we AGK met behulp van Röntgenspectroscopie. De huidige instrumentatie voor Röntgenastronomie is geschikt voor zowel lage resolutie spectroscopie in een brede band (0.3−10 keV) als hoge resolutie spectroscopie. De eerste is het beste geschikt voor het bestuderen van de continuumemissie in de Röntgenband, terwijl de laatste beter bruikbaar is voor het bestuderen van uitstromen van gas.

Het Röntgen continuum

De accretieschijf in AGK zendt niet veel straling uit in de Röntgenband. Men denkt dat de Röntgenstraling wordt geproduceerd in een compacte corona van heet plasma op een afstand van een paar lichturen van het zwarte gat. De optische en UV fotonen die door de schijf worden uitgezonden krijgen meer energie als zij met de hete electronen in de

corona botsen. Daarom verlaten ze de corona als Röntgenfotonen. Dit is een bekend stralingstransportverschijnsel dat het 'inverse Compton' effect wordt genoemd.

Het Röntgenspectrum dat door deze Comptonisatie wordt geproduceerd kan benaderd worden door een machtswet. Dit is een spectrale vorm die inderdaad alomvertegenwoordigd is in AGK spectra boven de ∼2 keV. Bij energiën onder de 2 keV, daarentegen, ligt het spectrum van type I AGK vaak boven deze theoretische machtswet. De oorsprong van deze 'zachte' Röntgenstraling is nog steeds een open vraagstuk.

AGK zijn variabele Röntgenbronnen. Spectra van dezelfde AGK die op verschillende tijdstippen genomen zijn, kunnen er heel verschillend uitzien, zowel in helderheid als spectrale vorm. De helderheid in de 'zachte' Röntgenband kan bijvoorbeeld een factor 2−20 zwakker zijn en tegelijkertijd in de loop van enkele uren behoorlijk veranderen. In veel gevallen verklaart een tijdsafhankelijke absorptie van de Röntgenstraling de waargenomen variabiliteit goed. In de praktijk zien AGK er meer of minder helder uit in Röntgenstraling afhankelijk van hoeveel Röntgenstraling er langs de gezichtslijn wordt geabsorbeerd. Deze variabele Röntgenabsorptie wordt veroorzaakt door wolken van koud (neutraal) materiaal aan bijvoorbeeld aan de rand van de torus, of in sommige gevallen zelfs in de BLR.

Warme absorbeerders

Ruwweg de helft van de Seyfert 1 melkwegstelsels bevat een warme absorbeerder (WA), in essentie een 'zachte' (v_{out} =∼100−1000 km s^{-1}) uitstroom van geïoniseerd gas. De geïoniseerde atomen in de wind absorberen het licht uit de kern op een specifieke frequentie. De WA laat zich in een spectrum zien als een overmaat aan Nauwe Absorptie Lijnen (NAL) van diverse geïoniseerde elementen, zoals ijzer, zuurstof, stikstof en koolstof. De lijnen worden gedetecteerd in hoge-resolutie UV en Röntgenspectra van AGK. Vanwege de beweging van het gas naar ons toe, worden de lijnen op een frequentie gemeten die iets hoger ligt dan de frequentie in het laboratorium. Dit heet het Doppler effect. De verschuiving van de frequentie is daarom een maat voor de uitstroomsnelheid van de wind.

Het materiaal van de WA blijft vrij constant geïoniseerd omdat het continu wordt verlicht door de straling uit de kern. Dit wordt fotoïonisatie genoemd. In een fotogeïoniseerd gas in evenwicht is het aantal ionisaties (een foton botst met een atoom waardoor een elektron losschiet) op hetzelfde moment gelijk aan het aantal recombinaties (een electron valt terug in het atoom en zendt een foton uit). Door deze fotoïonisatiebalans expliciet uit te rekenen is het mogelijk om de concentratie van alle soorten ionen in het gas te voorspellen en daarmee ook de sterkte van de absorptielijnen uit te rekenen. Dit modelleren van fotoïonisatie levert een meting op van de mate van ionisatie van het gas, die wordt aangeduid met de ionisatieparameter ξ, en van het globale absorberend vermogen dat wordt aangeduid met de kolomdichtheid van waterstof $N_{\rm H}$.

In de afgelopen 15 jaar zijn WAs uitgebreid onderzocht door veel waarneemcampagnes in het UV/Röntgen van Seyfert 1 AGK uit te voeren. Hiermee is een gedetailleerd fysisch beeld ontstaan. WA zijn winden die zelfs in één object meerdere onderdelen met verschillende ionisatieparameters en snelheden bevatten. De lijnen die bij de hoogst-

geïoniseerde WA horen (Ne IX–Ne X, O VII–O VIII en C VI) worden alleen in de Röntgenband gedetecteerd, terwijl de laagst-geïoniseerde lijnen alleen in het UV te meten zijn (Si II–Si III, Mg II en C II–C IV). In sommige gevallen kan een tussenfase lijnen zowel in de UV als Röntgenband produceren (O VI).

Het is vaak niet mogelijk om de afstand r van de WA tot de kern nauwkeurig vast te stellen. In principe geeft de ionisatieparameter ξ, die schaalt als $1/nr^2$ met n de gasdichtheid, een directe indicatie van de WA afstand. In de meeste gevallen wordt er echter geen directe indicator van de gasdichtheid gemeten en is alleen een orde van grootte schatting van de afstand mogelijk. Af en toe laat een UV absorptielijn van een dichtheidsafhankelijk metastabiel niveau het toe de dichtheid te schatten. Het meten van de recombinatietijdschaal $t_{\text{rec}} \sim n^{-1}$ van een specifiek ion (het meten van de reactietijd van de absorptielijn op de verandering van het stralingscontinuüm) is een andere mogelijke methode om de dichtheid te bepalen. Om de reactietijd te kunnen meten is het nodig om tijdsopgeloste spectroscopie te gebruiken op een tijdschaal van een paar ks tot een paar dagen, afhankelijk van de bron.

Met behulp van deze methoden is de afstand van de WA in een handvol nabije AGK vastgesteld. Volgens de huidige schattingen zijn WA ongeveer even ver verwijderd van de kern als de verhullende torus. Het bepalen van de afstand geeft ook een schatting van de energie die de WA aan de omgeving aflevert. Dit wordt uitgerekend via de kinetische helderheid $L_{\text{kin}} \sim v^3 N_{\text{H}} r$. Het is nuttig om deze helderheid te vergelijken met de totale AGK helderheid L_{bol} om te bepalen of de WA belangrijk is voor de AGK terugkoppeling met het melkwegstelsel. Voor een typische WA is L_{kin} veel kleiner dan L_{bol}, dus dragen deze geïoniseerde winden niet veel bij aan AGK terugkoppeling.

Dit proefschrift

In dit proefschrift hebben we Röntgenspectroscopie gebruikt om de gaswolken rondom de kern en het emissiemechanisme in drie nabije AGK te bestuderen: 1H 0419-577, NGC 5548 en 4C +74.26. De belangrijkste resultaten zijn:

1. We hebben gevonden dat de Röntgen WA in 1H 0419-577, die ook in het UV gedetecteerd is, deel is van een galactische wind. Gebruikmakend van fotoïonisatie modellering hebben we laten zien dat de optische/UV/Röntgen NLR een gecompliceerde gasrijke omgeving is die gelaagd is in zowel ionisatie als dichtheid.

2. Met optische/UV/Röntgen data hebben we laten zien dat de extra zachte Röntgenemissie in 1H 0419-577 misschien wordt geproduceerd door Comptonisatie van fotonen uit de accretieschijf in een warme corona die zich wellicht vlak boven de schijf bevindt. We vonden ook dat de variaties in helderheid in een brede golflengteband van deze AGK gedurende ~ 10 jaar kan worden verklaard door een variabele koude absorbeerder die zich waarschijnlijk aan de binnenste rand van de verhullende torus bevindt.

3. Met behulp van een lange waarneemcampagne van de WA in NGC 5548 in 2013 hebben we een AGK ontdekt in een ongebruikelijke toestand waarin de zachte

Röntgenstraling gedurende een lange periode werd geabsorbeerd. We hebben laten zien dat de Röntgenvariabiliteit gedurende de campagne consistent is met het beeld van een gestructureerde wind die onze gezichtslijn blokkeert. Deze wind in de buurt van de kern blokkeert ook het licht dat door de WA wordt ontvangen, waardoor die in een lagere ionisatiegraad terechtkomt in vergelijking met eerdere waarnemingen. We hebben dit scenario bevestigd door het analyseren van de Röntgenabsorptielijnen van de WA.

4. Met behulp van een hoge-resolutie Röntgenspectrum hebben we een uitstroom van fotogeïoniseerd gas in de radio-luide quasar 4C +74.26 gekarakteriseerd. Deze is consistent met een polaire verstrooiingsuitstroom die in het optisch gedetecteerd is.

English Summary

Motivation

Galaxies are giant, gravitationally bound systems containing up to 100 billions of stars. Every galaxy hosts a supermassive black hole (SMBH) in its center. Supermassive means a mass of millions-up-to-billions times the mass of the sun. In 17% of the galaxies the central SMBH is active. In these so-called Active Galactic Nuclei (AGN, a.k.a. Seyfert galaxies, or quasars), the optical luminosity of the point-like nucleus overcomes the starlight luminosity of the entire galaxy. This enormous release of radiation, which ranges from radio up to gamma-ray energies, is powered by the gravitational infalling of galactic material onto the SMBH. Gravitational accretion is indeed the most efficient way in nature to extract energy from normal matter.

Astrophysical measurements show that the mass of the central SMBH determines the number of stars contained the galactic spheroid (the so-called bulge). This is the so-called $M - \sigma$ relation that we show in Fig. 1.

Thus, somehow, while the galaxy evolves, the activity of the central SMBH influences its ability to form stars. Theoretical models for this so-called AGN feedback prescribe that a fast gaseous wind, powered by the black-hole activity, expands in the galactic environment and interacts with it in a complex way. In some conditions, the nuclear wind is able to drive a large-scale outflow which eventually depletes the galaxy of its gas reservoir. Hence, as a consequence of the lack of cold gaseous material, the galaxy stops forming stars and the black hole stops growing. This mechanism is believed to regulate $M - \sigma$ relation.

AGN winds of different kinds are observed at submillimeter, infrared, optical, UV, and X-ray energies using spectroscopical techniques. From a spectroscopical observation, the physical properties of the wind can be measured. These can be compared with the predictions of the current theoretical scenarios. The ultimate aim of this research is finding the observational proof of AGN feedback.

Anatomy of an AGN

The observational properties of AGN can be quite diverse. For instance, some AGN are powerful radio emitters, while some others are not. From a spectroscopical point of view, AGN can be divided in two classes. Type 1 AGN exhibit both narrow and broad emission lines in the optical/UV/X-ray spectrum, while the spectrum of type 2 AGN displays only narrow emission lines. We believed that this dichotomy is explained by a simple Unified Model. In Fig. 2 we show the basic AGN anatomy.

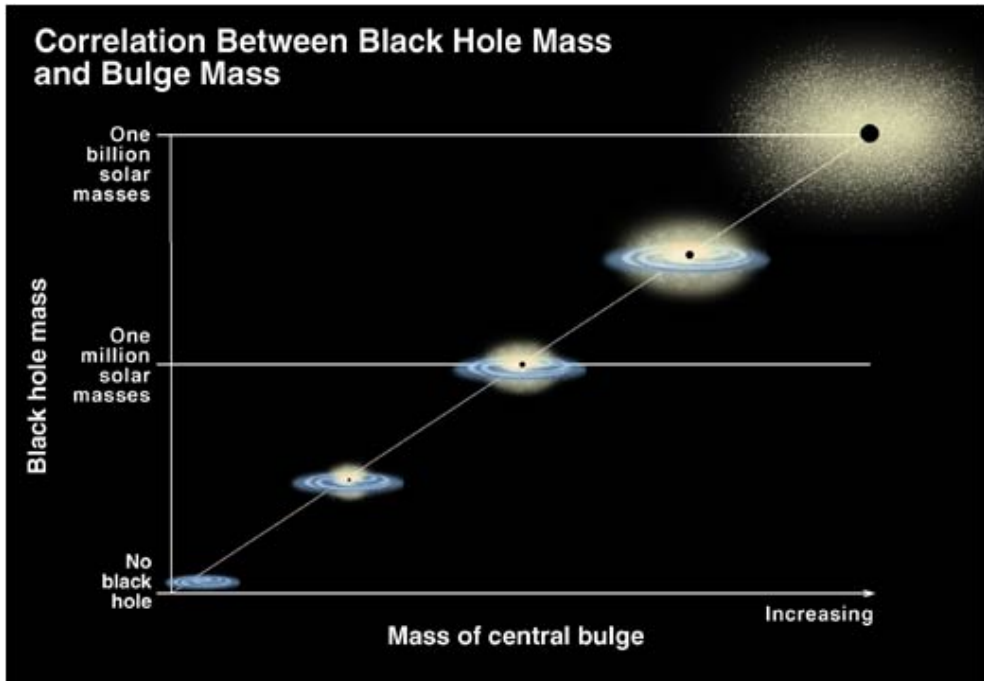Inside out, the model comprises:

Figure 4.10: Graphical representation of the black hole mass-galaxy bulge mass correlation. [Credit: K. Cordes & S. Brown (STScI)]

1. A SMBH surrounded by an accretion disk. The disk emits thermal radiation mostly in the optical/UV band.

2. A Broad Line Region (BLR) formed by ionized gas clouds orbiting around the black hole at velocities of the order of $10\,000$ km s^{-1}. The BLR is located at a maximum distance of few light-days from the nucleus.

3. A torus of optically-thick, cold, material surrounding the nucleus and the BLR. The torus is located at a distance of few light-years from the nucleus.

4. A conically-shaped narrow line region (NLR) formed by ionized gas clouds orbiting around the center at velocities of the order of few 100 km s^{-1}. The NLR is located above and below the pole the torus and may extend up to distances of the order 100 light-years from the nucleus

5. A collimated jet of relativistic particles, emanating from the nucleus. The particles in the jets emit synchrotron radiation in the radio band. The jet is not always present. This determines whether the AGN is radio-loud or radio-quiet.

According to this geometry, the torus screens the nucleus and the BLR light along the equatorial direction. Thus, AGN viewed from a polar inclination angle are not obscured
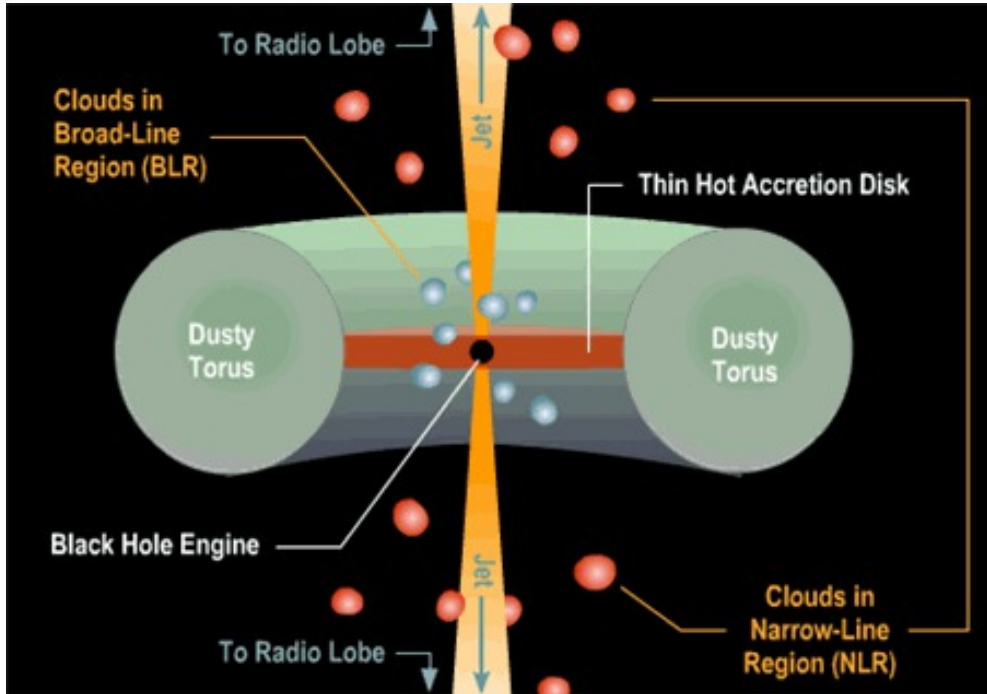
Figure 4.11: Schematic representation of the basic anatomy of an AGN, according to the so-called "Unified Model". [Credit: Brooks/Cole Thomson Learning]

by the torus and will appear as type 1. Conversely, AGN viewed from an equatorial line of sight will appear as type 2.

AGN in the X-ray band

In this thesis we study the AGN environment using X-ray spectroscopy. The current instrumentation for X-ray astronomy allows to perform both a low-resolution, but broadband (i.e., in the 0.3–10 keV band) spectroscopy, and a high-resolution spectroscopy. The former is better suited to study the X-ray continuum emission, while the latter is more useful to study the outflows.

The X-ray continuum

The accretion disk in AGN does not emit much radiation in the X-ray band. The X-ray radiation is thought to be produced in a compact corona of hot plasma located at a distance of some light-hours from the black-hole. The optical/UV photons emitted by the accretion disk gain energy from the encounter with the hot electrons of the corona. Thus, they emerge from the corona as X-ray photons. This is a well-known radiative

phenomenon named inverse Compton effect.

The X-ray spectrum produced by this Comptonization can be approximated by a power-law shape. This is indeed the spectral shape ubiquitously observed in AGN spectra above ~2.0 keV. On the other hand, at energies below ~2.0 keV, the spectrum of type 1 AGN often lies well above this theoretical power-law. The origin of this so-called soft-excess is still an open issue.

AGN are variable X-ray emitters. Spectra of the same AGN taken at different epochs may look quite different, both in luminosity and in spectral shape. For instance, the luminosity in the soft X-ray band may decrease of a large factor (e.g., 2–20) and at the same time, the spectrum may undergo significant changes even on a timescale of few hours. In many cases, a time-variable absorption of the X-ray radiation explains well the observed variability. In practice, AGN appear more or less X-ray luminous depending on how much the X-ray radiation is absorbed along the line of sight. This variable X-ray absorption may be due to some patchy cold (i.e. neutral) material located around the inner edge of the obscuring torus, or in some cases, even within the BLR.

Warm absorbers

Roughly half of Seyfert 1 galaxies host a warm absorber (WA) i.e. a gentle (v_{out}=few hundreds–few thousands km s^{-1}) outflow of ionized gas. The ionized atoms contained in the winds absorb the nuclear light at a specific frequency. Thus, the spectral signatures of WA are a plethora of narrow absorption lines (NAL) from many ionized species of common atomic elements such as iron, oxygen, nitrogen and carbon. The lines are detected in the UV and X-ray high-resolution spectra of AGN. Because of the motion of the gas towards us, these lines are detected at a frequency which is higher than the laboratory one. This is called Doppler effect. Thus, the shift in frequency of the lines provides a measurement of the outflow velocity of the wind.

The WA material remains steadily ionized because it is constantly illuminated by the AGN light. This is called photoionization. In a photoionized gas in equilibrium, the number of photoionizations (i.e. a photon hits a nucleus a nucleus and an electron is stripped) must be instantaneously equal to the number of recombinations (i.e. an electron rebinds to a nucleus and a photon is emitted). By explicitly computing this photoionization balance, it is possible to predict the concentration of all the ionic species contained in the gas and thus the expected strength of all the absorption lines. This photoionization modeling provides a measurement of the level of ionization of the gas, which is quantified by the ionization parameter ξ, and of its global absorbing power, which is quantified by the hydrogen column density N_H .

In the last fifteen years, WA have been extensively studied by performing many UV/X-ray observational campaigns of nearby Seyfert 1. A detailed physical picture has emerged. WA are multicomponent winds spanning a range in ionization and in velocity even in the same object. The lines belonging to the most highly-ionized WA components (e.g., Ne IX–Ne X, O VII–O VIII, and, C VI) are detected only in the X-ray, while the least ionized lines are detected only in the UV (e.g., Si II–Si III, Mg II, and, C II–C IV). In some cases, an intermediate phase producing absorption lines in both the UV and the X-ray band (e.g.

O VI), may be present.

Determining accurately the distance r of the WA from the center is often not possible. In principle, provided the gas density n, the ionization parameter ξ, which scales like $1/nr^2$, is a direct indicator of the WA distance. In practice, in most cases no direct density indicator is available and only an order of magnitude estimation of the distance is possible. In fewer cases, the detection in the UV of absorption lines from density-sensitive metastable levels provides a density diagnostic. Measuring the recombination timescale $t_{rec} \sim n^{-1}$ of a particular ione (i.e., measuring the time delay after which an absorption line reacts to changes in the illuminating continuum) is another possible method of determining the density. In order to observe this time delay, it is necessary to perform a time-resolved spectroscopy on a few ks–few days timescale, depending on the source.

Using these methods, the distance of the WA has been determined in a handful of nearby AGN. According to the estimations available so far, WA are often located as far as the obscuring torus. Determining the distance serves also to estimate the amount of energy that the WA delivers in the surrounding environment. This is quantified by the kinetic luminosity $L_{kin} \sim v^3\, N_H\, r$. It is useful to compare this luminosity with the total AGN luminosity L_{bol} in order to ascertain whether the WA is important for the AGN feedback scenario. For a typical WA, L_{kin} is much smaller than L_{bol}. Thus, these ionized winds alone do not contribute much to a possible AGN feedback.

This thesis

In this thesis, we have used X-ray spectroscopy to study circumnuclear gaseous environment as well as the primary emission mechanism in three nearby AGN: 1H 0419-577, NGC 5548, and, 4C +74.26.

The main results are:

- We found that the X-ray WA in 1H 0419-577, detected also in the UV, is part of a galactic wind. Using photoionization modeling techniques, we showed that the optical/UV/X-ray NLR is a complex gaseous environment stratified both in ionization and in density.

- Using optical, UV and X-ray data, we showed that the soft-excess in 1H 0419-577 may be produced by Comptonization of the disk photons in a warm corona, possibly located above the accretion disk. Moreover, we found that the broadband variability of this AGN during ~ 10 years may be due to a variable cold absorber, possibly located around the inner edge of the obscuring torus.

- In 2013, during an extended monitoring campaign dedicated to the the WA in NGC 5548, we discovered the AGN in an unusual condition of heavy and persistent soft X-ray obscuration. We showed that the X-ray variability observed during the campaign is consistent with the picture of patchy wind obscuring our line of sight. This inner wind also filters the light received by the WA, which become less ionized that what was observed during historical unobscured epochs. We confirmed this scenario by analyzing the X-ray lines of the WA.

- Using an high resolution X-ray spectrum, we characterized a photoionized gas out-
  flow in the radio-loud quasar 4C +74.26. This is consistent to be X-ray counterpart
  of a polar scattering outflow detected in the optical band for this source.

Acknowledgements

And that's it. This small booklet is the end of a life adventure. This has been fun and tough, happy and sad, wonderful and some times desperate. All in all it has been a big mess, but I never doubted that it would have been worthy to go all the way trough it.

I am grateful to a long list of persons, and I am forgetting someone for sure.

Elisa, ovviamente senza il tuo aiuto scientifico, pratico, psicologico e a tratti anche filologico non sarei mai arrivata fin qua. Grazie per tutto quello che mi hai insegnato, per essere stata sempre dalla mia parte, e per aver sempre sopportato il cocciutissimo impostore che sta dentro di me.

Thanks Jelle, for the support and for many non-trivial scientific advices.

Thanks to all the people of the NGC 5548 collaboration. It has been good to be part of such a team and I have learned a lot. And a special thanks to my new advisor, Stéphane, for having waited patiently the fulfillment of the Leiden formalities.

Thanks to Umberto, for making the cover of the booklet and to Jelle de Plaa for translating the summary.

Thanks to all the people who have been around me at SRON for helping me in many small and sometimes big things (scientific or not). Thanks also for having made my working days cheerful, and for having often tried to "beer" my mood up. Even if I do not like beer, especially at "merenda" time, I have always appreciated the attempt. Thanks to Eva, Ciro, Yan, Jacobo, Manuel, Jelle, Ton, Peter, Esther, Marlies, Jan-Willem, Marianne, Tullio, Catia, Sascha, Igone, Daniele, François, Margherita, Carlo, Missagh, Liyi, Junjie, Francesca, Kristhell, Remco (D.), Remco (S.),Tobias, Theodora, and Andreas.

A big thanks to my friends, now sparse between Italy, the Netherlands and the rest of the world. The Ph.D. stress worsened my empathy addiction and luckily my friends never left me without my dose. Thanks to my Mauritsstraat family, Davide, Dubla, Meri, Ivano, Agostino and Grazia. Thanks to the IKEA family Davide, Erica, Carla, Agnese and Amir. Thanks to Vittoria, Marco, Serena, Alice, Laura, Crucio, Isa, Kikka, Ste, Massy e Gio.

L'ultimo pensiero va alla mia vera famiglia. Senza quello che mi hanno insegnato loro non ce l'avrei mai fatta.

Curriculum Vitae

I was born on August the 30th, 1984, in Vimercate (Milano), Italy. I attended the primary and the secondary school in my city, Monza. From 1998, I studied at the scientific High School (*Liceo Scientifico*) Paolo Frisi, in Monza, and I obtained my Diploma (*Diploma di Maturità Scientifica*) in 2003, with a mark of 96/100.

In 2003, I started a Bachelor in physics (*Laurea in Fisica*) at Università degli Studi di Milano-Bicocca, in Milano. I graduated in April 2007 (mark: 101/110) with a thesis entitled "Host galaxies and progenitor in Gamma Ray Bursts". My bachelor thesis project was supervised by Prof. Guido Chincarini.

I continued my studies at the University of Milano-Bicocca with a Master in Astrophysics (*Laurea Magistrale in Astrofisica e Fisica dello Spazio*) and I obtained my Master Diploma in 2010 (mark: 109/110). For my Master project, which was supervised by Prof. Monica Colpi and co-supervised by Dr. Anna Wolter, I worked at the Observatory of Brera, in Milano. My Master dissertation was about the X-ray emission from early-type galaxies.

After my Master, I was awarded of a pre-doctoral scholarship (*Borsa di Studio per il proseguimento della formazione dei giovani promettenti*) from the Università degli Studi di Milano. With that funding, I worked from April 2011 until September 2011 at INAF/IASF in Milano on a project of Dr. Fabio Gastaldello, which was published in the Astrophysical Journal.

In September 2011 I started my Ph. D. at SRON Netherlands Institute for Space Research under the supervision of Dr. Elisa Costantini and Prof. Jelle Kaastra. During my Ph.D. I studied the physical properties of the ionized gas in the circumnuclear environment of Active Galactic Nuclei (AGN) using high resolution spectroscopy in the X-ray band and photoionization modeling techniques. The results of my Ph. D. work were published in the journal Astronomy & Astrophysics and presented at several international conferences. Since January 2016, I am employed as a postdoctoral researcher at ISDC, Integral Data Center for Astrophysics in Versoix (Genève), Switzerland in the group of Dr. Stéphane Paltani.

Bibliography

Aalto, S., Garcia-Burillo, S., Muller, S., et al. 2012, A&A, 537, A44

Anders, E. & Grevesse, N. 1989, Geochim. Cosmochim. Acta, 53, 197

Antonucci, R. 1993, ARA&A, 31, 473

Antonucci, R. R. J. & Miller, J. S. 1985, ApJ, 297, 621

Arabadjis, J. S. & Bregman, J. N. 1999, ApJ, 510, 806

Arav, N., Chamberlain, C., Kriss, G. A., et al. 2015, A&A, 577, A37

Arav, N., Edmonds, D., Borguet, B., et al. 2012, A&A, 544, A33

Arav, N., Gabel, J. R., Korista, K. T., et al. 2007, ApJ, 658, 829

Arav, N., Korista, K. T., & de Kool, M. 2002, ApJ, 566, 699

Armentrout, B. K., Kraemer, S. B., & Turner, T. J. 2007, ApJ, 665, 237

Arnaud, K. A. 1996, in Astronomical Society of the Pacific Conference Series, Vol. 101, Astronomical Data Analysis Software and Systems V, ed. G. H. Jacoby & J. Barnes, 17

Arnaud, K. A., Branduardi-Raymont, G., Culhane, J. L., et al. 1985, MNRAS, 217, 105

Asmus, D., Hönig, S. F., & Gandhi, P. 2016, ApJ, 822, 109

Bachev, R., Marziani, P., Sulentic, J. W., et al. 2004, ApJ, 617, 171

Baldwin, J., Ferland, G., Korista, K., & Verner, D. 1995, ApJ, 455, L119

Ballantyne, D. R. 2005, MNRAS, 362, 1183

Ballantyne, D. R. & Fabian, A. C. 2005, ApJ, 622, L97

Ballantyne, D. R., Ross, R. R., & Fabian, A. C. 2001, MNRAS, 327, 10

Ballantyne, D. R., Vaughan, S., & Fabian, A. C. 2003, MNRAS, 342, 239

Bambi, C. 2012, Phys. Rev. D, 85, 043001

Barvainis, R. 1987, ApJ, 320, 537

Baskin, A. & Laor, A. 2005, MNRAS, 358, 1043

Baumgartner, W. H., Tueller, J., Markwardt, C. B., et al. 2013, ApJS, 207, 19

Bautista, M., Arav, N., Dunn, J., et al. 2009, in Bulletin of the American Astronomical Society, Vol. 41, American Astronomical Society Meeting Abstracts 213, 484.08

Beckmann, V. & Shrader, C. 2012, in Proceedings of "An INTEGRAL view of the high-energy sky (the first 10 years)" - 9th INTEGRAL Workshop and celebration of the 10th anniversary of the launch (INTEGRAL 2012). 15-19 October 2012. Bibliotheque Nationale de France, Paris, France

Behar, E., Rasmussen, A. P., Blustin, A. J., et al. 2003, ApJ, 598, 232

Bianchi, S., Guainazzi, M., & Chiaberge, M. 2006, A&A, 448, 499

Bianchi, S., Guainazzi, M., Matt, G., Fonseca Bonilla, N., & Ponti, G. 2009, A&A, 495, 421

Bianchi, S., Maiolino, R., & Risaliti, G. 2012, Advances in Astronomy, 2012, 17

Blandford, R. D. & Payne, D. G. 1982, MNRAS, 199, 883

Blustin, A. J., Page, M. J., Fuerst, S. V., Branduardi-Raymont, G., & Ashton, C. E. 2005, A&A, 431, 111

Boissay, R., Ricci, C., & Paltani, S. 2016, A&A, 588, A70

Borguet, B. C. J., Edmonds, D., Arav, N., Dunn, J., & Kriss, G. A. 2012, ApJ, 751, 107

Braito, V., Reeves, J. N., Sambruna, R. M., & Gofford, J. 2011, MNRAS, 414, 2739

Brenneman, L. W., Madejski, G., Fuerst, F., et al. 2014, ApJ, 788, 61

Brinkman, B. C., Gunsing, T., Kaastra, J. S., et al. 2000, in Society of Photo-Optical Instrumentation Engineers (SPIE) Conference Series, Vol. 4012, X-Ray Optics, Instruments, and Missions III, ed. J. E. Truemper & B. Aschenbach, 81–90

Brinkmann, W., Otani, C., Wagner, S. J., & Siebert, J. 1998, A&A, 330, 67

Burrows, D. N., Hill, J. E., Nousek, J. A., et al. 2005, Space Sci. Rev., 120, 165

Burtscher, L., Meisenheimer, K., Tristram, K. R. W., et al. 2013, A&A, 558, A149

Buttiglione, S., Capetti, A., Celotti, A., et al. 2009, A&A, 495, 1033

Cackett, E. M., Fabian, A. C., Zogbhi, A., et al. 2013, ApJ, 764, L9

Canizares, C. R., Davis, J. E., Dewey, D., et al. 2005, PASP, 117, 1144

Cappi, M., Panessa, F., Bassani, L., et al. 2006, A&A, 446, 459

Cardelli, J. A., Clayton, G. C., & Mathis, J. S. 1989, ApJ, 345, 245

Carter, B. 1971, Physical Review Letters, 26, 331

Carter, B. J., Fabricant, D. G., Geller, M. J., Kurtz, M. J., & McLean, B. 2001, ApJ, 559, 606

Cash, W. 1979, ApJ, 228, 939

Cavagnolo, K. W., McNamara, B. R., Nulsen, P. E. J., et al. 2010, ApJ, 720, 1066

Cicone, C., Maiolino, R., Sturm, E., et al. 2014, A&A, 562, A21

Coffey, D., Longinotti, A. L., Rodríguez-Ardila, A., et al. 2014, MNRAS, 443, 1788

Condon, J. J., Cotton, W. D., Greisen, E. W., et al. 1998, AJ, 115, 1693

Corral, A., Page, M. J., Carrera, F. J., et al. 2008, A&A, 492, 71

Costantini, E. 2010, Space Sci. Rev., 157, 265

Costantini, E., Kaastra, J. S., Arav, N., et al. 2007, A&A, 461, 121

Costantini, E., Kaastra, J. S., Korista, K., et al. 2010, A&A, 512, A25

Crenshaw, D. M., Fischer, T. C., Kraemer, S. B., & Schmitt, H. R. 2015, ApJ, 799, 83

Crenshaw, D. M. & Kraemer, S. B. 1997, in Bulletin of the American Astronomical Society, Vol. 29, American Astronomical Society Meeting Abstracts, 1334

Crenshaw, D. M. & Kraemer, S. B. 1999, ApJ, 521, 572

Crenshaw, D. M. & Kraemer, S. B. 2012, ApJ, 753, 75

Crenshaw, D. M., Kraemer, S. B., Gabel, J. R., et al. 2003a, ApJ, 594, 116

Crenshaw, D. M., Kraemer, S. B., & George, I. M. 2003b, ARA&A, 41, 117

Crummy, J., Fabian, A. C., Gallo, L., & Ross, R. R. 2006, MNRAS, 365, 1067

de Blok, W. J. G., Walter, F., Brinks, E., et al. 2008, AJ, 136, 2648

De Marco, B., Ponti, G., Cappi, M., et al. 2013, MNRAS, 431, 2441

de Vaucouleurs, G., de Vaucouleurs, A., Corwin, J. H. G., et al. 1991, Third Reference Catalogue of Bright Galaxies. Volume I: Explanations and references. Volume II: Data for galaxies between 0^h and 12^h. Volume III: Data for galaxies between 12^h and 24^h.

den Herder, J. W., Brinkman, A. C., Kahn, S. M., et al. 2001, A&A, 365, L7

Detmers, R. G., Kaastra, J. S., & McHardy, I. M. 2009, A&A, 504, 409

Detmers, R. G., Kaastra, J. S., Steenbrugge, K. C., et al. 2011, A&A, 534, A38

Di Gesu, L., Costantini, E., Arav, N., et al. 2013, A&A, 556, A94 (Paper I)

Di Gesu, L., Costantini, E., Piconcelli, E., et al. 2014, A&A, 563, A95

Di Matteo, T., Springel, V., & Hernquist, L. 2005, Nature, 433, 604

Dickey, J. M. & Lockman, F. J. 1990, ARA&A, 28, 215

Done, C., Davis, S. W., Jin, C., Blaes, O., & Ward, M. 2012, MNRAS, 420, 1848

Dunn, J. P., Bautista, M., Arav, N., et al. 2010, ApJ, 709, 611

Dunn, J. P., Crenshaw, D. M., Kraemer, S. B., & Gabel, J. R. 2007, AJ, 134, 1061

Dunn, J. P., Crenshaw, D. M., Kraemer, S. B., & Trippe, M. L. 2008, AJ, 136, 1201

Ebrero, J., Costantini, E., Kaastra, J. S., et al. 2010, A&A, 520, A36

Ebrero, J., Kaastra, J. S., Kriss, G. A., de Vries, C. P., & Costantini, E. 2013, MNRAS, 435, 3028

Ebrero, J., Kaastra, J. S., Kriss, G. A., et al. 2016, A&A, 587, A129

Ebrero, J., Kriss, G. A., Kaastra, J. S., et al. 2011, A&A, 534, A40

Ebrero, J., Mateos, S., Stewart, G. C., Carrera, F. J., & Watson, M. G. 2009, A&A, 500, 749

Edmonds, D., Borguet, B., Arav, N., et al. 2011, ApJ, 739, 7

Elitzur, M. 2012, ApJ, 747, L33

Elitzur, M. & Shlosman, I. 2006, ApJ, 648, L101

Elvis, M. 2012, Journal of Physics Conference Series, 372, 012032

Elvis, M., Risaliti, G., Nicastro, F., et al. 2004, ApJ, 615, L25

Everett, J. E. 2005, ApJ, 631, 689

Fabian, A. C. 2006, Astronomische Nachrichten, 327, 943

Fabian, A. C., Miniutti, G., Iwasawa, K., & Ross, R. R. 2005, MNRAS, 361, 795

Fabian, A. C., Zoghbi, A., Ross, R. R., et al. 2009, Nature, 459, 540

Faucher-Giguère, C.-A. & Quataert, E. 2012, MNRAS, 425, 605

Ferguson, J. W., Korista, K. T., Baldwin, J. A., & Ferland, G. J. 1997, ApJ, 487, 122

Ferland, G. J., Korista, K. T., Verner, D. A., et al. 1998, PASP, 110, 761

Ferland, G. J., Martin, P. G., van Hoof, P. A. M., & Weingartner, J. C. 2003, ArXiv Astrophysics e-prints

Ferland, G. J., Porter, R. L., van Hoof, P. A. M., et al. 2013, Rev. Mexicana Astron. Astrofis., 49, 137

Feruglio, C., Fiore, F., Carniani, S., et al. 2015, ArXiv e-prints

Feruglio, C., Maiolino, R., Piconcelli, E., et al. 2010, A&A, 518, L155

Fiore, F., Elvis, M., Mathur, S., Wilkes, B. J., & McDowell, J. C. 1993, ApJ, 415, 129

Fischer, J., Sturm, E., González-Alfonso, E., et al. 2010, A&A, 518, L41

Gabel, J. R., Kraemer, S. B., Crenshaw, D. M., et al. 2005, ApJ, 631, 741

Gehrels, N., Chincarini, G., Giommi, P., et al. 2004, ApJ, 611, 1005

Giacchè, S., Gilli, R., & Titarchuk, L. 2014, A&A, 562, A44

Giustini, M., Turner, T. J., Reeves, J. N., et al. 2015, A&A, 577, A8

Gliozzi, M., Papadakis, I. E., Grupe, D., Brinkmann, W. P., & Räth, C. 2013, MNRAS, 433, 1709

Gofford, J., Reeves, J. N., Tombesi, F., et al. 2013, MNRAS, 430, 60

González-Alfonso, E., Fischer, J., Isaak, K., et al. 2010, A&A, 518, L43

Guainazzi, M., Comastri, A., Stirpe, G. M., et al. 1998, A&A, 339, 327

Haardt, F. & Maraschi, L. 1991, ApJ, 380, L51

Hamann, F. & Sabra, B. 2004, in Astronomical Society of the Pacific Conference Series, Vol. 311, AGN Physics with the Sloan Digital Sky Survey, ed. G. T. Richards & P. B. Hall, 203

Hamann, F. W., Barlow, T. A., Chaffee, F. C., Foltz, C. B., & Weymann, R. J. 2001, ApJ, 550, 142

Hardee, P. 2008, Journal of Physics Conference Series, 131, 012052

Harrison, C. M., Alexander, D. M., Mullaney, J. R., & Swinbank, A. M. 2014, MNRAS, 441, 3306

Harrison, F. A., Craig, W. W., Christensen, F. E., et al. 2013, ApJ, 770, 103

Hasenkopf, C. A., Sambruna, R. M., & Eracleous, M. 2002, ApJ, 575, 127

Ho, L. C., Filippenko, A. V., & Sargent, W. L. W. 1997, ApJ, 487, 568

Hönig, S. F. & Kishimoto, M. 2010, A&A, 523, A27

Hönig, S. F., Kishimoto, M., Antonucci, R., et al. 2012, ApJ, 755, 149

Hönig, S. F., Kishimoto, M., Tristram, K. R. W., et al. 2013, ApJ, 771, 87

Hopkins, P. F. & Elvis, M. 2010, MNRAS, 401, 7

Hopkins, P. F., Hernquist, L., Cox, T. J., & Kereš, D. 2008, ApJS, 175, 356

Hutsemékers, D., Hall, P. B., & Brinkmann, J. 2004, A&A, 415, 77

Immler, S., Brandt, W. N., Vignali, C., et al. 2003, AJ, 126, 153

Israel, F. P. 1998, A&A Rev., 8, 237

Iwasawa, K., Fabian, A. C., & Nandra, K. 1999, MNRAS, 307, 611

Jaffe, W., Meisenheimer, K., Röttgering, H. J. A., et al. 2004, Nature, 429, 47

Jiménez-Bailón, E., Piconcelli, E., Guainazzi, M., et al. 2005, A&A, 435, 449

Jin, C., Ward, M., Done, C., & Gelbord, J. 2012, MNRAS, 420, 1825

Kaastra, J. S. & Barr, P. 1989, A&A, 226, 59

Kaastra, J. S., Detmers, R. G., Mehdipour, M., et al. 2012, A&A, 539, A117

Kaastra, J. S., Kriss, G. A., Cappi, M., et al. 2014, Science, 345, 64

Kaastra, J. S., Mewe, R., Liedahl, D. A., Komossa, S., & Brinkman, A. C. 2000, A&A, 354, L83

Kaastra, J. S., Mewe, R., & Nieuwenhuijzen, H. 1996, in UV and X-ray Spectroscopy of Astrophysical and Laboratory Plasmas, ed. K. Yamashita & T. Watanabe, 411–414

Kaastra, J. S., Petrucci, P.-O., Cappi, M., et al. 2011, A&A, 534, A36

Kaastra, J. S., Raassen, A. J. J., Mewe, R., et al. 2004, A&A, 428, 57

Kaastra, J. S., Steenbrugge, K. C., Raassen, A. J. J., et al. 2002, A&A, 386, 427

Kalberla, P. M. W., Burton, W. B., Hartmann, D., et al. 2005, A&A, 440, 775

Kallman, T. 1999, XSTAR: A program for calculating conditions and spectra of photoionized gases, Astrophysics Source Code Library

Kaspi, S., Brandt, W. N., George, I. M., et al. 2002a, ApJ, 574, 643

Kaspi, S., Brandt, W. N., George, I. M., et al. 2002b, ApJ, 574, 643

Kaspi, S., Smith, P. S., Netzer, H., et al. 2000, ApJ, 533, 631

Kellermann, K. I., Sramek, R., Schmidt, M., Shaffer, D. B., & Green, R. 1989, AJ, 98, 1195

King, A. & Pounds, K. 2015, ARA&A, 53, 115

King, A. R. 2010, MNRAS, 402, 1516

Kishimoto, M., Hönig, S. F., Beckert, T., & Weigelt, G. 2007, A&A, 476, 713

Königl, A. 2006, Mem. Soc. Astron. Italiana, 77, 598

Korista, K., Baldwin, J., Ferland, G., & Verner, D. 1997, ApJS, 108, 401

Korista, K. T. & Goad, M. R. 2000, ApJ, 536, 284

Koshida, S., Minezaki, T., Yoshii, Y., et al. 2014, ApJ, 788, 159

Kraemer, S. B., Crenshaw, D. M., Dunn, J. P., et al. 2012, ApJ, 751, 84

Kraemer, S. B., Crenshaw, D. M., Gabel, J. R., et al. 2006, ApJS, 167, 161

Kraemer, S. B., Crenshaw, D. M., George, I. M., Gabel, J. R., & NGC 4151 Team. 2005, in Bulletin of the American Astronomical Society, Vol. 37, American Astronomical Society Meeting Abstracts, 1190

Kraemer, S. B., Crenshaw, D. M., Hutchings, J. B., et al. 2001, ApJ, 551, 671

Kriss, G. A., Arav, N., Kaastra, J. S., et al. 2011, A&A, 534, A41

Krolik, J. H. & Kriss, G. A. 2001, ApJ, 561, 684

Krongold, Y., Elvis, M., Andrade-Velazquez, M., et al. 2010, ApJ, 710, 360

Krongold, Y., Nicastro, F., Brickhouse, N. S., Elvis, M., & Mathur, S. 2005, ApJ, 622, 842

Krongold, Y., Nicastro, F., Elvis, M., et al. 2007, ApJ, 659, 1022

Landt, H., Ward, M. J., Elvis, M., & Karovska, M. 2014, MNRAS, 439, 1051

Laor, A. 1991, ApJ, 376, 90

Larsson, J., Fabian, A. C., Ballantyne, D. R., & Miniutti, G. 2008, MNRAS, 388, 1037

Longinotti, A. L., Bianchi, S., Ballo, L., de La Calle, I., & Guainazzi, M. 2009, MNRAS, 394, L1

Longinotti, A. L., Costantini, E., Petrucci, P. O., et al. 2010, A&A, 510, A92

Longinotti, A. L., Krongold, Y., Kriss, G. A., et al. 2013, ApJ, 766, 104

Magdziarz, P., Blaes, O. M., Zdziarski, A. A., Johnson, W. N., & Smith, D. A. 1998, MNRAS, 301, 179

Magdziarz, P. & Zdziarski, A. A. 1995, MNRAS, 273, 837

Maiolino, R. & Rieke, G. H. 1995, ApJ, 454, 95

Malizia, A., Molina, M., Bassani, L., et al. 2014, ApJ, 782, L25

Malzac, J., Beloborodov, A. M., & Poutanen, J. 2001, in American Institute of Physics Conference Series, Vol. 587, Gamma 2001: Gamma-Ray Astrophysics, ed. S. Ritz, N. Gehrels, & C. R. Shrader, 111–115

Marchese, E., Braito, V., Della Ceca, R., Caccianiga, A., & Severgnini, P. 2012, MNRAS, 421, 1803

Marinucci, A., Matt, G., Kara, E., et al. 2014a, MNRAS, 440, 2347

Marinucci, A., Matt, G., Miniutti, G., et al. 2014b, ApJ, 787, 83

Markowitz, A. G., Krumpe, M., & Nikutta, R. 2014, MNRAS, 439, 1403

Mason, K. O., Breeveld, A., Much, R., et al. 2001, A&A, 365, L36

Mathur, S. 1994, ApJ, 431, L75

Mathur, S., Wilkes, B., Elvis, M., & Fiore, F. 1994, ApJ, 434, 493

Matt, G., Guainazzi, M., & Maiolino, R. 2003, MNRAS, 342, 422

Matt, G., Perola, G. C., & Piro, L. 1991, A&A, 247, 25

Mauch, T., Murphy, T., Buttery, H. J., et al. 2003, MNRAS, 342, 1117

McHardy, I. M., Koerding, E., Knigge, C., Uttley, P., & Fender, R. P. 2006, Nature, 444, 730

McKernan, B., Yaqoob, T., & Reynolds, C. S. 2007, MNRAS, 379, 1359

McNamara, B. R. & Nulsen, P. E. J. 2012, New Journal of Physics, 14, 055023

Mehdipour, M., Branduardi-Raymont, G., Kaastra, J. S., et al. 2011, A&A, 534, A39

Mehdipour, M., Kaastra, J. S., Kriss, G. A., et al. 2015, ArXiv e-prints

Merritt, D. & Ferrarese, L. 2001, ApJ, 547, 140

Middleton, M., Done, C., & Gierliński, M. 2007, MNRAS, 381, 1426

Miller, C. J., Nichol, R. C., Gómez, P. L., Hopkins, A. M., & Bernardi, M. 2003, ApJ, 597, 142

Miller, J. M. 2007, ARA&A, 45, 441

Miller, L., Turner, T. J., & Reeves, J. N. 2008, A&A, 483, 437

Miniutti, G. & Fabian, A. C. 2004, MNRAS, 349, 1435

Miniutti, G., Sanfrutos, M., Beuchert, T., et al. 2014, MNRAS, 437, 1776

Moe, M., Arav, N., Bautista, M. A., & Korista, K. T. 2009, ApJ, 706, 525

Molina, M., Venturi, T., Malizia, A., et al. 2015, MNRAS, 451, 2370

Morgan, C. W., Kochanek, C. S., Dai, X., Morgan, N. D., & Falco, E. E. 2008, ApJ, 689, 755

Morganti, R. 2015, in IAU Symposium, Vol. 313, IAU Symposium, ed. F. Massaro, C. C. Cheung, E. Lopez, & A. Siemiginowska, 283–288

Morganti, R., Fogasy, J., Paragi, Z., Oosterloo, T., & Orienti, M. 2013, Science, 341, 1082

Murphy, K. D. & Yaqoob, T. 2009, MNRAS, 397, 1549

Nandra, K., Fabian, A. C., George, I. M., et al. 1993, MNRAS, 260, 504

Nandra, K., O'Neill, P. M., George, I. M., & Reeves, J. N. 2007, MNRAS, 382, 194

Nardini, E., Reeves, J. N., Gofford, J., et al. 2015, Science, 347, 860

Nenkova, M., Ivezić, Ž., & Elitzur, M. 2002, ApJ, 570, L9

Nenkova, M., Sirocky, M. M., Nikutta, R., Ivezić, v., & Elitzur, M. 2008, ApJ, 685, 160

Netzer, H. 1990, in Active Galactic Nuclei, ed. R. D. Blandford, H. Netzer, L. Woltjer, T. J.-L. Courvoisier, & M. Mayor, 57–160

Netzer, H. 2004, ApJ, 604, 551

Netzer, H. 2008, New A Rev., 52, 257

Netzer, H. 2015, ARA&A, 53, 365

Netzer, H., Kaspi, S., Behar, E., et al. 2003, ApJ, 599, 933

Noda, H., Makishima, K., Nakazawa, K., et al. 2013, PASJ, 65

Noda, H., Makishima, K., Yamada, S., et al. 2011, PASJ, 63, S925

Novikov, I. D. & Thorne, K. S. 1973, in Black Holes (Les Astres Occlus), ed. C. Dewitt & B. S. Dewitt, 343–450

Nucita, A. A., Guainazzi, M., Longinotti, A. L., et al. 2010, A&A, 515, A47

O'Neill, P. M., Nandra, K., Papadakis, I. E., & Turner, T. J. 2005, MNRAS, 358, 1405

Osterbrock, D. E. 1989, Astrophysics of Gaseous Nebulae and Active Galactic Nuclei, University Science Books, Mill Valley

Page, K. L., Pounds, K. A., Reeves, J. N., & O'Brien, P. T. 2002, MNRAS, 330, L1

Page, M. J., Symeonidis, M., Vieira, J. D., et al. 2012, Nature, 485, 213

Pal, M. & Dewangan, G. C. 2013, MNRAS, 435, 1287

Pancoast, A., Brewer, B. J., Treu, T., et al. 2014, MNRAS, 445, 3073

Panessa, F., Bassani, L., Bazzano, A., et al. 2014, in Proceedings of the 12th European VLBI Network Symposium and Users Meeting (EVN 2014). 7-10 October 2014. Cagliari, Italy., 4

Panessa, F., Bassani, L., de Rosa, A., et al. 2008, A&A, 483, 151

Pearson, T. J., Blundell, K. M., Riley, J. M., & Warner, P. J. 1992, MNRAS, 259, 13P

Perola, G. C., Matt, G., Cappi, M., et al. 2002, A&A, 389, 802

Peterson, B. M. 1997, An Introduction to Active Galactic Nuclei

Peterson, B. M., Ferrarese, L., Gilbert, K. M., et al. 2004, ApJ, 613, 682

Peterson, B. M. & Horne, K. 2004, Astronomische Nachrichten, 325, 248

Peterson, B. M. & Wandel, A. 1999, ApJ, 521, L95

Petrucci, P.-O., Paltani, S., Malzac, J., et al. 2013, A&A, 549, A73

Piconcelli, E., Bianchi, S., Guainazzi, M., Fiore, F., & Chiaberge, M. 2007, A&A, 466, 855

Piconcelli, E., Jimenez-Bailón, E., Guainazzi, M., et al. 2005, A&A, 432, 15

Pinto, C., Kriss, G. A., Kaastra, J. S., et al. 2012, A&A, 541, A147

Piro, L., Matt, G., & Ricci, R. 1997, A&AS, 126, 525

Pogge, R. W. 1988, ApJ, 332, 702

Ponti, G., Miniutti, G., Cappi, M., et al. 2006, MNRAS, 368, 903

Ponti, G., Papadakis, I., Bianchi, S., et al. 2012, A&A, 542, A83

Porquet, D. & Dubau, J. 2000, A&AS, 143, 495

Pounds, K. A., Reeves, J. N., Page, K. L., & O'Brien, P. T. 2004a, ApJ, 605, 670

Pounds, K. A., Reeves, J. N., Page, K. L., & O'Brien, P. T. 2004b, ApJ, 616, 696

Pozo Nuñez, F., Haas, M., Chini, R., et al. 2014, A&A, 561, L8

Predehl, P. & Schmitt, J. H. M. M. 1995, A&A, 293, 889

Proga, D. 2007, in Astronomical Society of the Pacific Conference Series, Vol. 373, The Central Engine of Active Galactic Nuclei, ed. L. C. Ho & J.-W. Wang, 267

Proga, D., Stone, J. M., & Kallman, T. R. 2000, ApJ, 543, 686

Protassov, R., van Dyk, D. A., Connors, A., Kashyap, V. L., & Siemiginowska, A. 2002, ApJ, 571, 545

Puccetti, S., Fiore, F., Risaliti, G., et al. 2007, MNRAS, 377, 607

Raban, D., Jaffe, W., Röttgering, H., Meisenheimer, K., & Tristram, K. R. W. 2009, MNRAS, 394, 1325

Reeves, J. N., Gofford, J., Braito, V., & Sambruna, R. 2010, ApJ, 725, 803

Reeves, J. N., Sambruna, R. M., Braito, V., & Eracleous, M. 2009, ApJ, 702, L187

Reeves, J. N. & Turner, M. J. L. 2000, MNRAS, 316, 234

Reis, R. C. & Miller, J. M. 2013, ApJ, 769, L7

Reynolds, C. S. & Nowak, M. A. 2003, Phys. Rep., 377, 389

Riley, J. M. & Warner, P. J. 1990, MNRAS, 246, 1P

Riley, J. M., Warner, P. J., Rawlings, S., et al. 1989, MNRAS, 236, 13P

Risaliti, G., Elvis, M., Bianchi, S., & Matt, G. 2010, MNRAS, 406, L20

Risaliti, G., Elvis, M., Fabbiano, G., Baldi, A., & Zezas, A. 2005, ApJ, 623, L93

Risaliti, G., Elvis, M., Fabbiano, G., et al. 2007, ApJ, 659, L111

Risaliti, G., Harrison, F. A., Madsen, K. K., et al. 2013, Nature, 494, 449

Risaliti, G., Nardini, E., Salvati, M., et al. 2011, MNRAS, 410, 1027

Risaliti, G., Salvati, M., Elvis, M., et al. 2009, MNRAS, 393, L1

Rivers, E., Markowitz, A., Duro, R., & Rothschild, R. 2012, ApJ, 759, 63

Robinson, A., Corbett, E. A., Axon, D. J., & Young, S. 1999, MNRAS, 305, 97

Roming, P. W. A., Kennedy, T. E., Mason, K. O., et al. 2005, Space Sci. Rev., 120, 95

Ross, R. R. & Fabian, A. C. 2005, MNRAS, 358, 211

Rupke, D. S. N. & Veilleux, S. 2013, ApJ, 768, 75

Sambruna, R. M., Eracleous, M., & Mushotzky, R. F. 1999, ApJ, 526, 60

Sanfrutos, M., Miniutti, G., Agís-González, B., et al. 2013, MNRAS

Scannapieco, E. & Oh, S. P. 2004, ApJ, 608, 62

Schlafly, E. F. & Finkbeiner, D. P. 2011, ApJ, 737, 103

Scott, J., Kriss, G., Brotherton, M., et al. 2004, in Astronomical Society of the Pacific Conference Series, Vol. 311, AGN Physics with the Sloan Digital Sky Survey, ed. G. T. Richards & P. B. Hall, 31

Scott, J. E., Kriss, G. A., Lee, J. C., et al. 2005, ApJ, 634, 193

Shakura, N. I. 1973, Soviet Ast., 16, 756

Shih, D. C., Iwasawa, K., & Fabian, A. C. 2002, MNRAS, 333, 687

Sijacki, D., Springel, V., Di Matteo, T., & Hernquist, L. 2007, MNRAS, 380, 877

Singh, K. P., Garmire, G. P., & Nousek, J. 1985, ApJ, 297, 633

Sobolewska, M. A., Siemiginowska, A., & Życki, P. T. 2004, ApJ, 608, 80

Somerville, R. S., Hopkins, P. F., Cox, T. J., Robertson, B. E., & Hernquist, L. 2008, MNRAS, 391, 481

Steenbrugge, K. C., Fenovčík, M., Kaastra, J. S., Costantini, E., & Verbunt, F. 2009, A&A, 496, 107

Steenbrugge, K. C., Kaastra, J. S., Crenshaw, D. M., et al. 2005, A&A, 434, 569

Steenbrugge, K. C., Kaastra, J. S., de Vries, C. P., & Edelson, R. 2003, A&A, 402, 477

Strüder, L., Briel, U., Dennerl, K., et al. 2001, A&A, 365, L18

Sturm, E., González-Alfonso, E., Veilleux, S., et al. 2011, ApJ, 733, L16

Suganuma, M., Yoshii, Y., Kobayashi, Y., et al. 2006, ApJ, 639, 46

Sulentic, J. W., Marziani, P., & Dultzin-Hacyan, D. 2000, ARA&A, 38, 521

Tanaka, Y., Nandra, K., Fabian, A. C., et al. 1995, Nature, 375, 659

Tarter, C. B., Tucker, W. H., & Salpeter, E. E. 1969, ApJ, 156, 943

Titarchuk, L. 1994, ApJ, 434, 570

Tombesi, F., Cappi, M., Reeves, J. N., & Braito, V. 2012, MNRAS, 422, 1

Tombesi, F., Cappi, M., Reeves, J. N., et al. 2011, ApJ, 742, 44

Tombesi, F., Cappi, M., Reeves, J. N., et al. 2010, A&A, 521, A57

Tombesi, F., Meléndez, M., Veilleux, S., et al. 2015, Nature, 519, 436

Tombesi, F., Tazaki, F., Mushotzky, R. F., et al. 2014, MNRAS, 443, 2154

Toomre, A. 1964, ApJ, 139, 1217

Torresi, E., Grandi, P., Costantini, E., & Palumbo, G. G. C. 2012, MNRAS, 419, 321

Torresi, E., Grandi, P., Longinotti, A. L., et al. 2010, MNRAS, 401, L10

Tristram, K. R. W., Burtscher, L., Jaffe, W., et al. 2014, A&A, 563, A82

Turner, M. J. L., Abbey, A., Arnaud, M., et al. 2001, A&A, 365, L27

Turner, T. J., Miller, L., Kraemer, S. B., Reeves, J. N., & Pounds, K. A. 2009, ApJ, 698, 99

Urry, C. M. & Padovani, P. 1995, PASP, 107, 803

Ursini, F., Boissay, R., Petrucci, P.-O., et al. 2015, A&A, 577, A38

Véron-Cetty, M.-P. & Véron, P. 2006, A&A, 455, 773

Wagner, A. Y. & Bicknell, G. V. 2011, ApJ, 728, 29

Wagner, A. Y., Bicknell, G. V., & Umemura, M. 2012, ApJ, 757, 136

Wakker, B. P., Lockman, F. J., & Brown, J. M. 2011, ApJ, 728, 159

Wakker, B. P. & Savage, B. D. 2009, ApJS, 182, 378

Walton, D. J., Reis, R. C., & Fabian, A. C. 2010, MNRAS, 408, 601

Walton, D. J., Risaliti, G., Harrison, F. A., et al. 2014, ApJ, 788, 76

Wandel, A. 2002, ApJ, 565, 762

Weigelt, G., Hofmann, K.-H., Kishimoto, M., et al. 2012, A&A, 541, L9

Weymann, R. J., Morris, S. L., Foltz, C. B., & Hewett, P. C. 1991, ApJ, 373, 23

Whewell, M., Branduardi-Raymont, G., Kaastra, J. S., et al. 2015, A&A, 581, A79

Wilkins, D. R. & Fabian, A. C. 2013, MNRAS, 430, 247

Wilkins, D. R. & Gallo, L. C. 2015, MNRAS, 449, 129

Willingale, R., Starling, R. L. C., Beardmore, A. P., Tanvir, N. R., & O'Brien, P. T. 2013, MNRAS, 431, 394

Wilson, A. S., Shopbell, P. L., Simpson, C., et al. 2000, AJ, 120, 1325

Winter, L. M., Lewis, K. T., Koss, M., et al. 2010, ApJ, 710, 503

Winter, L. M., Veilleux, S., McKernan, B., & Kallman, T. R. 2012, ApJ, 745, 107

Yao, Y. & Wang, Q. D. 2005, ApJ, 624, 751

Yaqoob, T. & Murphy, K. D. 2011, MNRAS, 412, 277

Yaqoob, T. & Padmanabhan, U. 2004, ApJ, 604, 63

Yuan, Q., Green, R. F., Brotherton, M., et al. 2002, ApJ, 575, 687

Zycki, P. T. & Czerny, B. 1994, MNRAS, 266, 653